Edge of Chaos Theory Unveils the First and Simplest Ever Reported Hodgkin–Huxley Neuristor

ADVANCED ELECTRONIC MATERIALS Open Access
www.advelectronicmat.de

Edge of Chaos Theory Unveils the First and Simplest Ever Reported Hodgkin–Huxley Neuristor

Alon Ascoli, Ahmet Samil Demirkol, Ioannis Messaris, Vasilis Ntinas, Dimitris Prousalis, Stefan Slesazeck, Thomas Mikolajick, Fernando Corinto, Michele Bonnin, Marco Gilli, Pier Paolo Civalleri, Ronald Tetzlaff, and Leon Chua*

The Hodgkin-Huxley model is an accurate yet convoluted mathematical description of the complex nonlinear dynamics of a biological neuronal axon. Employing four degrees of freedom, three of which embodied by the sodium and potassium memristive ion channels, it is capable to capture the cascade of three fundamental bifurcations, specifically a Hopf supercritical, a Hopf subcritical, and a saddle-node limit cycle bifurcation, marking the life cycle from birth to extinction via All-to-None effect of an electrical spike, also referred to as Action Potential in the literature, across biological axon membranes under monotonic change in the net synaptic current. This paper recurs to powerful concepts from the Local Activity and Edge of Chaos Principle and to methods from Circuit Theory and Nonlinear Dynamics to design the first and simplest ever-reported electrical circuit, which, leveraging the peculiar Negative Differential Resistance effects in a volatile NbOx threshold switch from NaMLab, and including additionally just one capacitor and one DC current source in its minimal topology, undergoes the three-bifurcation cascade, emerging across the fourth-order Hodgkin-Huxley neuron model under monotonic current sweep, while requiring half the number of degrees of freedom, which reveals the promising potential of Memristors on "Edge of Chaos" for energy-efficient bio-inspired electronics.

1. Introduction

The amplification of infinitesimal fluctuations in energy[1] upon suitable polarization is the *Conditio Sine Qua Non* for a physical system to enter a particularly interesting operating domain known as *Local Activity*.[2] Specifically, a physical system, which exchanges energy with the external environment, may exhibit complex dynamical behaviors if and only if it may be biased about some locally active operating point.[3] More importantly, emergent phenomena may first appear across its medium when it is polarized in a region of the local activity domain, known as *Edge of Chaos*. In this regime, which, given its significance, is often referred to as the *Pearl or Crown Jewel of Local Activity*, the system is poised on a locally active and asymptotically stable operating point, featuring a high degree of excitability, hidden behind the quiet state it sits at. Under these conditions, small perturbations of the system may induce the sudden occurrence of dramatic events, known as *Bifurcations* in Nonlinear Dynamics Theory,[4] across its physical medium, resulting in the instability of the operating point, and in the manifestation of complex phenomena at steady state. For example, a biological neuron is poised on the Edge of Chaos[5] when the net synaptic current, flowing into its physical medium through dendritic paths, attains a critical level, referred to as *Hopf Supercritical Bifurcation*[6] point, at which a train of electrical spikes, known as *Action Potentials* in Neuroscience, first develops across its membrane capacitance. The Edge of Chaos is a universal physics principle, grounded on solid theoretical foundations, which enables to explain the

A. Ascoli, F. Corinto, M. Bonnin, M. Gilli, P. P. Civalleri
Department of Electronics and Telecommunications
Politecnico di Torino
Corso Duca degli Abruzzi 24, Turin, Piedmont 10129, Italy
E-mail: alon.ascoli@polito.it

The ORCID identification number(s) for the author(s) of this article can be found under https://doi.org/10.1002/aelm.202400789

DOI: 10.1002/aelm.202400789

A. S. Demirkol, I. Messaris, V. Ntinas, D. Prousalis, R. Tetzlaff
Institut für Grundlagen der Elektrotechnik und Elektronik
Technische Universität Dresden
Mommsenstraße 12, 01069 Dresden, Saxony, Germany

S. Slesazeck, T. Mikolajick
NaMLab gGmbH
Nöthnitzer Straße 64a, 01187 Dresden, Saxony, Germany

T. Mikolajick
Institut für Halbleiter- und Mikrosystemtechnik
Technische Universität Dresden
Nöthnitzer Straße 64, 01187 Dresden, Saxony, Germany

L. Chua
Department of Electrical Engineering and Computer Sciences
University of California Berkeley
Hearst Avenue 2626, Berkeley, CA 94720, USA

mechanisms behind complex phenomena in any non-isolated system. It can be invoked to investigate the origin for complexity in all fields of research, including physics, electronics, chemistry, and biology. Differently from resistance switching memories from the non-volatile class,[7] a volatile memristor may not serve as a data storage device. However, if it falls in the class of locally-active memristors, such as ovonic threshold switches,[8] and second-order diffusive memristors,[9] it is blessed with the extraordinary capability to act as a source of *small-signal or local* energy under suitable polarization, in a similar way as a metal oxide semiconductor field effect transistor (MOSFET) biased in the saturation region. Certain solid-state *volatile* resistance switching memories, including niobium oxide (NbO_x),[10,11] and vanadium oxide (VO_x),[12] electro-thermal memristors[13] inherently feature a distinctive signature for Local Activity, namely a *Negative Differential Resistance* (NDR) at any of the continuum of bias points, where the respective DC current versus voltage characteristics admit a negative slope, similarly as the sodium and potassium ion channels across a neuronal axon membrane, which crucially leverages their capability to amplify infinitesimal fluctuations in energy to support the life cycle of an Action Potential.[14,15] The fabrication of these devices as thin oxide films, filling the gaps, which form at the regularly-spaced junctions of dense crossbar arrays, consisting of two mutually-perpendicular and vertically-displaced sets of adjacent metal lines, running in parallel along rows and columns, respectively, enables to exploit the third dimension, without enlarging the integrated circuit (IC) area reserved to the underlying complementary MOSFET (CMOS-FET) circuitry. It is further worth pointing out that locally-active memristors consume a minuscule amount of power during operation, and that their use as threshold switches in combination with non-volatile memristor physical realizations[16] enables the hardware implementation of innovative in-memory data sensing and processing paradigms, which allows to reduce dramatically the time necessary to execute standard tasks in traditional computing machines, which, built around the classical von-Neumann architecture, suffer also from energy inefficiencies, besides calling for ad hoc ventilation systems to prevent thermal heat from damaging their components. All in all, locally-active memristors represent ideal device candidates for the development of bio-inspired technical systems,[17] which, obeying similar principles as biological neural networks, may approach the operating efficiency of the human brain. In fact, scientific studies have recently provided strong proof of evidence for the capability of locally-active memristors to enable the design of circuits, which reproduce fundamental bifurcation phenomena, occurring in high-order systems from cellular biology, through the interaction between a lower number of dynamical states. In particular, a simple Memristor Cellular Neural Network (M-CNN),[18] composed of two identical circuits, connected by means of a passive and linear resistor, composed of one DC voltage source with its positive series resistance, and one locally-active NbO_x memristor from NaMLab[19] each, and poised on the Edge of Chaos when uncoupled one from the other, was found to experience diffusion-driven symmetry-breaking effects, leading to the steady-state formation of *static patterns* across its physical medium, through half the number of degrees of freedom as compared to a fourth-order reaction-diffusion biological cellular system from the Turing class.[20] Furthermore, after inserting one capacitor across the NaMLab threshold switch in each of the two identical circuits within the M-CNN presented in ref. [18], the resulting fourth-order bio-inspired array[21] was found to reproduce the same counterintuitive phenomena, observed by Stephen Smale[22] in a biological reaction-diffusion cellular system, featuring double the number of dynamical states, when its two cells, sitting on a common stable and locally-active quiescent state when uncoupled one from the other, were suddenly found to wake up, experiencing sustained limit-cycle oscillations, as diffusion processes, enabling their interaction, were activated. Importantly, the studies in Refs. [18] and [21] allowed to demonstrate that the destabilization of the homogeneous solution in reaction-diffusion biological cellular networks is possible if and only if each of the identical cells is poised on the Edge of Chaos on its own. As yet another example of the capability of solid-state locally-active memristors to enable the design of bio-inspired circuits, reproducing complex natural phenomena, occurring in biological systems operating on the Edge of Chaos, while necessitating the interaction between a smaller set of dynamical states relative to the physical systems, they are intended to emulate, this manuscript presents the first and simplest ever-reported electrical cell, supporting all the three fundamental bifurcations (see section S1 in the Supporting Information file), occurring under monotonic net synaptic current sweep in the fourth-order Hodgkin-Huxley neuronal axon membrane model, through half the number of degrees of freedom as compared to the mathematical description, published in 1952 in the seminal paper,[23] which earned the authors a Nobel prize in Physiology and Medicine eleven years later. In fact, crucially, recurring to a two-parameter bifurcation analysis allows to fit the circuit parameters of the Norton form of the relaxation oscillator,[24] which, as mentioned earlier, was recently employed in ref. [21] as basic unit of a bio-inspired network, supporting diffusion-induced steady-state *dynamic pattern formation*, similarly as the biological cellular system investigated by Smale in 1974, in such a way to enable the resulting second-order cell, featuring two separate Edge of Chaos operating domains as the Hodgkin–Huxley model, to undergo all the dramatic events, signalling the life cycle of a neuronal electrical spike[25] under a progressive monotonic change in the net synaptic current according to the mathematical description in the seminal paper[23] from 1952, specifically the local *Hopf Supercritical Bifurcation*, spawning stable oscillations across the membrane capacitance, the local *Hopf Subcritical Bifurcation*, giving origin to the unstable limit cycle in the respective state space, and, eventually, the global *Saddle-Node Limit Cycle Bifurcation*, at which the outer stable and inner unstable limit cycles gently coalesce one into the other, shedding light into the true mechanisms at the basis of the *All-to-None Phenomenon*.[26] Under this viewpoint, the proposed second-order current-driven circuit is dubbed *Hodgkin–Huxley electronic neuron (neuristor)*.[27] In fact, *it is the simplest and first ever reported Hodgkin–Huxley neuristor!* Notably, despite the order of the proposed neuristor is as low as two, its circuit parameters may be massaged so as to ensure that the shape of the electrical spike, appearing cyclically in the time waveform of the current, flowing through the NbO_x memristor, may resemble closely the typical waveform of a neuronal Action Potential. Capturing neuronal dynamic phenomena of higher order requires the use of a

bio-inspired network, which, consisting of two resistively-coupled neuristors from NaMLab, similarly as the circuit[28] from Pickett et al., leverages the interaction between four dynamical states. In applications, leveraging neuronal dynamics of such complexity, the adoption of this bio-mimetic network is recommendable. However, where the qualitative reproduction of basic neuronal functionalities is sufficient to process information, the simplicity of the proposed second-order NaMLab neuristor is a favorable design choice.

It is worth to observe that the topology of the Hodgkin–Huxley neuristor may be reduced in a minimal form. In fact, the use of a linear resistor is unnecessary. In fact, *the most elementary form of the proposed Hodgkin-Huxley neuristor consists of the parallel combination between three branches, including a linear capacitor, a locally-active memristor from NaMLab, and a DC current source*, respectively. In fact, upon suitable parameter remodulation, based upon a rigorous bifurcation analysis, *the proposed three-element cell could employ any other locally-active current-controlled volatile memristor nanodevice with S-shaped DC current versus voltage locus in place for the NaMLab threshold switch, and still capture the three-bifurcation cascade underlying the life cycle of an Action Potential across biological neuronal membranes according to the Hodgkin–Huxley model predictions*. Last but not least, invoking the Duality Principle from Circuit Theory,[29] *similar conclusions, drawn in regard to the local and global behavior of a three-element circuit, combining in parallel one linear capacitor, one locally-active current-controlled volatile memristor nanodevice with S-shaped DC current versus voltage locus, and one DC current source, apply* mutatis mutandis *for the nonlinear dynamics of the respective dual cell, composed of the series connection between a linear inductor, a locally-active voltage-controlled volatile memristor nanodevice with N-shaped DC voltage versus current locus, and a DC voltage source*.

2. Fundamentals of Local Activity and Edge of Chaos Theory

The physics principle of the Edge of Chaos[2] may be universally invoked to explore emergent phenomena in any physical system. However, in line with the topic discussed in this manuscript, its theoretic foundations are presented here in the context of two-terminal circuit elements, also referred to as one-ports in Circuit Theory.[29]

2.1. What is Local Activity and How to Test a Memristive One-Port for Local Activity?

Let a memristive one-port admit m degrees of freedom, encoded in a state vector $\mathbf{x} = [x_1, x_2, \ldots, x_m] \in \mathbb{R}^m$. Let it be subject to a 1D input signal $u \in \mathbb{R}$, corresponding either to the voltage v_m, falling across it, or to the current i_m, flowing between its terminals, depending upon the nature of its control variable. Assume the one-port to display a scalar output variable $y \in \mathbb{R}$, which under the first (latter) form of excitation coincides with the current i_m (the voltage v_m), flowing between its terminals (falling across it). Let the memristor be modelled by a *Differential Algebraic Equation* (DAE) set, consisting of a *State Vector Equation* (SE) and of a *Ohm Law* (OL), which in the most general case are respectively defined as

$$\dot{\mathbf{x}} = \mathbf{f}_{\mathbf{SE}}(\mathbf{x}, u), \text{and} \tag{1}$$

$$y = y(\mathbf{x}, u) = F_{OL}(\mathbf{x}, u) \cdot u \tag{2}$$

where $\mathbf{f}_{\mathbf{SE}}(\cdot,\cdot) : \mathbb{R}^m \times \mathbb{R} \to \mathbb{R}^m$ is the *state vector evolution function*, while $F_{OL}(\cdot,\cdot) : \mathbb{R} \times \mathbb{R} \to \mathbb{R}$ is a scalar function, called *memristance* (*memductance*) when $u = i_m$ ($u = v_m$), expressing how the conductivity of the one-port depends upon its state vector and input or control variable, and corresponding to the ratio between the device output and its input. The DAE set (1)–(2) is said to model a m^{th}-order *extended memristor*. Let a DC stimulus $u = U$ be applied continuously to the one-port model (1)–(2). With reference to the state vector Equation (1), assume $\mathbf{f}_{\mathbf{SE}}(\mathbf{x}, U)$ to vanish for $\mathbf{x} = \mathbf{X} = \mathbf{X} = (X_1, ..., X_m)$. The one-port subject to the specified DC stimulus may in fact potentially admit the operating point $\mathbf{Q} \triangleq \mathbf{X}$. From the Ohm law (2), correspondingly the device output would be $Y = F_{OL}(\mathbf{Q}, U) \cdot U$. The resulting admissible bias point for the one-port is denoted as $\mathbf{P} \triangleq (U, Y)$. Importantly, there exists a one-to-one mapping between $\mathbf{P}$ and $\mathbf{Q}$. Linearizing the one-port model Equations (1)–(2) about the operating point $\mathbf{Q}$, the local model of the memristor would be found to read as

$$\delta\dot{\mathbf{x}} = \mathbf{A}_{1,1}(\mathbf{Q}) \cdot \delta\mathbf{x} + \mathbf{a}_{1,2}(\mathbf{Q}) \cdot \delta u, \text{and} \tag{3}$$

$$\delta y = \mathbf{a}_{2,1}(\mathbf{Q}) \cdot \delta\mathbf{x} + a_{2,2}(\mathbf{Q}) \cdot \delta u \tag{4}$$

where $\mathbf{A}_{1,1}(\mathbf{Q}) = \left(\partial \mathbf{f}_{\mathbf{SE}}(\mathbf{x}, u)/\partial \mathbf{x}\right)\Big|_{(x,u)=(\mathbf{Q},U)} \in \mathbb{R}^{m\times m}$, $\mathbf{a}_{1,2}(\mathbf{Q}, U) = \left(\partial \mathbf{f}_{\mathbf{SE}}(\mathbf{x}, u)/\partial u\right)\Big|_{(x,u)=(\mathbf{Q},U)} \in \mathbb{R}^{m\times 1}$, $\mathbf{a}_{2,1}(\mathbf{Q}) = \left(\partial y(\mathbf{x}, u)/\partial \mathbf{x}\right)\Big|_{(x,u)=(\mathbf{Q},U)} \in \mathbb{R}^{1\times m}$, and $a_{2,2}(\mathbf{Q}) = \left(\partial y(\mathbf{x}, u)/\partial u\right)\Big|_{(x,u)=(\mathbf{Q},U)} \in \mathbb{R}^{1\times 1}$, while $\delta\mathbf{x}$, and δy respectively are the infinitesimal state vector and output which the m^{th}-order memristive system admits in response to the small-signal or local input δu, which is subject to from the time instant $t = t_0$. Despite the elements of $\mathbf{A}_{1,1}$, $\mathbf{a}_{1,2}$, and $\mathbf{a}_{2,1}$ as well as the scalar coefficient $a_{1,1}$ depend also upon the DC stimulus $u = U$, applied to the memristive ODE model (1)–(2), typically only their dependence upon the operating point $\mathbf{Q}$ is explicitly shown. Let us now solve the device small-signal model (3)–(4) for $\delta\mathbf{x}(t_0) = \delta\mathbf{x}_0$ in the hypothesis that the respective input δu is constrained to follow the time waveform of some arbitrary yet tiny stimulus from some time instant $t = t_0$. The memristive one-port is said to be *Locally Active* at the operating point $\mathbf{Q}$ if and only if there exists at least one infinitesimally-small input signal δu, such that the local net energy $\delta\mathcal{E}(t_0, t; \mathbf{Q})$, entering the one-port within the time interval (t_0, t), with $t > t_0$, i.e.,

$$\delta\mathcal{E}(t_0, t; \mathbf{Q}) = \int_{t'=t_0}^{t'=t} \delta u(t') \cdot \delta y(t')\, dt' \tag{5}$$

ever become negative for at least one finite time instant $t = \bar{t} > t_0$.[30] Equation (5) provides a rigorous definition for the Local

Activity of a m^{th}-order memristive one-port at a given operating point $\mathbf{Q}$. However, its adoption to verify whether a one-port, subject to some given DC stimulus, may ever enter the Local Activity domain about one of the operating points, it consequently admits, is practically unfeasible. In fact, before ruling out the possibility that the one-port may ever act as a source of local energy, one should compute the time integral in Equation (5) for all t values beyond t_0, under each of the countless small-signal stimuli one may possibly conceive, after evaluating the partial derivatives, determining the values of the parameters in the linearized model (3)–(4) about any of the operating points the device may admit for any choice of the DC stimulus. Fortunately, however, the *Local Activity Theorem*,[2] enunciated below for a m^{th}-order one-port, simplifies this testing investigation. This theorem requires the preliminary determination of the DC Y versus U characteristic of the one-port, including the $\mathbf{Q}$ versus U locus, and the subsequent derivation of its *small-signal or local transfer function* $H(s, \mathbf{Q}) \triangleq \frac{\mathcal{L}\{\delta y(t)\}}{\mathcal{L}\{\delta u(t)\}}\Big|_{\mathbf{Q}}$ evaluated at some operating point of interest. It is worth observing that for a current-controlled (voltage-controlled) one-port, the local transfer function $H(s; \mathbf{Q})$ about $\mathbf{Q}$ coincides with the local impedance $Z(s; \mathbf{Q}) \triangleq \frac{\mathcal{L}\{\delta v_m(t)\}}{\mathcal{L}\{\delta i_m(t)\}}\Big|_{\mathbf{Q}}$ (local admittance $Y(s; \mathbf{Q}) \triangleq \frac{\mathcal{L}\{\delta i_m(t)\}}{\mathcal{L}\{\delta v_m(t)\}}\Big|_{\mathbf{Q}}$) evaluated at the operating point itself.

Remark 1. A m^{th}-order one-port is said to be poised on the Local Activity domain at some operating point $\mathbf{Q}$ if and only if its *small-signal or local transfer function*, evaluated therein, namely $H(s; \mathbf{Q}) \triangleq \frac{\mathcal{L}\{\delta y(t)\}}{\mathcal{L}\{\delta u(t)\}}\Big|_{\mathbf{Q}}$, satisfies at least one of the following four conditions:

(i) The i^{th} pole $s = p_H^{(i)}(\mathbf{Q})$ of the local transfer function $H(s; \mathbf{Q})$ at $\mathbf{Q}$ sits on the open right half of the complex plane (ORHP), i.e., $\Re\{p_H^{(i)}(\mathbf{Q})\} > 0$, for one i value in the set $\{1, ..., m\}$.

(ii) The i^{th} pole $s = p_H^{(i)}(\mathbf{Q})$ of the local transfer function $H(s; \mathbf{Q})$ at $\mathbf{Q}$ lies on the $j\omega$ axis, i.e., $\Re\{p_H^{(i)}(\mathbf{Q})\} = 0$, and features an either negative real-valued or complex-valued residue $k_{p_H^{(i)}(\mathbf{Q})} = \lim_{s \to p_H^{(i)}(\mathbf{Q})} (s - p_H^{(i)}(\mathbf{Q})) \cdot H(s; \mathbf{Q})$, for one i value in the set $\{1, ..., m\}$.

(iii) A set of n poles of the local transfer function $H(s; \mathbf{Q})$ at $\mathbf{Q}$, specifically the k^{th}, the $(k+1)^{\text{th}}$, ..., and the $(k+n-1)^{\text{th}}$ one, respectively referred to as $s = p_H^{(k)}(\mathbf{Q})$, $s = p_H^{(k+1)}(\mathbf{Q})$, ..., and $s = p_H^{(k+n-1)}(\mathbf{Q})$, where, with n assuming a specific value from the set $\{2, ..., m\}$, the admissible number for the index k correspondingly lies within the range $\{1, ..., m-n+1\}$, are located on the same position along the $j\omega$ axis.

(iv) The real part of the local transfer function $H(s; \mathbf{Q})$, expressed in the Fourier transform domain upon letting $s = j\omega$, and evaluated at $\mathbf{Q}$, namely $\Re\{H(j\omega; \mathbf{Q})\}$, is negative for at least one finite real value $\omega_{0,\,H}(\mathbf{Q})$ of the angular frequency ω.

2.2. What is Edge of Chaos and How to Test a Memristive One-Port for Edge of Chaos?

The capability to act as a source of local energy under suitable polarization is an essential condition for a memristive one-port to support complexity. However, in order for emergent phenomena to appear across its physical medium, the one-port must enter a particular region of the Local Activity domain, referred to as *Edge of Chaos*. While poised on the Edge of Chaos, the one-port would hide a *high degree of excitability*[31] behind a stable quiescent state. As a result, tiny changes in its nominal conditions may be sufficient to destabilize its operating point and to induce complex effects across its physical stack at steady state. In fact, it is only when a nonlinear dynamic system is about to exit from (enter into) this operating regime that it may undergo local bifurcation phenomena, inducing its state vector, initiated close to an admissible operating point for the system, to move toward some other new-born attractor (to relax back to the earlier-unstable operating point itself),[5] after transients fade away. Since it holds the epicenter for complexity, Edge of Chaos is often referred to as the Pearl or Crown Jewel of Local Activity. The *Edge of Chaos Corollary*[2] dictates the rather stringent conditions a physical system must necessarily satisfy to operate on the Edge of Chaos regime.

Remark 2. A m^{th}-order one-port is said to be poised on the Edge of Chaos at some operating point $\mathbf{Q}$ if and only if the two constraints to follow concurrently apply:

(j) All the m poles $p_H^{(1)}(\mathbf{Q})$, $p_H^{(2)}(\mathbf{Q})$, ..., $p_H^{(m)}(\mathbf{Q})$ of the local transfer function $H(s; \mathbf{Q})$ at $\mathbf{Q}$ lie on the open left half of the complex plane (OLHP), implying the asymptotic stability of the operating point.

(jj) The sign of the real part $\Re\{H(j\omega; \mathbf{Q})\}$ of the local transfer function $H(s; \mathbf{Q})$, evaluated for $s = j\omega$ about $\mathbf{Q}$, is negative for at least one real value $\omega_{0,\,H}(\mathbf{Q})$ of the angular frequency ω within the admissible range $(-\infty, \infty)$.

According to the Edge of Chaos Corollary, a m^{th}-order one-port operates on the Edge of Chaos at some operating point providing it is *Locally Active and Asymptotically Stable* at $\mathbf{Q}$, where, as a result, none of the four conditions from the Local Activity Theorem may hold true, except the one listed in item (iv) from Remark 1. Importantly, denoting the signum function, equal to +1 (−1) for non-negative (negative) values of the variable in its argument, as sign(·), such condition implies that, perturbing the one-port through a small periodic signal $\delta u(t)$, featuring an angular frequency ω_*, at which $\Re\{H(j\omega_*; \mathbf{Q})\}$ is negative, the modulus of the phase shift $\angle\delta y - \angle\delta u = \angle H = \arctan(\Im\{H(j\omega_*; \mathbf{Q})\}/\Re\{H(j\omega_*; \mathbf{Q})\}) + \pi/2 \cdot (1 - \text{sign}(\Re\{H(j\omega_*; \mathbf{Q})\}))$ between the infinitesimal signal $\delta y(t)$, which appears correspondingly at the output of the one-port, and the local stimulus itself, lies over the range (90°, 270°).[13]

3. The Life Cycle of a Neuronal Electrical Spike in the Hodgkin–Huxley Neuron Model

In 1952, Hodgkin and Huxley proposed a fourth-order nonlinear ODE model to capture the complex behavior of the giant neuronal axon membrane of a squid living across the Atlantic ocean and named *Loligo Pealeii*. The circuit-theoretic representation of the Hodgkin–Huxley mathematical model is shown in plot (a) of **Figure 1**. It shows how, as dictated by the Kirchhoff

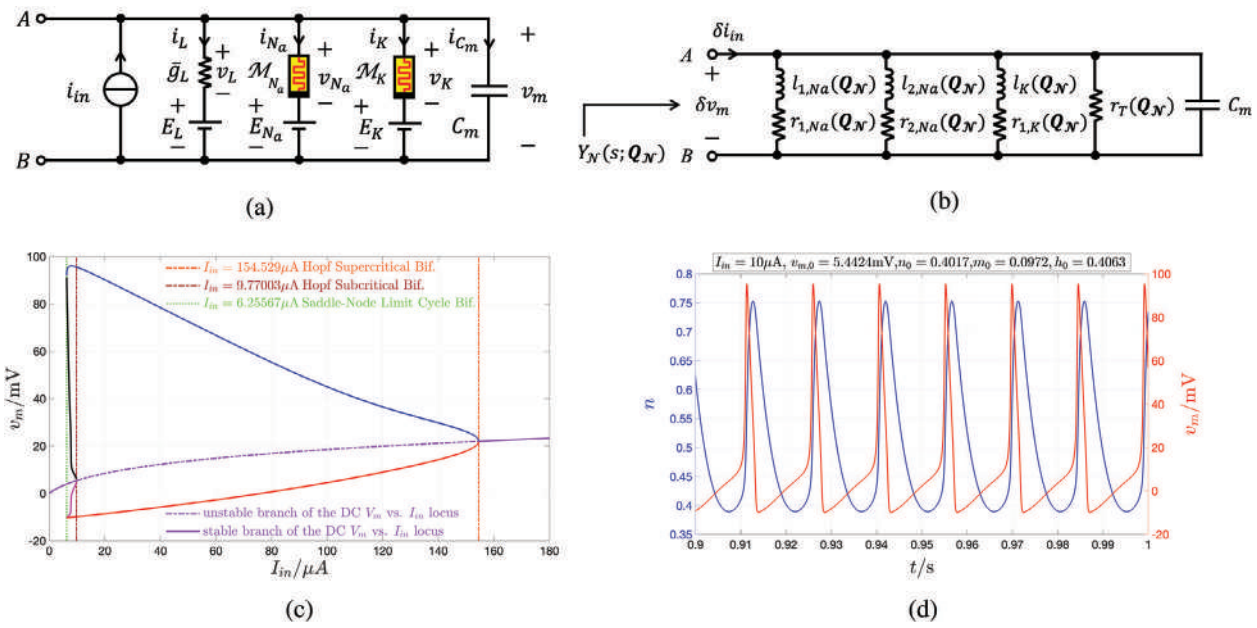

Figure 1. a) Circuit-theoretic representation of the Hodgkin–Huxley neuron model,[23] consisting of the parallel combination between an input source i_{in}, capturing the effects of the net synaptic current, acting as stimulus signal, the membrane capacitance C, the potassium ion channel memristor $\mathcal{M}_K$ with its series electrochemical gradient E_K, the sodium ion channel memristor $\mathcal{M}_{Na}$ with its series electrochemical gradient E_{Na}, and the linear conductance $\bar{g}_L$, accounting for leakage effects emerging across the axon membrane due to other ionic species, with its series electrochemical gradient E_L. b) Circuit-theoretic representation of the Hodgkin–Huxley neuron small-signal, i.e., local model about a generic operating point $\mathbf{Q}_{\mathcal{N}}$. The rightmost resistance may be computed as $r_T(\mathbf{Q}_{\mathcal{N}}) = \bar{r}_L + r_{2,K}(\mathbf{Q}_{\mathcal{N}}) + r_{3,Na}(\mathbf{Q}_{\mathcal{N}})$, where $\bar{r}_L = \bar{g}_L^{-1}$ (the interested readers are invited to consult[5] for the formulas of all the local resistances and inductances appearing in this linear circuit as a function of the neuron operating point $\mathbf{Q}_{\mathcal{N}}$). Here δv_m denotes the infinitesimally-small voltage, which develops across the membrane capacitance C in response to an infinitesimally-small input current stimulus δi_{in}. $Y_{\mathcal{N}}$ stands for the local admittance of the neuronal cell at the port A–B about $\mathbf{Q}_{\mathcal{N}}$. c) Classical bifurcation diagram of the Hodgkin-Huxley neuron model on the membrane capacitance voltage v_m versus DC net synaptic current I_{in} plane. The violet trace shows the DC V_m versus I_{in} characteristic of the neuronal cell from plot (a). Any bias point $\mathbf{P} = (I_{in}, V_m)$, lying along a solid (dash-dotted) violet branch, is associated to a stable (an unstable) operating point $\mathbf{Q}_{\mathcal{N}} = (V_m, N, M, H)$ for the neuron. For any DC input current value comprised between 6.25567 μA and 154.529 μA, resulting in the development of stable steady-state limit-cycle oscillations across the neuronal cell, a point on the top (bottom) blue (red) branch stands for the maximum (minimum) value $\max_{\text{per cycle}}\{\lim_{t\to\infty} v_m(t)\}$ ($\min_{\text{per cycle}}\{\lim_{t\to\infty} v_m(t)\}$), which the membrane capacitance voltage $v_m(t)$ assumes over each cycle of the respective periodic waveform as time approaches positive infinity (in practice, transients fade almost completely away over a finite amount of time). For any DC input current value comprised between 6.25567 μA and 9.77003 μA, resulting in the development of unstable steady-state limit-cycle oscillations across the neuronal cell, a point on the top (bottom) black (magenta) branch, stands for the maximum (minimum) value $\max_{\text{per cycle}}\{\lim_{t\to-\infty} v_m(t)\}$ ($\min_{\text{per cycle}}\{\lim_{t\to-\infty} v_m(t)\}$), which the membrane capacitance voltage $v_m(t)$ assumes over each cycle of the respective periodic waveform as time approaches negative infinity (while an attractor of a dynamic system in reverse time corresponds to a repellor for the same dynamic system in forward time, the high order of the Hodgkin-Huxley ODE set complicates the process of identifying the unstable oscillatory solution, which it admits for any DC input current I_{in} across the *bistability range* (6.25567 μA, 9.77003 μA), through a numerical integration in reverse time, which explains why, as described in the caption of Fig. 5 in the SI file, we had to recur to an alternative time-consuming numerical methodology, based on the analysis of its response in forward time, to resolve the unstable cycle detection problem). As I_{in} is continuously decreased from 180 μA to 0, the neuron undergoes a cascade of three fundamental bifurcations, which crucially govern the life cycle of an Action Potential across the neuronal membrane, namely first a Hopf supercritical bifurcation for $I_{in} = 154.529$ μA, then a Hopf subcritical bifurcation for $I_{in} = 9.77003$ μA, and finally a saddle-node limit-cycle bifurcation for $I_{in} = 6.25567$ μA. Importantly, the All-to-None effect, occurring when I_{in} is reduced down to 6.25567 μA, is the annihilation, anticipated by gentle coalescence, between two periodic solutions, of which the stable (unstable) one was born earlier (later) on, i.e., precisely, when the neuron, exited (entered) Edge of Chaos domain 2 (1) making its way into (leaving) the Unstable Local Activity domain. d) Steady-state time waveform of the potassium ion channel activation gating variable n (blue trace) and of the axon membrane capacitance voltage v_m (red trace) as observed in a numerical simulation of the Hodgkin-Huxley neuron model for $I_{in} = 10$ μA.

Current Law (KCL), the current $i_{C_m} = C_m \cdot \dot{v}_m$ flowing through the axon membrane, featuring a capacitance C_m and a voltage v_m, is an algebraic sum involving three components, and specifically the net input synaptic current i_{in}, the current i_K flowing through the potassium ion channel, the current i_{Na} flowing through the sodium ion channel, and the current i_L flowing through a resistive leakage path accounting for various contributions from other ionic species. In the original circuit representation, reported in the seminal paper from 1952,[23] Hodgkin and Huxley misinterpreted the modeling equations of the potassium and sodium ion channels in terms of time-varying resistances. On the other hand, as pointed out by Chua in 2012,[5] the first (latter) ion channel is a time-invariant first-order (second-order) voltage-controlled generic biological memristor! In fact the Hodgkin–Huxley neuron model consists of a set of four nonlinear ODEs, one for each of the state variables of the neuronal system, specifically the membrane capacitance voltage v_m, the activation gating variable n of the potassium ion channel memristor $\mathcal{M}_K$, as well as the activation and inactivation gating variables m and h of the sodium ion channel memristor $\mathcal{M}_{Na}$. Figure 1b shows the small-signal

or local equivalent circuit model of the neuron about a generic operating point $\mathbf{Q}_{\mathcal{N}} = (V_m, N, M, H)$, whose coordinates together nullify the four state evolution functions, appearing on the right hand sides of the Hodgkin–Huxley ODEs (1)-(4) in the Supporting Information file, for some DC value I_{in} assigned to the net synaptic current i_{in}. The interested reader is invited to consult Chua's seminal paper[5] for the formulas of the local resistances and inductances appearing in this circuit as a function of the neuron operating point. Plot (c) of Figure 1 compactly illustrates the bifurcations marking the life cycle of a neuronal electrical spike under a monotonic change in the net synaptic current according to the predictions of the Hodgkin–Huxley model. This plot, providing information on all the possible stable and unstable constant or oscillatory steady states for the membrane capacitance voltage v_m for each DC value of the input net synaptic current i_{in}, is in fact referred to in the literature as the *classical bifurcation diagram of the Hodgkin–Huxley neuron model*. The Supporting Information file provides an in-depth description of the emergent phenomena, which, according to this model, appear across a biological axon under a monotonic modulation of the net synaptic current stimulus, explaining furthermore how the local bifurcations, which spawn both the stable and unstable oscillations across its membrane at steady state, occur while the neuron itself is poised on the Edge of Chaos. In short, as the DC current stimulus $i_{in} = I_{in}$ is reduced from 180 μA to 0 μA, the neuron is first sitting quietly on some operating point $\mathbf{Q}_{\mathcal{N}}$, corresponding unequivocally to a bias point $\mathbf{P}_{\mathcal{N}} = (V_m, I_{in})$ lying along the rightmost stable solid portion of the DC voltage versus current characteristic drawn in violet and featuring a diode-like exponential shape. The neuron operating point $\mathbf{Q}_{\mathcal{N}}$ suddenly loses stability, its bias point $\mathbf{P}_{\mathcal{N}}$ entering the intermediate unstable dash-dotted portion of the respective DC voltage versus current characteristic, when I_{in} decreases down to 154.529 μA via a *local Hopf Supercritical Bifurcation*, which concurrently determines the birth of infinitesimal quasi-sinusoidal oscillations across the membrane capacitance, forming a tiny closed orbit, referred to as *limit-cycle attractor*, encircling the operating point $\mathbf{Q}_{\mathcal{N}}$ in the 4D v_m–n–m–h state space. This first bifurcation signals the beginning of the life cycle of the train of electrical voltage spikes, also referred to as *Action Potentials*, across the neuronal membrane. Afterwards, as the input current undergoes further decrements, the amplitude and degree of nonlinearity of the limit-cycle oscillations in the membrane capacitance voltage become larger. For example, Figure 1d shows the relaxation oscillations developing in the potassium ion channel gate activation variable n and the periodic train of Action Potentials forming the voltage v_m appearing across the membrane capacitance C_m after transients decay to zero, as observed in a numerical simulation of the fourth-order Hodgkin–Huxley ODE set – refer to Equations (S1)–(S4) in the Supporting Information file – for $I_{in} = 10$ μA and from an initial condition $(v_{m,0}, n_0, m_0, h_0) \triangleq (v_m(0), n(0), m(0), h(0))$ set to (5.4424 mV, 0.4017, 0.0972, 0.4063).

For the chosen value of the DC current stimulus, the neuron features an unstable operating point $\mathbf{Q}_{\mathcal{N}}$, lying at (V_m, N, M, H) = (5.4280 mV, 0.4031, 0.0981, 0.4034), and is found to fire periodically after transients vanish, irrespective of the initial condition. Importantly, when the net synaptic current descends down to 9.77003 μA, the neuron enters a region of *bi-stability*. In fact here yet another *local Hopf Bifurcation*, this time *of Subcritical form*, occurs across the axon membrane. As a result of this second bifurcation phenomenon, the neuron operating point re-acquires stability, yet in a local sense only, while unstable infinitesimal quasi-sinusoidal oscillations are found to develop across the neuronal axon membrane, forming yet another closed orbit, referred to as *limit-cycle repellor*, lying entirely within the larger stable cycle, while encircling the operating point $\mathbf{Q}_{\mathcal{N}}$, in the v_m–n–m–h state space.

As a result, the neuron is found to approach an operating point $\mathbf{Q}_{\mathcal{N}}$ associated to a bias point $\mathbf{P}_{\mathcal{N}}$ located on the leftmost stable solid portion of the respective DC voltage versus current characteristic, when the initial condition $(v_{m,0}, n_0, m_0, h_0) \triangleq (v_m(0), n(0), m(0), h(0))$ for its four state variables sets the starting point of the trajectory, obtained by following the time evolution of the fourth-order ODE solution $(v_m(t), n(t), m(t), h(t))$ across the 4D v_m–n–m–h state space, inside the limit-cycle repellor. On the other hand, the neuron is found to lock asymptotically into an oscillatory regime when the initial condition $(v_{m,0}, n_0, m_0, h_0)$ for its four state variables sets the starting point of the state-space trajectory outside the limit-cycle repellor. For this reason the limit-cycle repellor is referred to as *separatrix* in nonlinear dynamics theory. The input current range, across which the neuron may either fire continuously or sit on a quiescent state after transients decay to zero, exhibiting an interesting form of *bistability*, is however, very tight. In fact, as soon as the net synaptic current decreases past the Hopf Subcritical Bifurcation point, the amplitude of the unstable limit cycle oscillations in the membrane capacitance voltage, together with its degree of nonlinearity, increases dramatically, while the shape of the larger stable limit cycle oscillations is subject to comparatively-modest changes. It follows that unstable limit cycle approaches quickly the stable one until the two closed orbits gently merge one into the other, forming a unique semi-stable orbit referred to as *saddle-node limit cycle*, attracting trajectories initiated outside it while repelling those initiated inside it, on the 4D state space, when I_{in} decreases down to 6.25567 μA, which sets the locally-stable operating point $\mathbf{Q}_{\mathcal{N}}$ at (V_m, N, M, H) = (3.8790 mV, 0.3784, 0.0827, 0.4575). This phenomenon is a *global Saddle-Node Limit Cycle Bifurcation*. It marks the end of the life cycle of the action potential train. In fact, as soon as the net synaptic current decreases below this bifurcation point, the neuron is bound to approach the operating point $\mathbf{Q}_{\mathcal{N}}$ irrespective of the initial condition at the end of the transient phase. Thus, as the current stimulus descends past the Saddle-Node Limit Cycle Bifurcation point, the neuron transition from a phase, where, under suitable initial conditions, it fires continuously (the *All Effect*) to a phase, where it is found to converge asymptotically toward a quiescent state (the *None Effect*). In conclusion, the *All-to-None Phenomenon*, constituting the enigma which troubled the mind of the Italian luminary Luigi Galvani[32] in the eighteenth century, is the result of the gentle coalescence, followed by mutual annihilation, between a stable train of Action Potentials and an unstable train of neuronal electrical spikes, born earlier on out of two local Hopf Bifurcations, the first of Supercritical and the second of Subcritical nature, while the neuron operated on the Edge of Chaos. In fact, as outlined in the Supporting Information file, deriving the neuron input admittance $Y_{\mathcal{N}}(s; \mathbf{Q}_{\mathcal{N}}) \triangleq \left.\frac{\mathcal{L}\{\delta i_m(t)\}}{\mathcal{L}\{\delta v_m(t)\}}\right|_{\mathbf{Q}_{\mathcal{N}}}$ about an operating point $\mathbf{Q}_{\mathcal{N}}$ by applying basic circuit-theoretic principles to the linear circuit in plot (b) of Figure 1, and testing

it for Local Activity and Edge of Chaos by recurring to the Local Activity Theorem from Section 2.1 and to the Edge of Chaos Corollary from Section 2.2, it may be demonstrated that the neuron admits two separate operating regimes of high excitability, referred to as Edge of Chaos (EOC) domains, when, respectively, the DC input current I_{in} and the corresponding steady-state capacitance voltage V_m range across the sets to follow:

$$\text{EOC domain 1 (EOC 1)} : I_{in} \in (7.8293\,\mu\text{A}, 9.77003\,\mu\text{A})$$

$$\text{or, equivalently}$$

$$V_m \in (4.57443\,\text{mV}, 5.34305\,\text{mV}), \text{ and} \tag{6}$$

$$\text{EOC domain 2 (EOC 2)} : I_{in} \in (154.529\,\mu\text{A}, 155.731\,\mu\text{A})$$

$$\text{or, equivalently}$$

$$V_m \in (21.9425\,\text{mV}, 22.0079\,\text{mV}) \tag{7}$$

Moreover, the neuron is found to operate in the Unstable Local Activity (ULA) regime when I_{in} and V_m vary across the intervals

$$\text{Unstable Local Activity Domain (ULA)} : I_{in} \in (9.77003\,\mu\text{A},$$

$$154.529\,\mu\text{A}), \text{or, equivalently}$$

$$V_m \in (5.34305\,\text{mV}, 21.9425\,\text{mV}) \tag{8}$$

For the sake of completeness, the neuron works in the Local Passivity (LP) regime for any other DC value I_{in} of the input current i_{in} under sweep, i.e., for any other steady state value V_m which the membrane capacitance voltage v_m correspondingly assumes as follows from the DC V_m versus I_{in} characteristic. Clearly, the local Hopf Supercritical Bifurcation occurs while the neuron operates at the frontier between EOC 1 and the ULA domain, whereas the local Hopf Subcritical Bifurcation occurs while the neuron transitions through the boundary between the ULA domain and EOC 2.

Shortly, we shall present the first and simplest ever-reported bio-inspired electrical circuit, which requires just two degrees of freedom to reproduce the three-bifurcation cascade, underlying the life cycle of an Action Potential under a monotonic in the net synaptic current across neuronal membranes, according to the predictions from the Hodgkin–Huxley model, which on the other hand requires four state variables to capture these complex biological phenomena. Let us first introduce the key electrical component, specifically a locally-active memristor, to be employed later on for the design of the second-order bio-inspired circuit, which we dub *Hogdkin–Huxley neuristor*, since it captures qualitatively the complex physical phenomena at the origin of generation, development, and extinction of a train of All-or-None electrical spikes across neuronal membranes. Interestingly, as demonstrated toward the end of the manuscript in Section 6.2.2, similarly as the Hogdkin–Huxley neuron, the proposed neuristor admits two EOC domains, referred to as EOC 1 and EOC 2, separated by an ULA, transitions from EOC 1 into the ULA domain when it undergoes a local Hopf Supercritical Bifurcation, and transitions from the ULA domain into EOC 2 when it experiences a local Hopf Subcritical Bifurcation. We shall also show that, since the second EOC domain is much wider for the proposed analogue electronic cell relative to what is the case for the biological model, the Hogdkin–Huxley neuristor is still operating in this high-excitability regime as it undergoes the global Saddle-Node Limit Cycle Bifurcation, which on the other hand emerges across the biological axon membrane when it already works in the respective LP domain.

4. The NaMLab Memristor

Let us first report the large-signal mathematical model of the NbO_x memristor nano-device, fabricated at NaMLab, to be employed for the design of the Hogdkin–Huxley neuristor in Section 5.

4.1. Device Large-Signal Model

The Chua's Unfolding Principle[33] establishes a device modeling methodology based on the determination of a suitable polynomial series expansion for each of the components of the state vector evolution function $\mathbf{F_{SE}}(\mathbf{x}, u)$ as well as for the scalar function $F_{OL}(\mathbf{x}, u)$. The methodology revolves around an iterative procedure, exploring first the modeling accuracy of DAE sets, composed of polynomial series expansions of lower order, including a smaller number of terms arranged in simpler forms, before increasing the complexity of the mathematical description. For each polynomial-based DAE set candidate an optimisation algorithm is let massage the respective coefficients until it either assigns them values, which reduce the cumulative error between model predictions and experimental measurements, acquired preliminarily from some physical sample, below a prespecified threshold, or runs out of a maximum allowable simulation time without finding a suitable solution, which would lead to a new iteration of the procedure for investigating a mathematical description of higher complexity.

Adopting this device modeling methodology, the NbO_x threshold switch, known as *NaMLab memristor*,[19] was mathematically described in a simple yet accurate form through a polynomial-based DAE set falling in the class of first-order *generic memristors*, for which the function $F_{OL}(\mathbf{x}, u)$ in the Ohm law (2) depends solely upon a scalar state variable x. Letting the voltage v_m (current i_m), falling across (flowing through) the device, denote its input or control (output) variable u (y), the model of the locally-active memristor from NaMLab was cast in the form

$$\dot{x} = g(x, v_m), \text{ and} \tag{9}$$

$$i_m = i_m(x, v_m) = G(x) \cdot v_m \tag{10}$$

in which the state evolution function $g(x, v_m)$ and the memductance function $G(x)$ may be derived from their counterparts, appearing respectively in the first and second equation of the DAE set (1)–(2), for the general class of extended memristors, after suitable simplification, via the definitions $F_{SE}(x, v_m) \triangleq g(x, v_m)$ and $F_{OL}(x) \triangleq G(x)$. Most importantly, the formulas for the polynomial series expansions of the state evolution and memductance functions in the simplest generic memristor model, which could possibly fit as accurately as desired a wide set of experimental data,

Table 1. Values for the unfolding parameters in the simplest polynomial-based memristor model fit to a NbO_x locally-active volatile threshold switch from NaMLab.

a_0	a_1	b_2	$c_{2,1}$	$c_{2,2}$
$5.19 \cdot 10^{9}$	$-2.05 \cdot 10^{7}$	$7.21 \cdot 10^{9}$	$-0.07 \cdot 10^{9}$	$2.27 \cdot 10^{5}$
$c_{2,3}$	$c_{2,4}$	$c_{2,5}$	d_0	d_1
$-2.40 \cdot 10^{2}$	$1.25 \cdot 10^{-1}$	$-2.69 \cdot 10^{-5}$	$6.50 \cdot 10^{-3}$	$-6.66 \cdot 10^{-5}$
d_2		d_3		d_4
$2.14 \cdot 10^{-7}$		$-2.14 \cdot 10^{-10}$		$1.19 \cdot 10^{-13}$

acquired preliminarily from one physical sample through tests allowing to characterize its static and dynamic behaviors, were found to read as

$$g(x, v_m) \triangleq a_0 + a_1 \cdot x + b_2 \cdot v_m^2 + c_{2,1} \cdot v_m^2 \cdot x + c_{2,2} \cdot v_m^2 \cdot x^2 + c_{2,3} \cdot v_m^2 \cdot x^3 + c_{2,4} \cdot v_m^2 \cdot x^4 + c_{2,5} \cdot v_m^2 \cdot x^5, \text{ and} \quad (11)$$

$$G(x) \triangleq d_0 + d_1 \cdot x + d_2 \cdot x^2 + d_3 \cdot x^3 + d_4 \cdot x^4 \quad (12)$$

Table 1 reports the values, which our optimisation algorithm assigned to the coefficients of the polynomials in Equations (11) and (12), bringing the iterative procedure to an abrupt successful halt.

If a current is let flow through the nanodevice, its state and voltage response may be predicted via

$$\dot{x} = f(x, i_m), \text{ and} \quad (13)$$

$$v_m = v_m(x, i_m) \triangleq R(x) \cdot i_m \quad (14)$$

with

$$f(x, i_m) \triangleq g(x, v_m(x, i_m)), \text{ and} \quad (15)$$

$$R(x) \triangleq G^{-1}(x) \quad (16)$$

Controlling the device in current, its state evolution function $f(x, i_m)$ and its memristance function $R(x)$ may be retrieved from their equivalents, reported respectively in the state Equation (1) and Ohm's law (2) for the class of extended memristors, after appropriate simplification, through the definitions $f(x, i_m) \triangleq F_{SE}(x, i_m)$ and $R(x) \triangleq F_{OL}(x)$. The next section describes how the device behaves under DC stimulation. This study is a fundamental preliminary step toward the determination of the Local Activity and Edge of Chaos domains of the NaMLab memristor.

4.2. Device DC Response

Analysing the *Dynamic Route Map (DRM)*[36] of the first-order NaMLab threshold switch enables to gain insights into its response to a bias stimulus.

Remark 3. Plotting the rate of change $\dot{x}$ of the volatile memory state x of the first-order NbO_x threshold switch versus the state x itself for a given DC value I_m (V_m) of the current (voltage) stimulus i_m (v_m), and endowing the resulting trace with arrows, pointing to the east (west) on the upper (lower) half plane, results in one *State Dynamic Route (SDR)*[36] for the two-terminal circuit element subject to bias current (voltage) excitation. A SDR from the first (second) kind reveals the time evolution of the volatile memory state x from any initial condition $x_0 \triangleq x(0)$, when a DC source of current I_m (voltage V_m) is connected in parallel to the device, without the need to solve the ordinary differential equation (ODE) (13) (9). Given a certain bias current (voltage) stimulus I_m (V_m), the DC value X, at which the state evolution function $f(x, i_m)$ ($g(x, v_m)$) from Equation (15) (11) admits a zero for $i_m = I_m$ ($v_m = V_m$), represents an admissible operating point Q for the current-driven (voltage-driven) memristor. As a result, the abscissa of any intersection between the $f(x, i_m)$ ($g(x, v_m)$) versus x locus, obtained after assigning I_m (V_m) to i_m (v_m), and the horizontal axis x identifies a possible operating point $Q = X$ for the device under DC current (voltage) stimulation. Irrespective of the nature of the bias stimulus, being in current or voltage form, the local stability (instability) of an operating point Q of the device may be inferred either from the direction of the arrows, lying along the respective $\dot{x}$ versus x locus, as they would point toward (away from) it within its neighborhood, or, alternatively, from the polarity of the slope of the SDR itself, as it would be negative (positive) at its location. The family of SDRs, derived by sweeping the DC value I_m (V_m) of the input signal i_m (v_m) across all real numbers, constitutes the DRM of the device under bias current (voltage) excitation. Inserting all the possible operating points, which the device may ever admit in response to a bias current (voltage) I_m (V_m), into Ohm's law (14) (10), allows to derive each of the admissible values for the voltage (current) V_m (I_m), falling across (flowing through) the two-terminal element, at steady state. These values can then be marked against the respective DC stimulus on the voltage versus current (current versus voltage) plane. Repeating this procedure for each possible current (voltage) stimulus value, a suitable interpolation method can then be used to determine the curve, which best fits the data points marked on the V_m (I_m) versus I_m (V_m) plane in each iteration.

Figure 2a,b shows the circuit employed to test the response of the NaMLab memristor to a bias current (voltage) stimulus I_m (V_m). The DRM of the device under DC current (voltage) excitation is shown in **Figure 3**a,b. The polarity of the DC stimulus, being in current (voltage) form in the first (latter) plot, does not have an impact on the respective DRM, as $f(x, i_m)$ ($g(x, v_m)$) from Equation (15) (11) depends on the square of i_m (v_m). With reference to plot (a), irrespective of the bias current I_m, let flow through the memristor, its state x is found to converge toward one and only one *globally asymptotically stable (GAS)* operating point $Q = X$, as indicated through a filled marker. On the other hand, as illustrated in plot (b) of the same figure, applying a bias voltage V_m across the device, its state x is bound to approach a GAS operating point $Q = X$, exhibiting asymptotic *monostability*, if and only if the modulus of the DC stimulus is chosen outside a specific interval, specifically (0.826 V, 1.007 V). Otherwise, the device admits a triplet of possible operating points, say $Q_1 = X_1$, $Q_2 = X_2$, and $Q_3 = X_3$, of which the outer ones (the inner one), indicated through a filled (hollow) marker, is *locally asymptotically stable (LAS)* (unstable). In these circumstances, the device state x

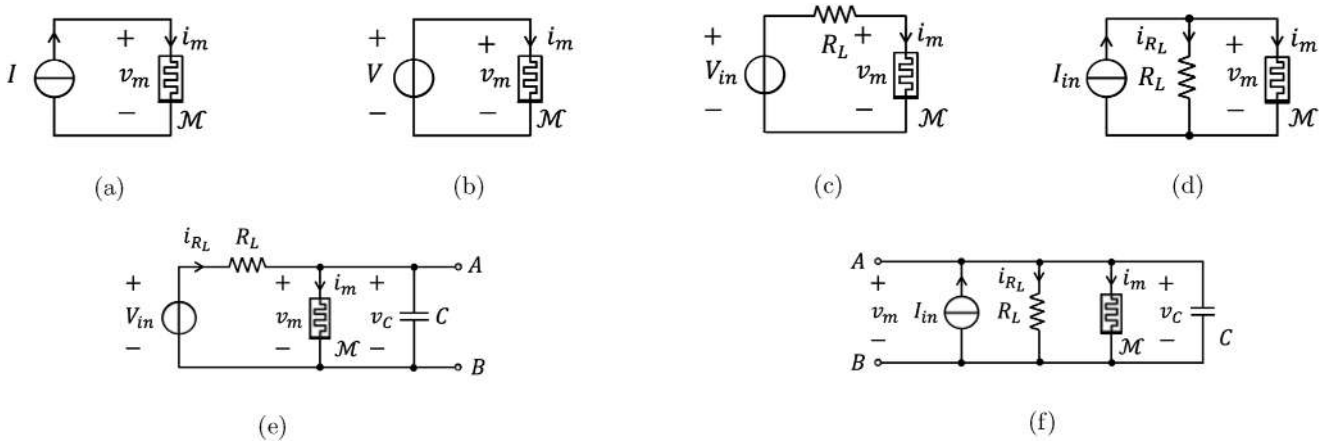

Figure 2. a,b) Circuit set-up to study the DC response of the NbO_x threshold switch to a DC current (voltage) stimulus I (V). c) Circuit set-up for stabilising a NDR bias point $\mathbf{P} = (V_m, I_m)$ of the device subject to a DC voltage stimulus V_{in}. Here the load line $I_m = (V_{in} - V_m)/R_L$ must necessarily go through **P** on the I_m versus V_m plane, and, concurrently, the resistance of the linear resistor R_L has to be chosen larger than the modulus of the inverse of the slope of the DC I_m versus V_m characteristic of the memristor at **P** (see Figure 4c for details). d) Norton representation of the circuit from (c). Here $I_{in} = V_{in}/R_L$. Despite the theorem, enabling the transformation of the voltage-driven one-port in (c) into the equivalent current-driven one-port in (d) is often credited to Norton, it was Mayer who, inspired by a previous work of Thévenin,[34] first introduced it ref. [35]. Clearly, either the circuit in (a), with $I = I_m$, or the circuit in (d), where $I_{in} = I_m + V_m/R_L$, may be alternatively adopted to poise the threshold switch in a NDR operating point $Q = X$. As explained in the main, constraints must be imposed on the bias parameters V_{in} and R_L for stabilizing the memristor on a NDR operating point $Q = X$ of interest. f) Norton equivalent representation of the neuristor from (e), featuring a circuit topology reminiscent of the Hodgkin-Huxley circuit model. The two circuits in (e) and (f) are equivalent one to the other providing $I_{in} = V_{in}/R_L$.

is said to feature steady-state *bistability*, as it is found to sit at the lower (higher) LAS operating point $Q_1 = X_1$ ($Q_3 = X_3$), after transients vanish away, providing its initial condition x_0 is chosen to the left (right) of the intermediate unstable operating point $Q_2 = X_2$.

Importantly, the SDR, extracted from either DRM for zero input, and known as *Power Off Plot (POP)*,[36] sheds light into the volatile memory capability of the NbO_x threshold switch from NaMLab. In fact, since the POP from Figure 3a,b intersects the horizontal axis with negative slope just once, the device is obviously unable to store data under power off conditions, admitting only one GAS operating point, specifically $Q = X = -a_0/a_1 = 253$, when I_m (V_m) is set to zero. The DC voltage V_m versus current I_m (current I_m versus voltage V_m) locus of the NaMLab memristor is shown in Figure 3c,d. Branches with negative slope appear in red. The memristor features a *Negative Differential Resistance (NDR)*, and is locally active, in view of condition (iv) of the Local Activity Theorem from Section 2.1, at any bias point sitting on such branches. Branches, featuring a positive slope, are indicated in black (blue), if the device sits in a bias point at relatively low (high) current, and correspondingly features an operating point commonly referred to as *High (Low) Resistance State*, HRS (LRS) for short, in the literature. At each bias point along branches of this kind the device is said to admit a *Positive Differential Resistance (PDR)*.

With reference to Figure 3c, for each bias current I_m, let flow through the device, one and only one DC voltage V_m may fall between its terminals at steady state, as follows from Ohm's law (14) upon assigning the only GAS operating point $Q = X$, which the device itself may admit in these circumstances according to the DRM analysis of Figure 3a, to the state variable x. As indicated through a solid line style, employed to depict the entire DC V_m versus I_m characteristic in Figure 3c, each device bias point $\mathbf{P} \triangleq (I_m, V_m)$, lying along it, is GAS, as the corresponding operating point $Q = X$. Since the V_m versus I_m locus is a single-valued curve, from a circuit-theoretic viewpoint the NbO_x threshold switch is a *current-controlled device*, and, as a result, the DAE set (13)–(14) is the most appropriate form to cast its model into. Let us now consider the DC voltage stress test once again, and assume, without loss of generality, the polarity of the stimulus V_m to be positive. Assume the bias voltage V_m were chosen outside and to the left (right) of a specific interval, representing the *positive NDR DC voltage range*, and indicated as $(V^{(+)}_{m,NDR,L}, V^{(+)}_{m,NDR,U})$, where, as anticipated earlier, $V^{(+)}_{m,NDR,L} = 0.826$ V and $V^{(+)}_{m,NDR,U} = 1.007$ V. In the first (latter) case, the device current i_m, determined from Ohm's law (10) upon replacing the volatile memory state x with the only GAS operating point $Q = X$, which the state Equation (9) would admit under these hypotheses according to the DRM analysis of Figure 3b, would asymptotically approach one steady-state value I_m, denoting the ordinate of a bias point sitting along the HRS (LRS) black (blue) PDR branch in Figure 3d. However, in case V_m were chosen within the positive NDR DC voltage range, three would be the possible DC currents, flowing through the memristor at steady state, namely $I_{m,1}$, $I_{m,2}$, and $I_{m,3}$, as descending from Ohm's law (10), upon setting the state variable x to the intersections $Q_1 = X_1$, $Q_2 = X_2$, and $Q_3 = X_3$ between the relevant SDR and the horizontal axis in Figure 3b, respectively. As shown in Figure 3d, the smallest (largest) current $I_{m,1}$ ($I_{m,3}$) in this triplet, denotes the ordinate of an admissible bias point, sitting on the HRS (LRS) black (blue) PDR branch, is LAS as the associated operating point $Q_1 = X_1$ ($Q_3 = X_3$), and would be recorded in practice if the state initial condition x_0 were chosen to the left (right) of the unstable operating point $Q_2 = X_2$, which in its turn explains the instability of the other possible bias point, featuring ordinate $I_{m,2}$ and lying along the NDR branch.

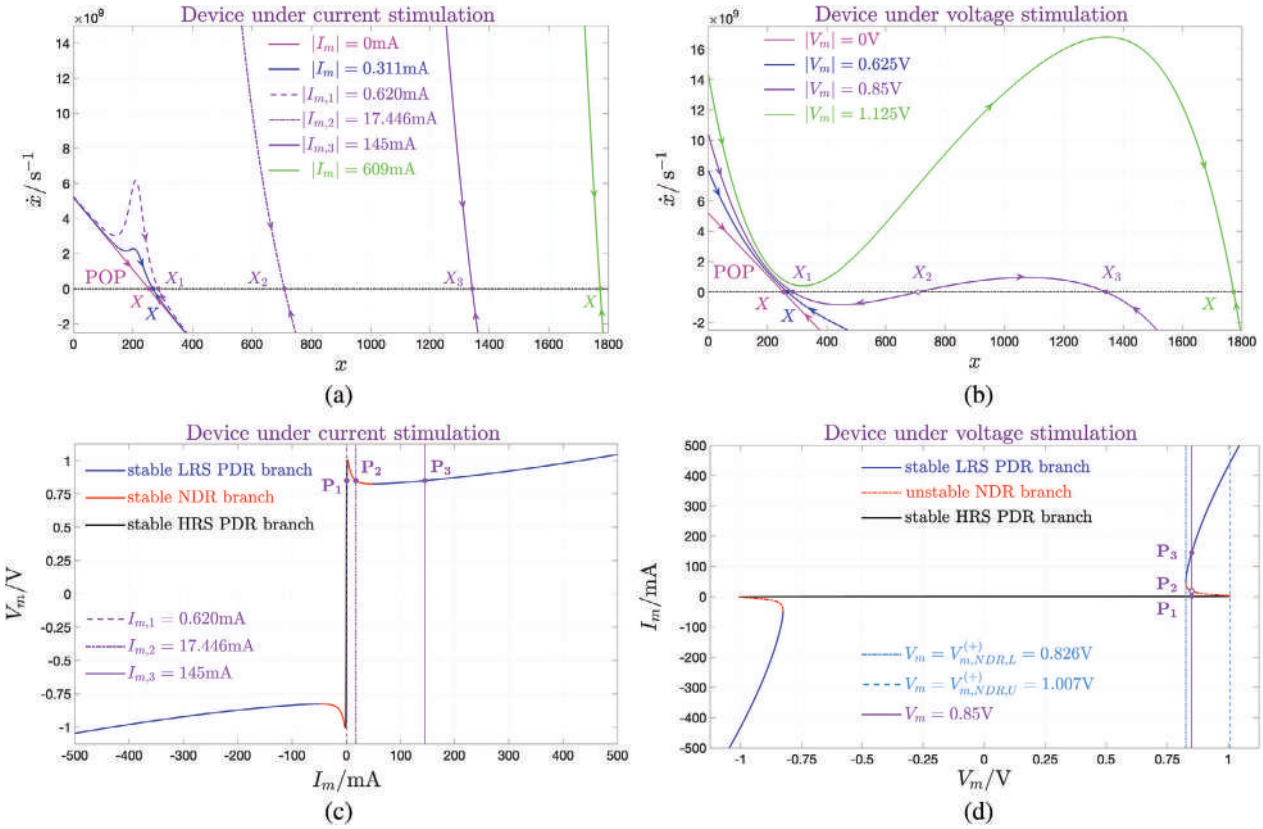

Figure 3. a,b) DRM of the NaMLab memristor under bias current (voltage) sweep. In either DRM, the SDR, associated to a given bias stimulus, is independent of its polarity, due to the quadratic dependence of the respective state evolution function upon the input variable. The magenta trace in (a,b), denoting the SDR of the current-driven (voltage-driven) device under power-off conditions, reveals its volatile memory capability. As may be inferred from the first, second, and third violet SDRs, drawn as dashed, dash-dotted, and solid traces, respectively, in plot (a), $X_1 = 285$, $X_2 = 709$, and $X_3 = 1342$ are GAS DC states, which may be respectively programmed into the device by setting the modulus of the DC current stimulus I from Figure 2a to the 1st, 2nd, and 3rd $|I_m|$ value in the triplet $\{|I_{m,1}| = 0.620$ mA, $|I_{m,2}| = 17.446$ mA, $|I_{m,3}| = 145$ mA$\}$. In each of the 3 DC current excitation scenarios, the modulus of the device voltage V_m is found to attain the value of 0.85 V, at steady state. Fixing the modulus of the bias voltage stimulus V from Figure 2b to $|V_m| = 0.85$ V, which falls in the bistability domain (0.826,1.007)V of the threshold switch under voltage excitation, allows to stabilize the threshold switch at either of the two outer operating points $X_1 = 285$ and $X_3 = 1342$, only, since the inner operating point $X_2 = 709$ is unstable and thus unaccessible, as may be inferred by inspecting the solid violet SDR in plot (b). c,d) DC V_m versus I_m (I_m versus V_m) characteristic of the NaMLab memristor for $I_m \in (-500$ mA, 500 mA) ($V_m \in (-1.046$ V, 1.046 V)), when, correspondingly, the DC state X covers the span of values specified as (253,1722). In either DC locus, black (blue) traces represent HRS (LRS) PDR branches, while a red color is used to mark NDR regions. In (c), the j^{th} violet vertical load line $i_m = I_{m,j}$, drawn as a dashed, dash-dotted, and solid trace when the index j is respectively set to 1, 2, and 3, is found to cross the memristor V_m versus I_m characteristic only once, identifying a unique GAS bias point $\mathbf{P_j} = (I_{m,j}, V_{m,j})$, with $V_{m,j}$ fixed to 0.85 V irrespective of j, which allows to poise the memristor on a specific GAS DC state X_j, corresponding to the crossing between the j^{th} violet SDR and the horizontal axis in (a). In (d) the violet vertical DC load line $v_m = V_m$, lying within the positive NDR DC voltage range, crosses the memristor I_m versus V_m characteristic three times, identifying a triplet of possible operating points for the device, of which $\mathbf{P_1} = (V_{m,1} = V_m, I_{m,1})$ and $\mathbf{P_3} = (V_{m,3} = V_m, I_{m,3})$, lying in turn on the HRS PDR branch and on the LRS PDR branch, are LAS, as the corresponding operating points X_1 and X_3, respectively, while $\mathbf{P_2} = (V_{m,2} = V_m, I_{m,2})$, sitting along the NDR branch, is unstable, as the associated DC state X_2 (refer also to the violet SDR in (b)). $|V_m| \in (0.826, 1.007)$V defines the bistability domain of the NaMLab memristor under voltage stimulation.

Remark 4. Importantly, in the bistability regime of the device under positive voltage excitation, i.e., when V_m falls in the positive NDR DC voltage range $(V^{(+)}_{m,NDR,L}, V^{(+)}_{m,NDR,U})$, I_m assumes values within the *positive NDR DC current range*, which is indicated as $(I^{(+)}_{m,NDR,L}, I^{(+)}_{m,NDR,U})$, where $I^{(+)}_{m,NDR,L} = 2.037$ mA and $I^{(+)}_{m,NDR,U} = 49.296$ mA. Concurrently, $Q = X$ varies across the *NDR operating point or DC state range*, which is independent of the polarity of the voltage stimulus, and indicated as $(Q_{NDR,L}, Q_{NDR,U})$, with $Q_{NDR,L} = X_{NDR,L} = 351$ and $Q_{NDR,U} = X_{NDR,U} = 1006$. Note that, due to the negative slope of the NDR branch in the first quadrant of the I_m versus V_m plane of Figure 3d, the lower (upper) bound $V^{(+)}_{m,NDR,L}$ ($V^{(+)}_{m,NDR,U}$) in the positive NDR DC voltage range corresponds to the upper (lower) bound $I^{(+)}_{m,NDR,U}$ ($I^{(+)}_{m,NDR,L}$) for the positive NDR DC current. Moreover, since the memristor NDR operating point Q increases monotonically with the positive DC current I_m (see **Figure 4a**), when $V_m = V^{(+)}_{m,NDR,L}$ ($V_m = V^{(+)}_{m,NDR,U}$), then $Q = Q_{NDR,U}$ ($Q = Q_{NDR,L}$).

Similar conclusions apply *mutatis mutandis* to the response of the device to a negative-valued DC voltage stimulus. All in all,

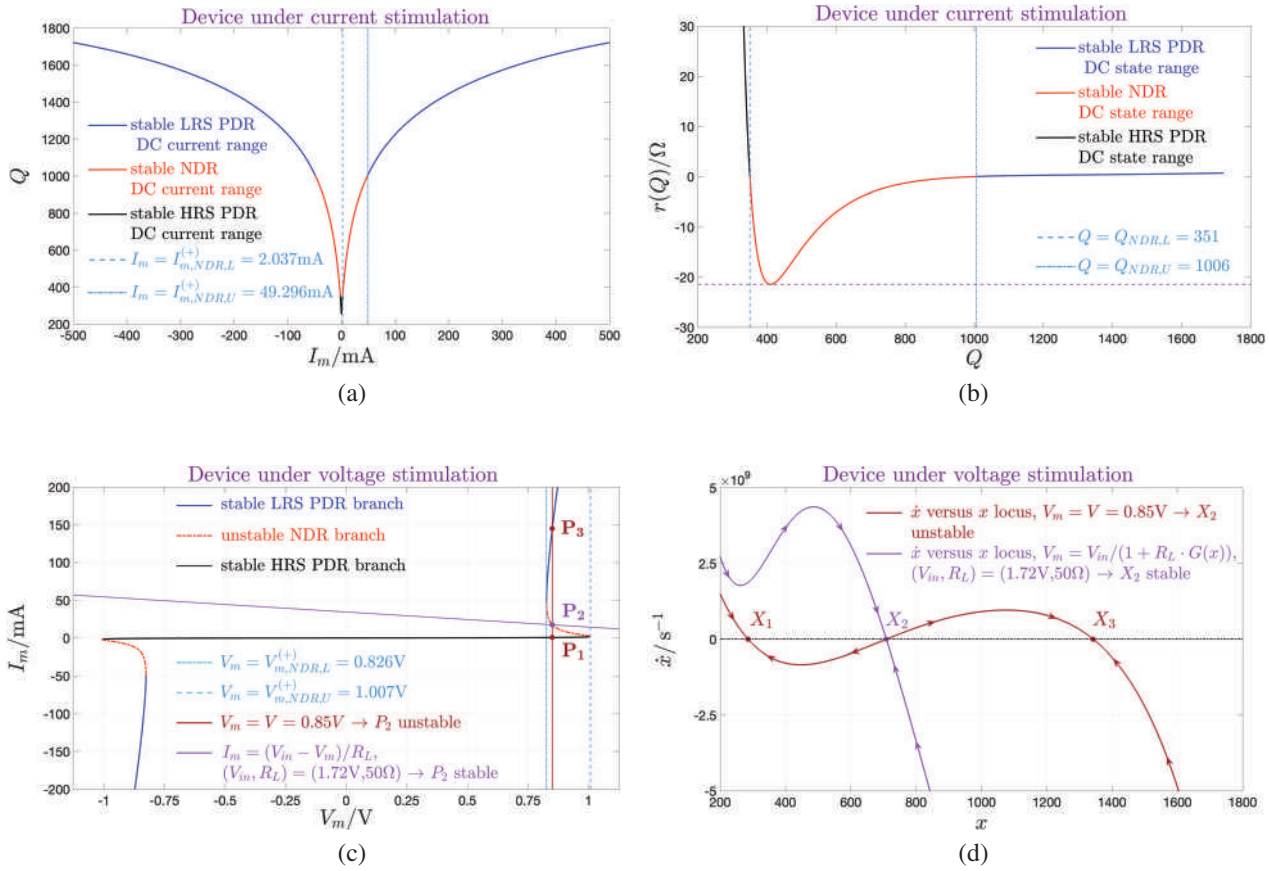

Figure 4. a) DC state X versus DC current I_m locus of the threshold switch under current excitation. b) Dependence of the small-signal resistance r of the current-driven device upon its operating point Q. Importantly, $r(Q)$ is identically equal to the slope of the memristor DC V_m versus I_m characteristic at the bias point **P**, which is unequivocally associated to the operating point Q of interest. Importantly, $r(Q = 411) = -\max_{Q\in(Q_{NDR,L},Q_{NDR,U})}|r(Q)| = -21.427\ \Omega$. Section 4.3 will show how to determine r at some Q through a straightforward circuit-theoretic analysis. c,d) Brown trace: Load line (Memristor SDR) in the circuit of Figure 2(b) for $V_m = 0.85$ V, which falls in the bistability domain $(V^{(+)}_{m,NDR,L}, V^{(+)}_{m,NDR,U}) = (0.826, 1.007)$V of the threshold switch under voltage excitation. Brown filled circles mark in (c,d) the two crossings between the brown-colored load line and the DC I_m versus V_m characteristic (the brown-colored memristor SDR and the horizontal line), which correspond to the LAS bias points $\mathbf{P_1}$ and $\mathbf{P_3}$ (LAS operating points $Q_1 = X_1$ and $Q_3 = X_3$) for the nanodevice. c,d) Violet trace: Load line (Memristor SDR) in the circuit of Figure 2c for $V_{in} = 1.72$ V and $R_L = 50\ \Omega$. A violet filled circle marks in (c,d) the only intersection between the violet-colored load line and the DC I_m versus V_m characteristic (the violet-colored memristor SDR and the horizontal line), which appears at the earlier unstable and now GAS bias point $\mathbf{P_2}$ (operating point $Q_2 = X_2$) for the NaMLab memristor. Thus the insertion of a resistor R_L of resistance larger than $|r(Q)|$ between the voltage stimulus V_{in}, chosen equal to $V_m \cdot (1 + R_L \cdot G(Q))$, and the NaMLab memristor enables to stabilize any of its NDR bias points, say $\mathbf{P} = (V_m, I_m)$, or equivalently any of its operating points, say $Q = X$, which would have been otherwise unstable had a source of DC voltage V_m been directly placed across the device.

as indicated via a solid (dash-dotted) line style along the DC I_m versus V_m characteristic of Figure 3d, a bias point $\mathbf{P} \triangleq (V_m, I_m)$, sitting on a black HRS or blue LRS PDR branch (on a red NDR branch) is either LAS if $|V_m|$ falls within the *bistability domain of the voltage-driven device*, i.e., inside the range $(V^{(+)}_{m,NDR,L}, V^{(+)}_{m,NDR,U})$, or GAS otherwise (is unstable).

4.2.1. Stabilization of a NDR Operating Point for the Threshold Switch Uunder Voltage Stimulation

Since the existence of NDR branches in the DC characteristic of a memristor is a signature for its capability to amplify infinitesimal fluctuations in energy at bias points, lying along them, their instability under voltage sweep is detrimental for locally-active circuit design.[24] However, inserting a linear resistor R_L in series with the DC voltage stimulus, here renamed V_{in}, as shown in Figure 2c, allows to stabilize a given NDR bias point $\mathbf{P} = (V_m, I_m)$ of the device under suitable conditions on the choice of the two bias parameters.[37] First of all, the bias parameter pair (V_{in}, R_L) needs to be selected in such a way that the load line $I_m = (V_{in} - V_m)/R_L$ for the memristor in the new bias circuit from Figure 2c goes through its NDR bias point **P** under stabilization on the I_m versus V_m plane. This is necessary, yet not quite sufficient. It is also fundamental to choose the series resistance in such a way to satisfy the inequality $R_L > |r(Q)|$, with $r(Q)$ denoting the negative-valued inverse of the slope of the DC I_m versus V_m characteristic at a specific NDR bias point $\mathbf{P} = (V_m, I_m)$ corresponding to a particular operating point Q, falling inside the NDR DC state range $(Q_{NDR,\,L}, Q_{NDR,\,U})$, and subject to the stabilization procedure. In

other words, the modulus of the slope of the memristor DC locus at **P** must be larger than the modulus of the slope of the load line. Once the just mentioned conditions are satisfied, the NDR bias point **P** of interest becomes the only crossing point between the I_m-V_m characteristic and the load line. Correspondingly, the state Equation (9), in which the device voltage v_m depends nonlinearly upon the state x according to the closed-form expression $v_m = V_{in}/(1 + G(x) \cdot R_L)$, where $G(x)$ denotes the memductance function from Equation (12), is found to admit a GAS operating point Q. Figure 4c shows how the NDR bias point $\mathbf{P}_2 = (V_{m,2}, I_{m,2})$, featuring abscissa $V_{m,2} = V_m = 0.85$ V, ordinate $I_{m,2} = 17.446$ mA, and an unstable nature in the circuit of Figure 2(b), becomes GAS in the circuit of Figure 2c upon setting V_{in} and R_L to 1.72 V and 50 Ω, respectively. Correspondingly, as illustrated in Figure 4(d), the SDR crosses the horizontal axis with negative slope only at the DC state $Q_2 = X_2 = 709$, changing its stability properties relative to what was the case in the circuit of Figure 2b. It is worth observing that the Thévenin NDR stabilisation circuit in plot (c) of Figure 2 could be equivalently replaced by its Norton form, as shown in plot (d) of the same figure. With reference to the case study endowing the memristor in the Thévenin cell with the violet SDR from Figure 4d, the bias parameter pair of the equivalent Norton circuit should be set to $(I_{in}, R_L) = (34.4$ mA, 50 Ω). As a final remark, in order to stabilize the entire NDR branch of the device under voltage stimulation, the series resistance R_S should be chosen in such as way that $R_L > \max_{\forall Q \in (Q_{NDR,L}, Q_{NDR,U})}\{|r(Q)|\}$. As may be inferred from the $r(Q)$ versus Q locus of Figure 4b, a series resistance larger than 21.427 Ω serves this purpose.

4.3. Device Small-Signal Model

Having acquired an in-depth understanding of the device response to DC excitation, we are now ready to analyze its small-signal behavior. This is yet another crucial step toward the identification of the Local Activity and Edge of Chaos domains of the NbO_x threshold switch. Let us consider, without loss of generality, the voltage-driven model form (9)–(10). Developing $g(x, v_m)$ from Equation (11) and $i_m(x, v_m)$, with $G(x)$ expressed by (12), in Taylor series about a given operating point $Q = X$, corresponding unequivocally to a bias point $\mathbf{P} = (V_m, I_m)$ on the DC I_m versus V_m characteristic, and truncating the resulting expansions to the first order, yields the device small-signal model, taking the form

$$\delta\dot{x} = a(Q) \cdot \delta x + b(Q) \cdot \delta v_m, \text{ and} \tag{17}$$

$$\delta i_m = c(Q) \cdot \delta x + d(Q) \cdot \delta v_m \tag{18}$$

where δx and δi_m respectively represent the infinitesimal state and current response of the memristor to the tiny voltage signal δv_m, superimposed on the bias stimulus V_m, while, deriving the components of the Jacobian matrix, the Q-dependent expressions for the local parameters are found to read as

$$a(Q) \triangleq \left.\frac{\partial g(x, v_m)}{\partial x}\right|_{Q=X} = a_1 + \left(c_{2,1} + 2 \cdot c_{2,2} \cdot X + 3 \cdot c_{2,3} \cdot X^2 + 4 \cdot c_{2,4} \cdot X^3 + 5 \cdot c_{2,5} \cdot X^4\right) \cdot V_m^2 \tag{19}$$

$$b(Q) \triangleq \left.\frac{\partial g(x, v_m)}{\partial v}\right|_{Q=X} = 2 \cdot \left(b_2 + c_{2,1} \cdot X + c_{2,2} \cdot X^2 + c_{2,3} \cdot X^3 + c_{2,4} \cdot X^4 + c_{2,5} \cdot X^5\right) \cdot V_m \tag{20}$$

$$c(Q) \triangleq \left.\frac{\partial i_m(x, v_m)}{\partial x}\right|_{Q=X} = \left(d_1 + 2 \cdot d_2 \cdot X + 3 \cdot d_3 \cdot X^2 + 4 \cdot d_4 \cdot X^3\right) \cdot V_m, \text{ and} \tag{21}$$

$$d(Q) \triangleq \left.\frac{\partial i_m(x, v_m)}{\partial v}\right|_{Q=X} = d_0 + d_1 \cdot X + d_2 \cdot X^2 + d_3 \cdot X^3 + d_4 \cdot X^4 \equiv G(X) \tag{22}$$

Transforming the small-signal model (17)–(18) into the Laplace domain, with $\delta x_0 \triangleq \delta x(0) = 0$, and performing some algebraic manipulations, allows to determine a closed-form expression for the memristor small-signal transfer function $H(s; Q)$, which under voltage stimulation, assumes the admittance form

$$Y(s; Q) \triangleq \left.\frac{\mathcal{L}\{\delta i_m(t)\}}{\mathcal{L}\{\delta v_m(t)\}}\right|_Q = K_Y(Q) \cdot \frac{s - z_Y(Q)}{s - p_Y(Q)} \tag{23}$$

where the factor, scaling the rational function, the zero, and the pole are respectively expressed by

$$K_Y(Q) = \frac{1}{r_1(Q)} \tag{24}$$

$$z_Y(Q) = -\frac{r_1(Q) + r_2(Q)}{l(Q)}, \text{ and} \tag{25}$$

$$p_Y(Q) = -\frac{r_2(Q)}{l(Q)} \tag{26}$$

where $r_1(Q)$, $r_2(Q)$, and $l(Q)$, in turn defined as

$$r_1(Q) = \frac{1}{d(Q)} \tag{27}$$

$$r_2(Q) = -\frac{a(Q)}{b(Q) \cdot c(Q)}, \text{ and} \tag{28}$$

$$l(Q) = \frac{1}{b(Q) \cdot c(Q)} \tag{29}$$

denote the Q-dependent two-terminal circuit elements of the linear one-port, depicted in **Figure 5**a, and featuring the very same admittance $Y(s; Q)$ reported in Equation (23). Plots (c), (d), and (e) in Figure 5 show how the values for $r_1(Q)$, $|r_2(Q)|$, and $l(Q)$ change with the device operating point Q. Importantly, $r_2(Q)$ goes negative throughout the NDR operating point range $(Q_{NDR,L}, Q_{NDR,U})$. Inspecting the small-signal circuit model from Figure 5(a) in the limit for $s \to 0$, the local conductance of the memristor, which is equivalent to the slope of its V_m versus I_m locus, may be computed via $\lim_{s \to 0} Y(s; Q) = r^{-1}(Q)$, where

$$r(Q) \triangleq r_1(Q) \parallel r_2(Q) \tag{30}$$

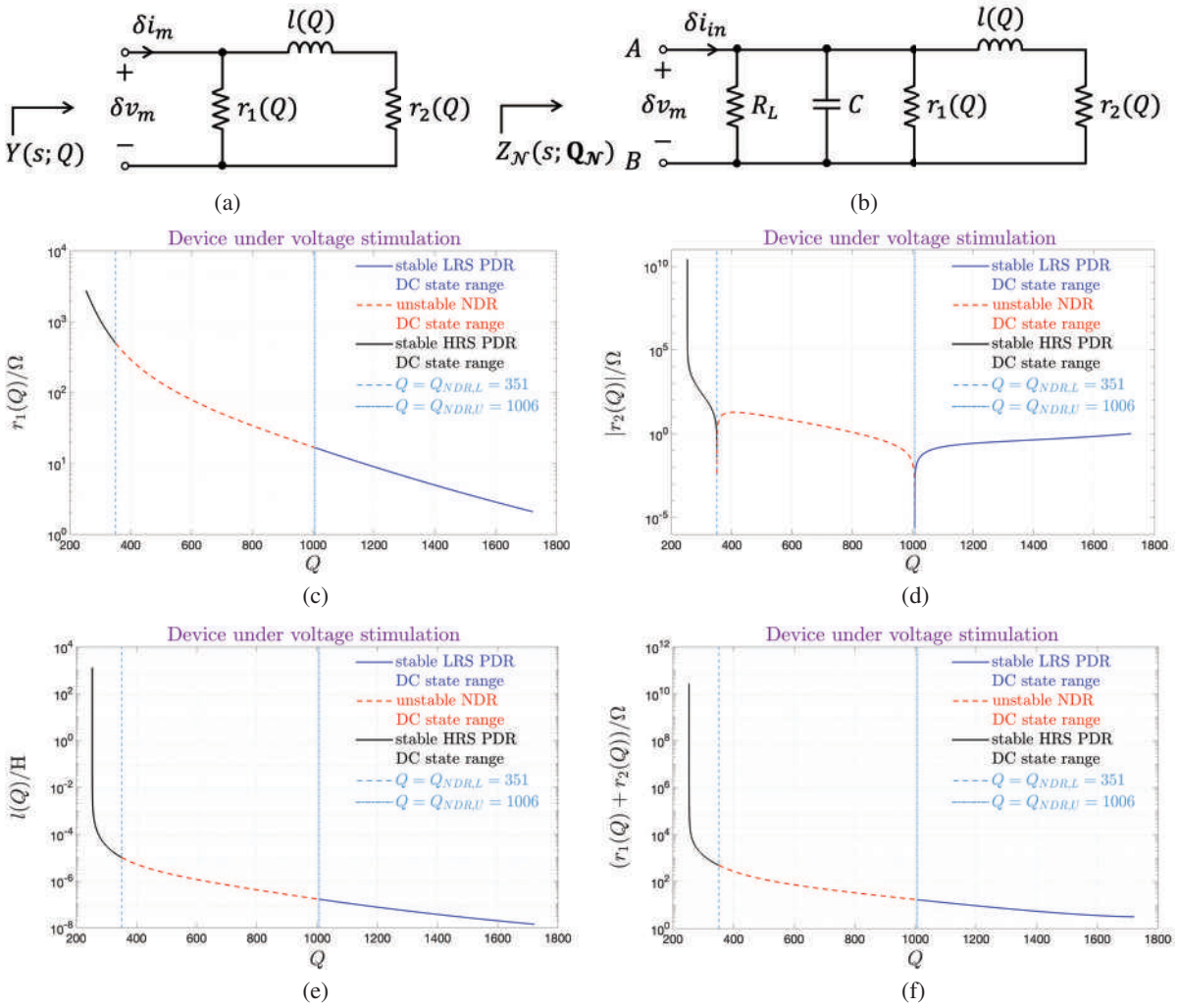

Figure 5. a) Equivalent circuit-theoretic representation of the small-signal or local memristor model. It is a linear one-port, consisting of the parallel combination between a resistance $r_1(Q)$ and a resistance $r_2(Q)$-inductance $l(Q)$ series one-port.[38] b) Small-signal or local model of the NaMLab Hodgkin-Huxley Neuristor in the Thévenin (Norton) form from plot (e,f) of Figure 2 about a generic operating point $\mathbf{Q}_{\mathcal{N}} = (Q, V_m)$. Here $Z_{\mathcal{N}}$ denotes the small-signal impedance of either of the two neuristor topologies at the respective input port *A*–*B*. (c–f) Illustrations showing how the values of the parameters of the memristor local circuit in plot (a) vary as the device operating point $Q = X$ is swept across the range (253,1722), when correspondingly the DC voltage V_m covers the interval (−1.046 V, 1.046 V) and the DC current I_m assumes values across the set (−500 mA, 500 mA). The local stability properties of the operating points of the memristor are indicated under the assumption that a DC voltage is let fall across its two terminals. (c) $r_1(Q)$ versus Q. d) $|r_2(Q)|$ versus Q. Importantly, $r_2(Q)$ is negative for $Q \in (Q_{NDR,\,L}, Q_{NDR,\,U})$, and positive elsewhere. e) $l(Q)$ versus Q. (f) $r_1(Q) + r_2(Q)$ versus Q.

stands for the device local resistance (recall Figure 4b). Also, the device acts as a linear conductance in response to small-signal stimuli at very high frequencies, as may be evinced by computing the limit of its local admittance for $s \to \infty$, which gives $\lim_{s\to\infty} Y(s; Q) = G(Q)$.

4.4. Local Activity and Edge of Chaos in the NaMLab Memristor

As shown in plot (a) of **Figure 6**, the pole $p_Y(Q)$ of the memristor local admittance $Y(s; Q)$ is positive within the NDR operating point range $(Q_{NDR,\,L}, Q_{NDR,\,U})$, and negative elsewhere. On the other hand, since the sum of the resistances $r_1(Q)$ and $r_2(Q)$ in the memristor local circuit model is strictly positive (refer to Figure 5f), the zero $z_Y(Q)$ of $Y(s; Q)$ keeps negative, irrespective of Q, as illustrated in plot (b) of Figure 6. Furthermore, the real part $\Re\{Y(s; Q)\}$ of the memristor local admittance $Y(s; Q)$ about an operating point Q, reading for $s = j\omega$ as

$$\Re\{Y(j\omega; Q)\} = K_Y(Q) \cdot \frac{\omega^2 + z_Y(Q) \cdot p_Y(Q)}{\omega^2 + p_Y^2(Q)} \tag{31}$$

goes negative across the range of angular frequencies

$$|\omega_{0,Y}(Q)| < \omega_{0,Y,\max}(Q) \triangleq \frac{1}{l(Q)} \cdot \sqrt{-r_2(Q) \cdot (r_1(Q) + r_2(Q))} \tag{32}$$

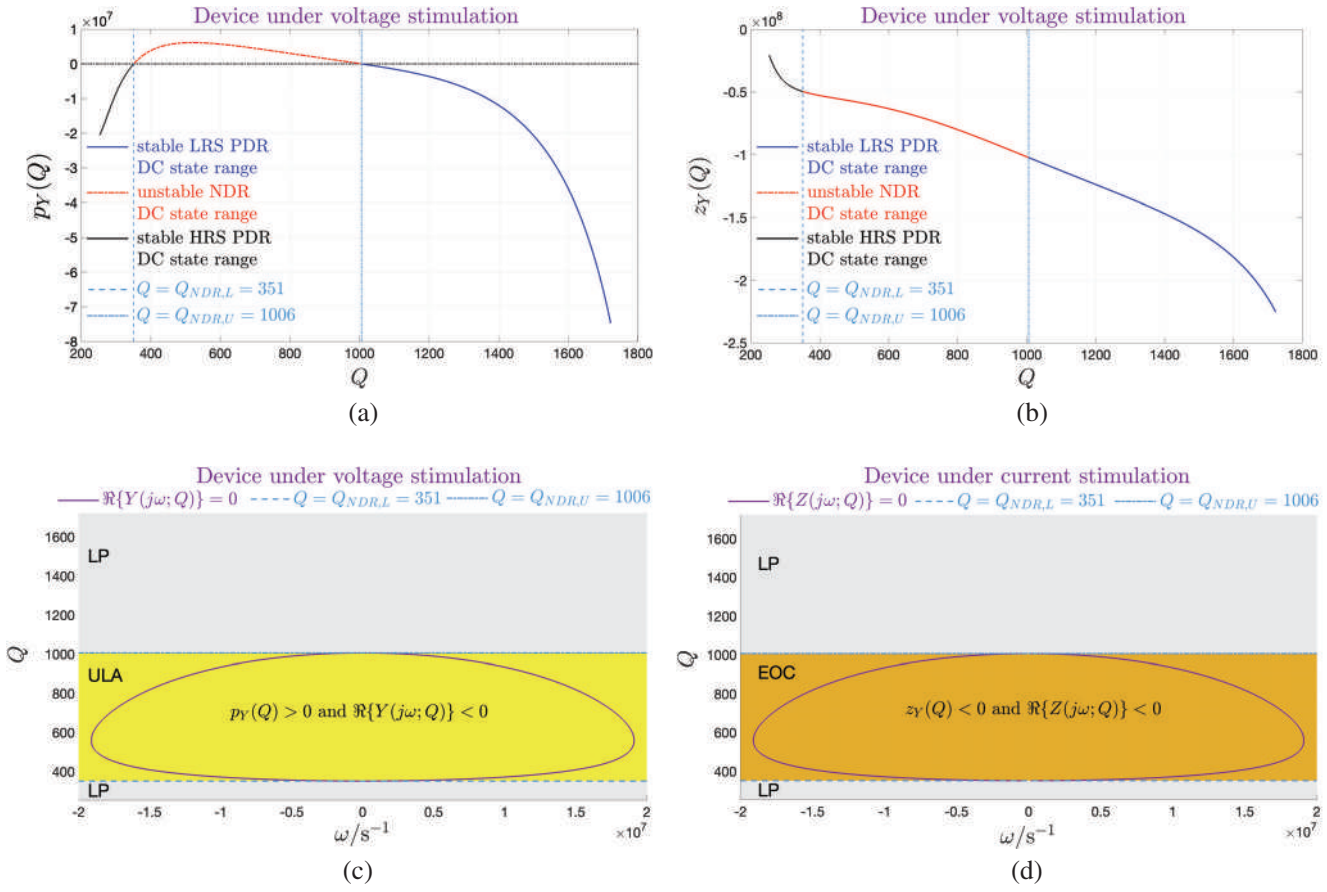

Figure 6. a,b) Locus of the pole $p_Y(Q)$ (zero $z_Y(Q)$) of the memristor local admittance $Y(s; Q)$ versus the respective operating point Q, providing insights into the local stability properties of all the admissible bias points of the device under voltage (current) stimulation. c,d) Partition of the operating point Q versus angular frequency ω plane into domains of different polarization regimes for the memristor under voltage (current) excitation. Irrespective of the nature of the excitation, being a voltage or a current bias signal, the bottom and top grey regions in both (c) and (d) represent the Local Passivity (LP) domains, stretching across the HRS PDR and LRS PDR operating point ranges, respectively. In (c,d) the yellow (ochre) region, where conditions (i) and (iv) of the Local Activity Theorem from Section 2.1 (conditions (j) and (jj) of the Edge of Chaos Corollary from Section 2.2) hold true for $Y(s; Q)$ ($Z(s; Q)$), is the Unstable Local Activity (ULA) (Edge of Chaos (EOC)) domain, covering the NDR operating point range ($Q_{NDR,\,L}$, $Q_{NDR,\,U}$), for the voltage-driven (current-driven) device. In (c,d) $\Re\{Y(j\omega; Q)\}$ ($\Re\{Z(j\omega; Q)\}$) goes negative within the region of the Q versus ω plane lying inside the closed violet curve.

provided the radicand is real-valued, implying the necessity for Q to lie inside the NDR operating point range ($Q_{NDR,\,L}$, $Q_{NDR,\,U}$). For a one-port the local impedance $Z(s; Q)$ is identically equal to the inverse $Y^{-1}(s; Q)$ of the local admittance $Y(s; Q)$. The local impedance of the NaMLab threshold switch may be cast in the form $Z(s; Q) = K_Z(Q) \cdot (s - z_Z(Q))/(s - p_Z(Q))$. The factor scaling the rational function is computable via $K_Z(Q) = 1/K_Y(Q)$. Most importantly, the pole (zero) $p_Z(Q)$ ($z_Z(Q)$) of $Z(s; Q)$ coincides with the zero (pole) $z_Y(Q)$ ($p_Y(Q)$) of $Y(s; Q)$ Moreover, *the conditions, ensuring the real part* $\Re\{Z(j\omega; Q)\}$ of $Z(j\omega; Q)$ is negative, are the very same, guaranteeing a negative sign for the real part $\Re\{Y(j\omega; Q)\}$ of $Y(j\omega; Q)$. In mathematical form, $\Re\{Z(j\omega; Q)\}$ goes negative across the range of angular frequencies $|\omega_{0,\,Z}(Q)|$

$$|\omega_{0,Z}(Q)| < \omega_{0,Z,\max}(Q) \triangleq \frac{1}{l(Q)} \cdot \sqrt{-r_2(Q) \cdot (r_1(Q) + r_2(Q))} \quad (33)$$

Invoking now the Local Activity Theorem and the Edge of Chaos Corollary, enunciated in Sections 2.1 and 2.2, respectively, definitive conclusions, as enumerated below, may be drawn in regard to the admissible operating regimes for the NbO_x threshold switch.

1. Under voltage stimulation, the device is locally active yet unstable (locally passive) at any bias point sitting along the NDR branches (along either the HRS or the LRS PDR branches), as shown in plot (c) of Figure 6.
2. Under current stimulation, the device is locally active and stable i.e. on the Edge of Chaos (locally passive) at any bias point along the NDR branches (along either the HRS or the LRS PDR branches), as illustrated in plot (d) of Figure 6.

It is simple to demonstrate that the resistor R_L-memristor $\mathcal{M}$ series one-port, whose voltage and current are respectively definable as $\tilde{v}_m \triangleq v_m + R_L \cdot i_m$ and $\tilde{i}_m \triangleq i_m$, is strictly locally-passive about the respective operating point, expressed via $\tilde{Q} \triangleq Q$, irrespective of the nature of the stimulus, being either in voltage or in current form, providing the inequality $R_L > \max_{\forall Q \in (Q_{NDR,L}, Q_{NDR,U})} |r(Q)|$ holds true. In fact, the local admittance $\tilde{Y}(j\omega, \tilde{Q})$ of the $1\mathcal{M}$-$1R_L$ series one-port about its operating point

$\tilde{Q}$ assumes the form

$$\tilde{Y}(j\omega, \tilde{Q}) \triangleq \frac{\mathcal{L}\{\delta\tilde{i}_m(t)\}}{\mathcal{L}\{\delta\tilde{v}_m(t)\}}\bigg|_{\tilde{Q}} = K_{\tilde{Y}}(\tilde{Q}) \cdot \frac{s - z_{\tilde{Y}}(\tilde{Q})}{s - p_{\tilde{Y}}(\tilde{Q})} \quad \text{where}$$

$$K_{\tilde{Y}}(\tilde{Q}) = K_{\tilde{Y}}(Q) = \frac{1}{r_1(Q) + R_L}$$

$$z_{\tilde{Y}}(\tilde{Q}) = z_{\tilde{Y}}(Q) = -\frac{r_1(Q) + r_2(Q)}{l(Q)}, \quad \text{and}$$

$$p_{\tilde{Y}}(\tilde{Q}) = p_{\tilde{Y}}(Q) = -\frac{R_L \cdot (r_1(Q) + r_2(Q)) + r_1(Q) \cdot r_2(Q)}{l(Q) \cdot (r_1(Q) + R_L)} \tag{34}$$

Provided the inequality $R_L > \max_{\forall Q \in (Q_{NDR,L}, Q_{NDR,U})} |r(Q)|$ applies, $\tilde{Y}(j\omega, \tilde{Q})$ admits a strictly negative real part $\Re\{\tilde{Y}(j\omega, \tilde{Q})\}$ irrespective of the angular frequency ω, while concurrently both its zero $z_{\tilde{Y}}(\tilde{Q})$ and its pole $p_{\tilde{Y}}(\tilde{Q})$ lie on the OLHP. In particular, choosing appropriate values for V_{in} and R_L in the circuit of Figure 2c, controlling the $1\mathcal{M}$-$1R_L$ series one-port in voltage, it is possible to poise it on a locally-passive operating point $\tilde{Q}$, while concurrently stabilising the respective threshold switch on a bias point $\mathbf{P} = (V_m, I_m)$ lying along a NDR branch of the respective DC current versus voltage characteristic.

Remark 5. Let us assume a DC current stimulus I_m to flow through the NaMLab threshold switch from $t = 0$. Suppose that, after transients fade away, the volatile memristor is found to sit on a stable and locally-active bias point $\mathbf{P} = (I_m, V_m)$ along a NDR branch of its voltage versus current characteristic. Also, let an infinitesimal sine-wave current signal of the form $\delta i_m = \delta\hat{i}_m \cdot \sin(\omega_* \cdot t + \angle\delta i_m)$ with $\angle\delta i_m = -\omega_* \cdot t_0$ flow through the NaMLab threshold switch from a time instant $t = t_0$, so much larger than 0 that the device would have settled to the aforementioned bias point by then. Assuming $\delta\hat{i}_m$ to be smaller than I_m by several orders of magnitude, the small-signal voltage, falling across the memristor in response to the local current stimulus from $t = t_0$, may be approximately computed via $\delta v_m = \delta\hat{v}_m \cdot \sin(\omega_* \cdot t + \angle\delta v_m)$, where $\delta\hat{v}_m = |Z(j\omega_*; Q)| \cdot \delta\hat{i}_m$ and $\angle\delta v_m = \angle\delta i_m + \angle Z(j\omega_*; Q)$, where $\angle Z(j\omega_*; Q) = \arctan(\Im\{Z(j\omega_*; Q)\}/\Re\{Z(j\omega_*; Q)\}) + \pi/2 \cdot (1 - \text{sign}(\Re\{Z(j\omega_*; Q)\}))$. Clearly, the modulus of the phase difference between the small-signal current stimulus δi_m and the resulting infinitesimal voltage response δv_m lies between 90° and 270° if and only if condition (iv) of the Local Activity Theorem from Section 2.1 holds true for the memristor local impedance Z evaluated about Q at the input angular frequency ω_*. Importantly, the net local energy $\delta\mathcal{E}$ absorbed by the threshold switch, biased at Q, over the time frame (t_0, t), is computable via

$$\begin{aligned}\delta\mathcal{E}(t_0, t; Q) &= \frac{1}{2} \cdot \delta\hat{v}_m \cdot \delta\hat{i}_m \cdot \Big[\cos(\angle\delta v_m - \angle\delta i_m) \cdot (t - t_0) \\ &- \big(\sin(2 \cdot \omega_* \cdot (t - t_0) + \angle\delta v_m + \angle\delta i_m) \\ &- \sin(\angle\delta v_m + \angle\delta i_m)\big) \cdot \frac{1}{2} \cdot \omega_*\Big]\end{aligned} \tag{35}$$

Clearly, over any input cycle, i.e., across a generic T_*-long time interval $(t_i, t_i + T_*)$, where $t_i \geq t_0$, the memristor shall absorb a net local energy which may be estimated via

$$\begin{aligned}\delta\mathcal{E}(t_i, t_i + T_*; Q) &= \frac{1}{2} \cdot \hat{v}_m \cdot \hat{i}_m \cdot T_* \cdot \cos(\angle\delta v_m - \angle\delta i_m) \\ &= \frac{1}{2} \cdot |Z(j\omega_*; Q)| \cdot \delta\hat{i}_m^2 \cdot T_* \\ &\quad \cdot \cos(\angle Z(j\omega_*; Q))\end{aligned} \tag{36}$$

where $T_* = 1/f_*$, while $f_* = \omega_*/(2 \cdot \pi)$ stands for the frequency of the infinitesimal perturbation. As long as the modulus of the phase shift between δi_m and δv_m is between 90° and 270°, which is the case if and only if $\Re\{Z(j\omega_*; Q)\} < 0$, does the memristor provide the excitation source, which imposes the current flowing between its terminals, with an infinitesimal amount of energy of modulus $|\delta\mathcal{E}(t_0, t_0 + T_*; Q)|$, with $\delta\mathcal{E}(t_0, t_0 + T_*; Q)$ expressed by Equation (36), over each T_*-long cycle of its small-signal sinusoidal current stimulus. Last but not least, from a basic inspection of the memristor small-signal equivalent circuit model of Figure 5a, it is easy to realize that the phase of the threshold switch local impedance evaluated about any of its NDR operating points is a monotonically decreasing function of the frequency, descending from 180° to 0° as the frequency increases from zero to positive infinity.

Figure 7 shows simulation results illustrating the important theoretical concepts presented in this remark. In particular, using the circuit set-up from Figure 2a, a DC current I equal to 17.446 mA was let flow through the threshold switch from $t = 0$. With I_m identically equal to I, the device was found to approach the GAS operating point $Q = 709$ after transients faded away (recall plots (a) and (c) of Figure 3). In fact, it can be assumed the memristor to sit at the aforementioned operating point at time $t = 1$ µs, as demonstrated in Figure 7a. From this time instant, labelled t_0 in the analysis to follow, a small-signal input current δi of amplitude $\delta\hat{i} = 10$ µA, phase $\angle\delta i = -\omega_* \cdot t_0$, and angular frequency $\omega_* = 2 \cdot \pi \cdot f_*$ was injected into the memristor together with the DC bias stimulus I. The blue and red traces in plot (b,c) of Figure 7 respectively show the local memristor current δi_m, identically equal to the small-signal stimulus δi, and the local voltage δv_m, which is correspondingly found to drop across the threshold switch, when the frequency f_* of the local stimulus is set to a value 2 MHz (4 MHz) smaller (larger) than the frequency $f_{0,Z,\max}(Q) \equiv \omega_{0,Z,\max}(Q)/(2 \cdot \pi)$, amounting to 2.80 MHz, at which the real part $\Re\{Z(j\omega, Q)\}$ of the memristor local impedance $Z(j\omega, Q)$ about the operating point Q vanishes, and concurrently the phase $\angle Z(j\omega, Q)$ of the memristor local impedance $Z(j\omega, Q)$ at Q, expressed in degrees, attains the value of 90° (refer to Figure 7d). The phase difference between memristor local voltage δv_m and memristor local current δi_m, coinciding with the phase of the threshold switch local impedance at Q, expressed in degrees, is found to be equal to a value 99.10° (80.45) larger (smaller) than 90° by about 10° for $f_* = f_{*,1} = 2$ MHz ($f_* = f_{*,2} = 4$ MHz), as shown in plot (b,c), which matches the expectations from plot (d). As a result, as established by Equation (36), the net local energy $\delta\mathcal{E}(t_i, t_i + T_*; Q)$, with $t_i \geq t_0 = 1$ µs, absorbed by the memristor per input cycle is negative (positive) for the first (latter) input frequency scenario. With $f_* = 2$ MHz ($f_* = 4$ MHz),

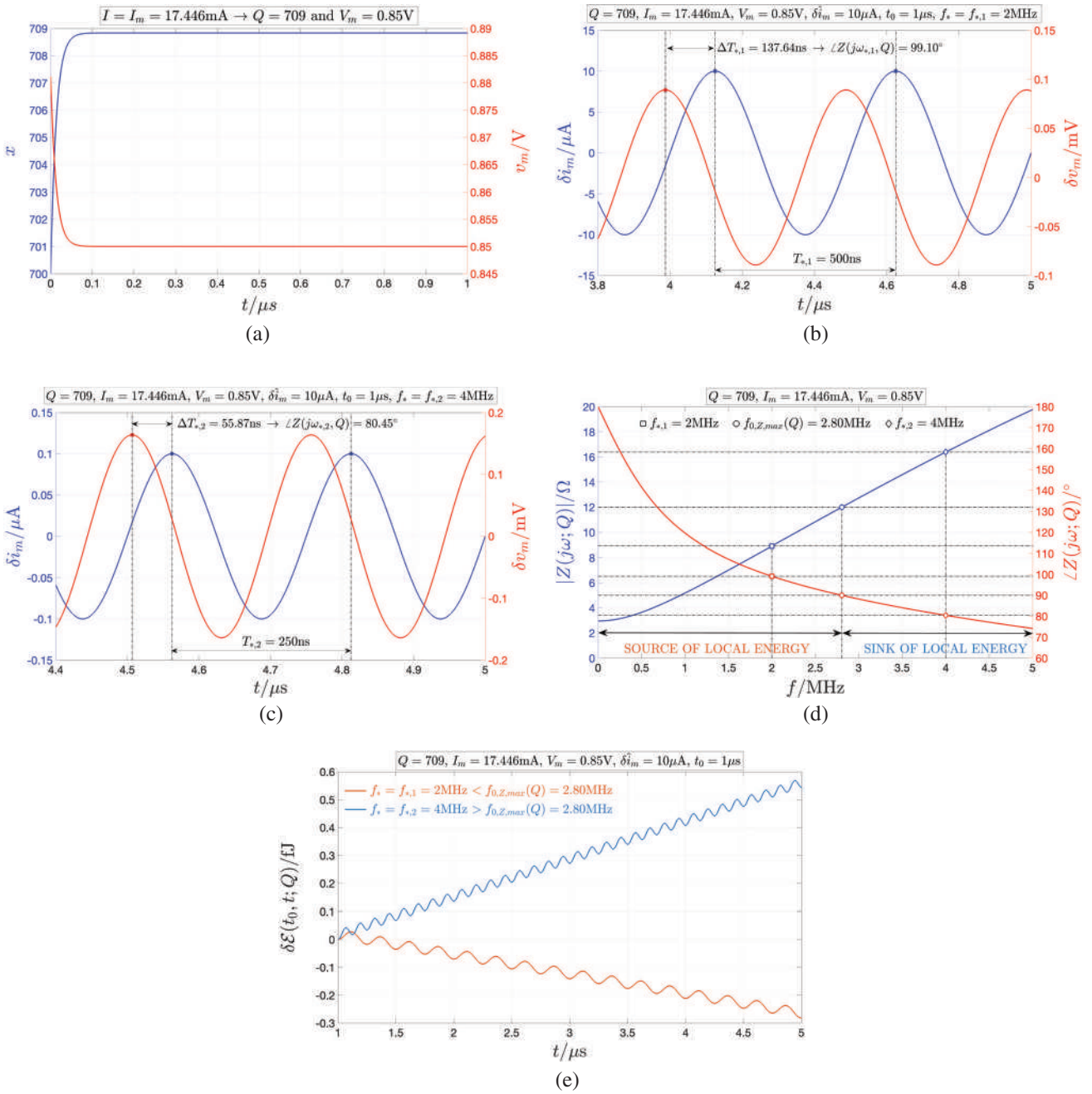

Figure 7. a) Blue (Red) trace: Progressive approach of the memristor state x (voltage v_m) toward the constant value $Q = X = 709$ ($V_m = 0.85$ V) in response to a DC current stimulus $I = 17.446$ mA let flow between its terminals using the circuit set-up from Figure 2a. b) Blue (Red) trace: time course of the memristor local current δi_m (memristor local voltage δv_m) from the instant $t_0 = 1$ µs at which a sine wave current δi of infinitesimal amplitude $\delta\hat{i} = 10$ µA, and phase $\angle\underline{i} = -\omega_* \cdot t_0$, with $\omega_* = 2 \cdot \pi \cdot f_*$ and $f_* = f_{*,1}$, set to 2 MHz, denote its angular frequency and frequency, respectively, is let flow between the threshold switch terminals together with the much larger DC current stimulus $I = 17.446$ mA. The local input current period $T_{*,1} = 1/f_{1,*}$ is equal to 500ns. The modulus of the temporal distance $\Delta T_{*,1}$ between a maximum of the voltage trace and an adjacent maximum of the current trace is found to be equal to 137.64ns, which results in a phase between the phase of the red trace and the phase of the blue trace, expressed in degrees, as large as $\angle\underline{\delta v_m} - \angle\underline{\delta i_m} = -\omega_{*,1} \cdot \Delta T_{*,1} \cdot 180°/\pi = 99.10°$. c) Blue (Red) trace: time course of the memristor local current δi_m (memristor local voltage δv_m) from the instant $t_0 = 1$ µs at which a sine wave current δi of infinitesimal amplitude $\hat{i} = 10$ µA, and phase $\angle\underline{i} = -\omega_* \cdot t_0$, with $\omega_* = 2 \cdot \pi \cdot f_*$ and $f_* = f_{*,2}$, set to 4 MHz, denote its angular frequency and frequency, respectively, is let flow between the threshold switch terminals together with the much larger DC current stimulus $I = 17.446$ mA. The local input current period $T_{*,2} = 1/f_{2,*}$ is equal to 250 ns. The modulus of the temporal distance $\Delta T_{*,2}$ between a maximum of the voltage trace and an adjacent maximum of the current trace is found to be equal to 55.87ns, which results in a difference between the phase of the red trace and the phase of the blue trace, expressed in degrees, as large as $\angle\underline{\delta v_m} - \angle\underline{\delta i_m} = -\omega_{*,2} \cdot \Delta T_{*,2} \cdot 180°/\pi = 80.45°$. d) Blue (Red) trace: Modulus $|Z(j\omega, Q)|$ (Phase $\angle\underline{Z(j\omega, Q)}$) of the memristor local impedance $Z(j\omega, Q)$ at $Q = 709$ against the frequency f. The blue (red)

the net local energy $\delta\mathcal{E}(t_0, t; Q)$ absorbed by the memristor from the instant t_0, at which the local current stimulus δi is let flow between its terminals, to any later time t is illustrated through a light brown (light blue) trace in Figure 7e. As expected, in the first (latter) case $\delta\mathcal{E}(t_0, t; Q)$ inevitably keeps decreasing (increasing) from input cycle to input cycle. Clearly, the NaMLab memristor acts as a source (sink) of local energy about the operating point Q for the lower (higher) input frequency case.

5. Large- and Small-Signal Models of the First and Simplest Ever Reported Hodgkin–Huxley Neuristor

The simplest bio-inspired locally-active circuit, able to undergo all the three fundamental bifurcations, which mark the life cycle of a neuronal electrical spike, is shown in Figure 2e.

It is a memristive variant of a well-know relaxation oscillator,[39] first introduced by Pearson and Anson (Refs. [40, 41]), being composed of the parallel combination between one linear capacitor C, one NaMLab threshold switch $\mathcal{M}$, and a bias circuit, including a DC voltage source V_{in} and its series resistance R_L. With reference to Figure 2 the Norton equivalent representation of the Thévenin circuit from plot (e) is illustrated in plot (f), where $I_{in} = V_{in}/R_L$. Clearly, the Norton cell has a similar topology as the Hodgkin–Huxley neuron circuit model from Figure 1a. However, rather remarkably, the proposed NaMLab neuristor leverages just two dynamical elements to reproduce the triplet of fundamental bifurcations, which, as predicted by Hodgkin and Huxley through the study of a biologically-plausible model—refer to the fourth-order nonlinear ODE set (1)-(4)[23] in the Suporting Information — featuring double the number of degrees of freedom, characterise the life cycle of an Action Potential under monotonic synaptic current modulation in biological neurons, as beautifully pictured by the bifurcation diagram of Figure 1c. Moreover, the proposed Hodgkin–Huxley neuristor may be further simplified by replacing the circuitry, polarizing the memristor $\mathcal{M}$ in a given NDR operating point Q of interest, specifically the parallel combination between a linear resistor R_L and a DC source, generating a constant current I_{in}, with a single generator of bias current I (refer to Section 8). Irrespective of its circuit topology, the Hodgkin–Huxley neuristor is indicated as $\mathcal{N}$ in the remainder of this paper.

The analysis to follow will focus on the current-driven oscillator of Figure 2f. Recurring to basic circuit-theoretic principles,[29] the second-order ODE, describing the Norton circuit, may be cast in the form

$$\dot{x} = f_{\mathcal{N},1}(x, v_m) \triangleq g(x, v_m), \text{ and} \tag{37}$$

$$\dot{v}_m = f_{\mathcal{N},2}(x, v_m) \triangleq \frac{1}{C} \cdot \left(I_{in} - \frac{v_m}{R_L} - i_m(x, v_m) \right) \tag{38}$$

where the two state variables, specifically x and v_m, respectively represent the memristor state and voltage, the latter coinciding with the capacitor voltage v_C, $g(x, v_m)$ is the state evolution function of the NbO_x threshold switch under voltage stimulation, as reported in Equation (11), while $i_m(x, v_m)$ stands for the respective current, as expressed via Ohm's law (10), with $G(x)$ denoting the memductance function from Equation (12). The state evolution function $f_{\mathcal{N},1}(x, v_m)$ ($f_{\mathcal{N},2}(x, v_m)$) provides the rate of change of the memristor state x (voltage v_m). Assuming to have preliminarily assigned a specific value to the resistance R_L, given a bias current stimulus $I_{in} = V_{in}/R_L$, an admissible operating point for the second-order relaxation oscillator is defined as $\mathbf{Q}_{\mathcal{N}} \triangleq (Q, V_m)$, where $Q = X$ and V_m indicate the DC values for memristor state x and voltage v_m, at which both $f_{\mathcal{N},1}(x, v_m)$ and $f_{\mathcal{N},2}(x, v_m)$ concurrently vanish. Now, the local model of the current-driven oscillator of Figure 2f may be derived, similarly as was done earlier for the memristor DAE set (9)–(10) under voltage excitation, by linearizing the second-order nonlinear ODE (37)–(38) about an operating point $\mathbf{Q}_{\mathcal{N}}$, assuming, furthermore, an infinitesimal current δi_{in} to enter its capacitor C through node A. The local model of the memristor oscillator takes the form

$$\delta\dot{x} = a_{\mathcal{N}}(\mathbf{Q}_{\mathcal{N}}) \cdot \delta x + b_{\mathcal{N}}(\mathbf{Q}_{\mathcal{N}}) \cdot \delta v_m, \text{ and} \tag{39}$$

$$\delta\dot{v}_m = c_{\mathcal{N}}(\mathbf{Q}_{\mathcal{N}}) \cdot \delta x + d_{\mathcal{N}}(\mathbf{Q}_{\mathcal{N}}) \cdot \delta v_m + \delta u_{in} \tag{40}$$

where δx and δv_m respectively denote the small-signal memristor state and voltage response to the infinitesimal current stimulus δi_{in}, $\delta u_{in} \triangleq \delta i_{in}/C$. By partial differentiation of the state evolution functions $f_1(x, v_m)$ and $f_2(x, v_m)$, the formulas for the local parameters of the neuristor depend upon its operating point $\mathbf{Q}_{\mathcal{N}}$ via

$$a_{\mathcal{N}}(\mathbf{Q}_{\mathcal{N}}) \triangleq \left.\frac{\partial f_{\mathcal{N},1}(x, v_m)}{\partial x}\right|_{\mathbf{Q}_{\mathcal{N}}=(Q,V_m)} = a(Q) \tag{41}$$

$$b_{\mathcal{N}}(\mathbf{Q}_{\mathcal{N}}) \triangleq \left.\frac{\partial f_{\mathcal{N},1}(x, v_m)}{\partial v_m}\right|_{\mathbf{Q}_{\mathcal{N}}=(Q,V_m)} = b(Q) \tag{42}$$

$$c_{\mathcal{N}}(\mathbf{Q}_{\mathcal{N}}) \triangleq \left.\frac{\partial f_{\mathcal{N},2}(x, v_m)}{\partial x}\right|_{\mathbf{Q}_{\mathcal{N}}=(Q,V_m)} = -\frac{c(Q)}{C}, \text{ and} \tag{43}$$

$$d_{\mathcal{N}}(\mathbf{Q}_{\mathcal{N}}) \triangleq \left.\frac{\partial f_{\mathcal{N},2}(x, v_m)}{\partial v_m}\right|_{\mathbf{Q}_{\mathcal{N}}=(Q,V_m)} = -\frac{d(Q) + G_L}{C} \tag{44}$$

in which $G_L = R_L^{-1}$, while $a(Q)$, $b(Q)$, $c(Q)$, and $d(Q)$ are expressed by Equations (19), (20), (21) and (22). After mapping the small-signal neuristor model (39)–(40) into the Laplace domain for $x_0 = x(0) = 0$ and $v_{m,0} = v_m(0) = 0$, and performing some algebraic calculation on the resulting linear system, the small-signal impedance $Z_{\mathcal{N}}(s; \mathbf{Q}_{\mathcal{N}})$ of the current-driven neuristor of Figure 2f

square, circle, and diamond markers indicate the modulus (the phase) of the memristor local impedance $Z(j\omega, Q)$ at $Q = 709$ when the frequency f is respectively equal to $f_{*,1} = 2$ MHz, $f_{0,Z,\max}(Q) = 2.80$ MHz, and $f_{*,2} = 4$ MHz. Letting a DC current $I = 17.446$ mA flow continuously between its terminals, the memristor is bound to operate as a source (sink) of local energy when, after having attained the expected operating point $Q = 709$, a purely-AC periodic sine wave current δi of infinitesimal amplitude $\delta\hat{i}$ and positive frequency f_* smaller (larger) than $f_{0,Z,\max}(Q) = 2.80$ MHz, implying $\angle Z(j\omega_*, Q)$ to be larger (smaller) than 90°, is injected together with the bias current I into its physical medium. e) Light brown (Light blue) trace: Locus of the net local energy $\delta\mathcal{E}(t_0, t; Q)$ absorbed by the memristor poised on $Q = 709$ from $t_0 = 1$ µs to any later time till $t = 5$ µs as the small-signal sine wave current δi of amplitude $\delta\hat{i} = 10$ µA and frequency $f_* = f_{*,1} = 2$ MHz ($f_* = f_{*,2} = 4$ MHz) from plot (b,c) flows between its terminals. In the first (latter) case the memristor behaves as a source (sink) of local energy, as expected from plot (d).

at the port A–B about an operating point $\mathbf{Q}_{\mathcal{N}}$ is found to read as

$$Z_{\mathcal{N}}(s;\mathbf{Q}_{\mathcal{N}}) \triangleq \left.\frac{\mathcal{L}\{\delta v_m(t)\}}{\mathcal{L}\{\delta i_{in}(t)\}}\right|_{\mathbf{Q}_{\mathcal{N}}}$$

$$= K_{Z_{\mathcal{N}}}(\mathbf{Q}_{\mathcal{N}}) \cdot \frac{s - z_{Z_{\mathcal{N}}}(\mathbf{Q}_{\mathcal{N}})}{\left(s - p_{-,Z_{\mathcal{N}}}(\mathbf{Q}_{\mathcal{N}})\right) \cdot \left(s - p_{+,Z_{\mathcal{N}}}(\mathbf{Q}_{\mathcal{N}})\right)} \tag{45}$$

where the factor $K_{Z_{\mathcal{N}}}$, scaling the rational function, the zero $z_{Z_{\mathcal{N}}}$, and the poles $p_{-,Z_{\mathcal{N}}}$ and $p_{+,Z_{\mathcal{N}}}$, when evaluated at $\mathbf{Q}_{\mathcal{N}}$, are respectively expressed by

$$K_{Z_{\mathcal{N}}}(\mathbf{Q}_{\mathcal{N}}) = \frac{1}{C} \tag{46}$$

$$z_{Z_{\mathcal{N}}}(\mathbf{Q}_{\mathcal{N}}) = p_Y(Q) = -\frac{r_2(Q)}{l(Q)}, \text{and} \tag{47}$$

$$p_{\mp,Z_{\mathcal{N}}}(\mathbf{Q}_{\mathcal{N}}) = \frac{\rho(\mathbf{Q}_{\mathcal{N}}) \mp \sqrt{\rho^2(\mathbf{Q}_{\mathcal{N}}) - 4 \cdot \eta(\mathbf{Q}_{\mathcal{N}})}}{2} \tag{48}$$

in which

$$\rho(\mathbf{Q}_{\mathcal{N}}) = -\frac{r_2(Q)}{l(Q)} - \frac{r_1(Q) + R_L}{C \cdot r_1(Q) \cdot R_L}, \text{ and} \tag{49}$$

$$\eta(\mathbf{Q}_{\mathcal{N}}) = \frac{1}{l(Q) \cdot C} \cdot \left(1 + \frac{r_2(Q) \cdot (r_1(Q) + R_L)}{r_1(Q) \cdot R_L}\right) \tag{50}$$

while the expressions for $r_1(Q)$, $r_2(Q)$, and $l(Q)$ are reported in Equations (27), (28), and (29), respectively. The linear one-port in plot (b) of Figure 5 features at the source port A–B the very same impedance, as reported in Equation (45). As a result, it defines the circuit-theoretic representation of the small-signal model of the Hodgkin–Huxley neuristor from Figure 2f about an operating point $\mathbf{Q}_{\mathcal{N}}$. It is worth observing that the small-signal equivalent circuit model of the neuristor in Norton form can be retrieved alternatively from the respective large-signal circuit topology from Figure 2f by turning off the independent DC source I_{in} and replacing the memristor with its small-signal equivalent circuit model from Figure 5a. The very same conclusions may be drawn from the analysis of the equivalent Thévenin circuit topology in Figure 2e across the respective port A–B. In particular, the local circuit model of this cell may be obtained from Figure 2e upon replacing the DC source V_{in} with the small-signal stimulus δv_{in} and the memristor with its small-signal equivalent circuit model from Figure 5a. One could then compute the local impedance of the resulting voltage-driven linear circuit at the capacitor port A–B. Alternatively, this circuit may be first cast in the form shown in plot (b) of Figure 5 upon defining $\delta i_{in} = \delta v_{in}/R_L$, as established by the Norton Theorem, which allows to follow the very same procedure outlined above to compute the local transfer function from Equation (45) thereafter.

5.1. Local Activity and Edge of Chaos in the Hodgkin–Huxley Neuristor

On the basis of the expressions for $\rho(\mathbf{Q}_{\mathcal{N}})$ and $\eta(\mathbf{Q}_{\mathcal{N}})$, reported in Equations (49) and (50), respectively, it is easy to prove that an admissible operating point $\mathbf{Q}_{\mathcal{N}}$ for the neuristor $\mathcal{N}$ is unstable if $\eta(\mathbf{Q}_{\mathcal{N}}) < 0$, i.e., when

$$r_2(Q) < 0, \text{ and } R_L < |r(Q)| \tag{51}$$

irrespective of the sign of $\rho(\mathbf{Q}_{\mathcal{N}})$, or if $\rho(\mathbf{Q}_{\mathcal{N}}) > 0$, i.e. when

$$r_2(Q) < 0,\ R_L > |r(Q)|, \text{ and } C > \hat{C}(Q) \tag{52}$$

where

$$\hat{C}(Q) \triangleq -\frac{l(Q)}{r_2(Q)} \cdot \frac{r_1(Q) + R_L}{r_1(Q) \cdot R_L} \tag{53}$$

in case $\eta(\mathbf{Q}_{\mathcal{N}}) > 0$.

Letting $s = j\omega$, the real part $\Re\{Z_{\mathcal{N}}(s;\mathbf{Q}_{\mathcal{N}})\}$ of the local impedance $Z_{\mathcal{N}}(s;\mathbf{Q}_{\mathcal{N}})$ of the memristor oscillator of Figure 2f across the port A-B about an operating point $\mathbf{Q}_{\mathcal{N}}$ may be computed via

$$\Re\{Z_{\mathcal{N}}(j\omega;\mathbf{Q}_{\mathcal{N}})\}$$

$$= K_{Z_{\mathcal{N}}}(\mathbf{Q}_{\mathcal{N}}) \cdot \frac{-\rho(\mathbf{Q}_{\mathcal{N}}) \cdot \omega^2 - z_{Z_{\mathcal{N}}}(\mathbf{Q}_{\mathcal{N}}) \cdot (\eta(\mathbf{Q}_{\mathcal{N}}) - \omega^2)}{\left(\rho(\mathbf{Q}_{\mathcal{N}}) \cdot \omega\right)^2 + \left(\eta(\mathbf{Q}_{\mathcal{N}}) - \omega^2\right)^2} \tag{54}$$

which goes negative across the range of frequencies

$$|\omega_{0,Z_{\mathcal{N}}}(\mathbf{Q}_{\mathcal{N}})| < \omega_{0,Z_{\mathcal{N}},\max}(\mathbf{Q}_{\mathcal{N}})$$

$$\triangleq \sqrt{-\frac{r_2(Q)}{l^2(Q)} \cdot \left(r_2(Q) + \frac{r_1(Q) \cdot R_L}{r_1(Q) + R_L}\right)} \tag{55}$$

provided the polarity of the radicand is positive, which calls for the need to fulfil concurrently the two inequalities $r_2(Q) < 0$ and $R_L > |r(Q)|$.

It follows that the proposed Hodgkin–Huxley neuristor from Figure 2f is poised on a GAS and locally-active operating point $\mathbf{Q}_{\mathcal{N}} = (Q, V_m)$ if the three inequalities

$$r_2(Q) < 0\ R_L > |r(Q)|, \text{ and } C < \hat{C}(Q) \tag{56}$$

are simultaneously satisfied. Last but not least, these conclusions on the Local Activity and Edge of Chaos of the proposed Hodgkin–Huxley neuristor $\mathcal{N}$ might have been equivalently derived by analyzing the Thévenin cell of Figure 2e.

5.2. Number, Local Stability, and Local Passivity/Local Activity Properties of the Operating Points of the Memristor Oscillator

On the basis of the results, acquired through the investigation of the DC response of the memristor $\mathcal{M}$ and through the exploration of the capability of the neuristor $\mathcal{N}$ from Figure 2f to amplify infinitesimal fluctuations in energy, as pursued in the Sections 4.2 and 5.1, respectively, the following conclusions may be drawn on number, local stability, and local activity properties of the admissible operating points for the equivalent Thévenin circuit topology in plot (a) of the same figure on the basis of the

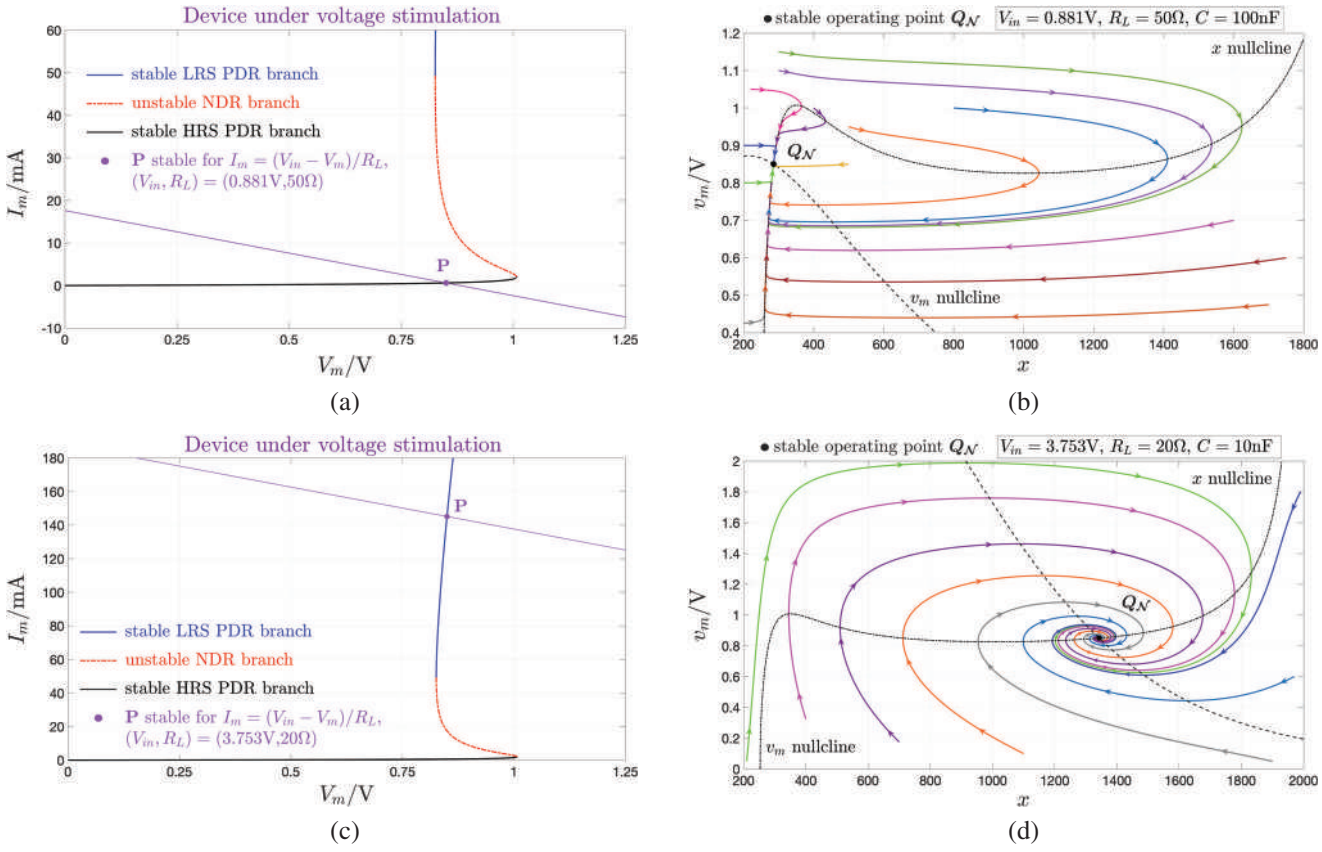

Figure 8. a) Application of the load line method to determine the memristor bias point **P** for $V_{in} = 0.881$ V and $R_L = 50\ \Omega$. The bias parameters stabilize **P** at $(V_m, I_m) = (0.85\text{ V}, 0.620\text{ mA})$, falling along the HRS PDR branch of the device DC current versus voltage characteristic. b) Phase portrait of the relaxation oscillator in Figure 2e under this bias parameter setting and for $C = 100$ nF. The second-order cell features one and only one locally-passive and stable operating point $\mathbf{Q}_\mathcal{N}$ at $(Q, V_m) = (285, 0.85\text{ V})$. c) Graphical identification of the memristor bias point **P** for $V_{in} = 3.753$ V and $R_L = 20\ \Omega$ via the load line method. In this scenario **P** is stabilized at $(V_m, I_m) = (0.85\text{ V}, 145\text{ mA})$, belonging to the LRS PDR branch of the device DC current versus voltage characteristic. d) Illustration of the local and global behavior of the second-order cell, featuring the aforementioned bias parameter values and a capacitance C of 10nF, for each initial condition from a wide set. The only locally-passive and stable operating point $\mathbf{Q}_\mathcal{N}$ for the oscillator of Figure 2e lies at $(Q, V_m) = (1342, 0.85\text{ V})$.

bias parameters V_{in} and R_L as well as of the capacitance C, assuming, without loss of generality, a positive polarity for the DC input voltage V_{in}.

1. If the bias parameter pair (V_{in}, R_L) is chosen in such a way that the load line of the circuit of Figure 2c crosses the DC current I_m versus voltage V_m locus just once, identifying a bias point $\mathbf{P} = (V_m, I_m)$, lying either along the HRS PDR branch or along the LRS PDR branch, as respectively illustrated in **Figure 8**a,c, which implies a positive polarity for $r_2(Q)$, where Q denotes the memristor operating point, corresponding to the bias point **P**, the oscillatory cell of Figure 2e is found to admit a locally-passive and locally-stable operating point $\mathbf{Q}_\mathcal{N} = (Q, V_m)$, irrespective of the value assigned to the capacitance C.
2. If the bias parameter pair (V_{in}, R_L) is chosen in such a way that the load line of the circuit of Figure 2c crosses the DC I_m versus V_m locus three times, identifying one bias point $\mathbf{P}_1 = (V_{m,1}, I_{m,1})$ in the HRS PDR branch, one bias point $\mathbf{P}_2 = (V_{m,2}, I_{m,2})$ in the NDR branch, and one bias point $\mathbf{P}_3 = (V_{m,3}, I_{m,3})$ in the LRS PDR branch, as depicted in **Figure 9**a, which implies $r_2(Q_1) > 0$, $r_2(Q_2) < 0$, $R_S < |r(Q_2)|$, and $r_2(Q_3) > 0$, where Q_i denotes the i^{th} memristor operating point, corresponding to its i^{th} bias point $\mathbf{P}_\mathbf{i}$ $(i \in (1, 2, 3))$, the oscillator of Figure 2e is found to admit a triplet of operating points, specifically $\mathbf{Q}_{\mathcal{N},1} = (Q_1, V_{m,1})$, $\mathbf{Q}_{\mathcal{N},2} = (Q_2, V_{m,2})$, and $\mathbf{Q}_{\mathcal{N},3} = (Q_3, V_{m,3})$, the first and third (the second) of which being locally-passive and locally-stable (locally-active yet unstable), irrespective of the capacitance C.
3. If the bias parameter pair (V_S, R_S) is chosen in such a way that the load line of the circuit of Figure 2c crosses the DC I_m versus V_m locus three times, identifying one bias point $\mathbf{P}_1 = (V_{m,1}, I_{m,1})$ on the HRS PDR branch, and two bias points, namely $\mathbf{P}_2 = (V_{m,2}, I_{m,2})$ and $\mathbf{P}_3 = (V_{m,3}, I_{m,3})$ on the NDR branch, as visualized in **Figure 10**a, which implies $r_2(Q_1) > 0$, $r_2(Q_2) < 0$, $r_2(Q_3) < 0$, and $|r(Q_3)| < R_S < |r(Q_2)|$, where Q_i denotes the i^{th} memristor operating point, corresponding to its i^{th} bias point $\mathbf{P}_\mathbf{i}$ $(i \in (1, 2, 3))$, the oscillator of Figure 2e is found to admit a triplet of operating points, specifically $\mathbf{Q}_{\mathcal{N},1} = (Q_1, V_{m,1})$, $\mathbf{Q}_{\mathcal{N},2} = (Q_2, V_{m,2})$, and $\mathbf{Q}_{\mathcal{N},3} = (Q_3, V_{m,3})$. While the first (second) cell operating point is locally-passive and locally-stable (locally-active yet unstable), irrespective of

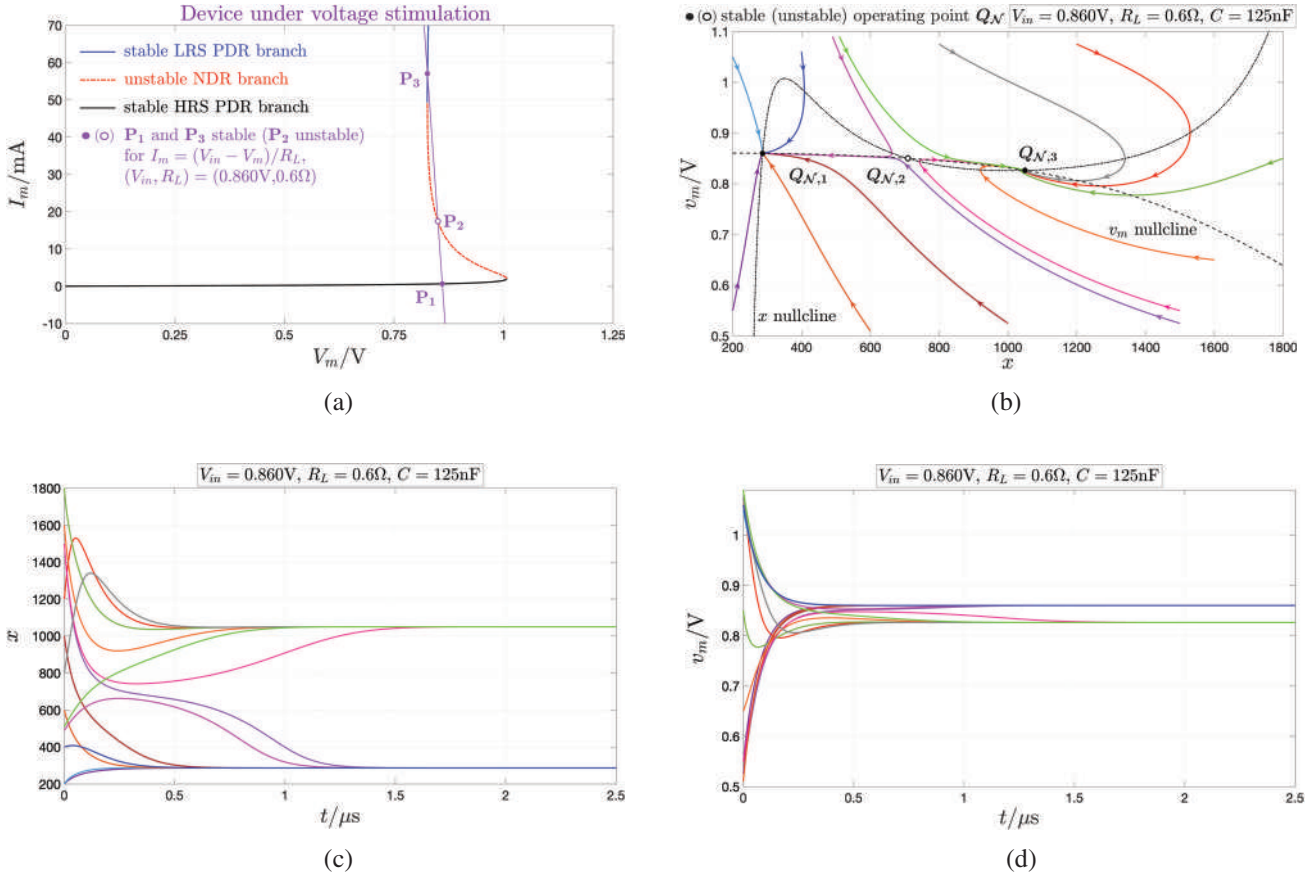

Figure 9. a) Intersections between memristor DC I_m versus V_m characteristic and load line for V_{in} = 0.8605 V and R_L = 0.6 Ω. The device admits a triplet of bias points, of which $\mathbf{P_1} = (V_{m,1}, I_{m,1})$ = (0.8601 V, 0.644 mA), lying along the HRS PDR branch, and $\mathbf{P_3} = (V_{m,3}, I_{m,3})$ = (0.8262 V, 57.045 mA), falling on the LRS PDR region, are locally stable, whereas $\mathbf{P_2} = (V_{m,2}, I_{m,2})$ = (0.85 V, 17.446 mA), belonging to the NDR domain, is unstable. b) Progressive approach of the relaxation oscillator of Figure 2e toward either of two locally passive and locally stable operating points, i.e., $\mathbf{Q}_{\mathcal{N},1} = (Q_1, V_{m,1})$ = (287, 0.8601 V) or $\mathbf{Q}_{\mathcal{N},3} = (Q_3, V_{m,3})$ = (1050, 0.8262 V), depending upon the initial condition, for C = 125 nF. The stable manifold of the locally-active yet unstable operating point $\mathbf{Q}_{\mathcal{N},2} = (Q_2, V_{m,2})$ = (709, 0.85 V) separates the basins of attraction of $\mathbf{Q}_{\mathcal{N},1}$ and $\mathbf{Q}_{\mathcal{N},3}$. c,d) Progression of the memristor voltage v_m (memristor state x) toward one of the two admissible asymptotic values, specifically $V_{m,1}$ = 0.8601 V (Q_1 = 287) or $V_{m,3}$ = 0.8262 V (Q_3 = 1050), for each of the initial conditions considered to draw the phase portrait in (b).

the capacitance, the third-one, keeping locally active at all circumstances, is found to be a stable (an unstable) focus whenever the value assigned to the capacitance C is smaller (larger) than a critical threshold $\hat{C}(Q_3)$ determinable via Equation (53).

4. If the bias parameter pair (V_{in}, R_L) is chosen in such a way that the load line of the circuit of Figure 2c crosses the DC current versus voltage locus just once, identifying a bias point $\mathbf{P} = (V_m, I_m)$, lying along the NDR branch, as shown in Figures 4c and 11a, which implies $r_2(Q) < 0$ and $R_S > |r(Q)|$, where Q denotes the only admissible memristor operating point, corresponding to its unique bias point $\mathbf{P}$, the oscillatory cell of Figure 2e is found to admit a locally-active operating point $\mathbf{Q}_{\mathcal{N}} = (Q, V_m)$, which is endowed with stability (instability) if the capacitance C is smaller (larger) than a bifurcation threshold $\hat{C}(Q)$ computable through Equation (53).

As will be unveiled shortly, it is in case study 4, and, particularly, while exiting, or entering, or operating on the Edge of Chaos domain, that the second-order relaxation oscillator from Figure 2(e) may reproduce the complex emergent phenomena, appearing in the fourth-order Hodgkin–Huxley neuron model, as illustrated in the classical bifurcation diagram from Figure 1c.

5.2.1. Condition for the Occurrence of a Local Hopf Bifurcation Across the Bio-Inspired Oscillator

A Local Hopf Bifurcation[6] may occur across the Thévenin (Norton) cell, shown in plot (e,f) of Figure 2, only in case study 4 from Section 5.2, and when, moreover, the cell is poised on an operating point $\mathbf{Q}_{\mathcal{N}} = (Q, V_m)$ at the frontier between its instability and Edge of Chaos domains, i.e., provided the following three constraints concurrently apply:

$$r_2(Q) < 0, \quad R_L > |r(Q)|, \quad \text{and} \quad C = \hat{C}(Q) \tag{57}$$

where the closed-form expression for $\hat{C}(Q)$ is reported in Equation (53).

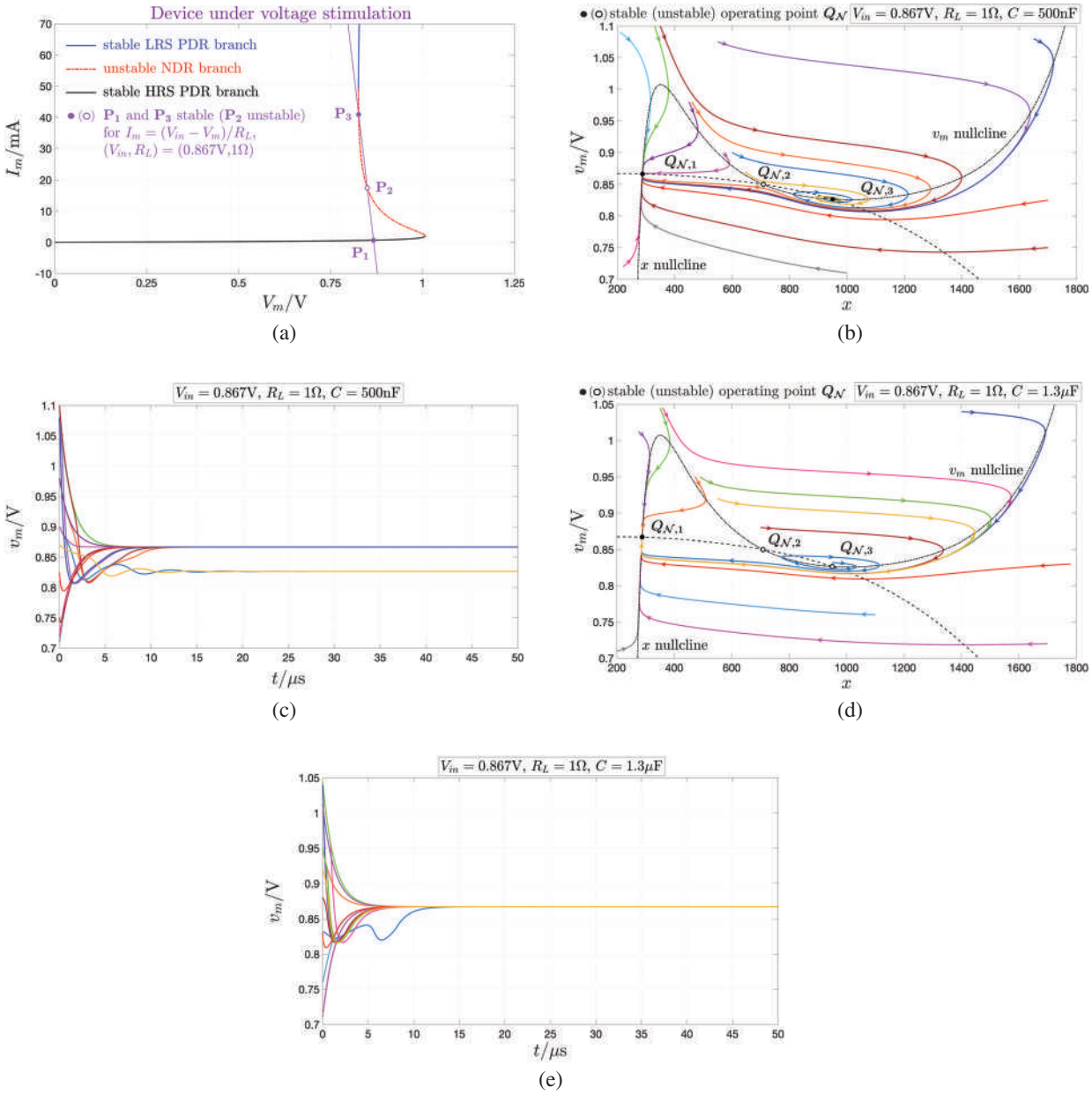

Figure 10. a) Crossings between DC I_m versus V_m locus and load line for V_{in} = 0.8674 V and R_L = 1 Ω. Three are the admissible bias points for the memristor. While $\mathbf{P_1} = (V_{m,1}, I_{m,1})$ = (0.8668 V, 0.661 mA) falls on the HRS PDR branch, both $\mathbf{P_2} = (V_{m,2}, I_{m,2})$ = (0.85 V, 17.446 mA) and $\mathbf{P_3} = (V_{m,3}, I_{m,3})$ = (0.8265 V, 40.945 mA) belong to the NDR region. As a result of the bias parameter setting, $\mathbf{P_1}$ and $\mathbf{P_3}$ are stable, while $\mathbf{P_2}$ is unstable. b,d)) Phase portrait of the oscillator of Figure 2e for C = 500 nF (C = 1.3 μF). The cell operating point $\mathbf{Q}_{\mathcal{N},1} = (Q_1, V_{m,1})$ = (288, 0.8668 V) ($\mathbf{Q}_{\mathcal{N},2} = (Q_2, V_{m,2})$ = (709, 0.85 V)) keeps locally-passive and stable (locally-active yet unstable), irrespective of the capacitance value. On the other hand, while maintaining its local activity, $\mathbf{Q}_{\mathcal{N},3} = (Q_3, V_{m,3})$ = (950, 0.8265 V) loses stability as C is increased above a threshold value of $\hat{C}(Q_3)$ = 1.273 μF. This notwithstanding, the cell does not undergo sustained limit-cycle oscillations for larger capacitance values. In fact, it is found to exhibit a bistable (monostable) quiescent steady state, depending (independent) upon (of) the initial conditions for any $C < (>)\hat{C}(Q_3)$, as is the case for example in the scenario illustrated in plot (b,c). c,e) Time behavior of the memristor voltage v_m from each initial condition used to draw the pre-bifurcation (post-bifurcation) phase portrait for C = 500 nF (C = 1.3 μF) in plot (b,d).

5.3. Unfolding the Global Nonlinear Dynamics of the Oscillator

The application of concepts from Local Activity Theory[2] allows to explore the dynamics of the Thévenin (Norton) topology of the oscillator, as shown in plot (e,f) of Figure 2, in the neighborhood of each of its admissible operating points, as described in Section 5.2. However, *important aspects of the dynamics of a nonlinear system may be overlooked when linearization techniques are applied to its model before commencing its analysis*. For this reason, drawing a comprehensive picture for the response of the oscillator to DC stimulation may not leave aside the investigation of its global behavior, which calls for the application of powerful

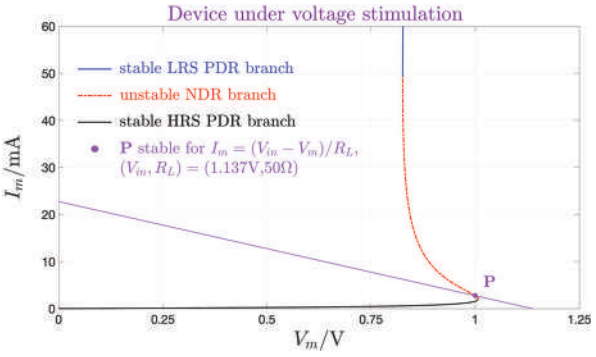

(a)

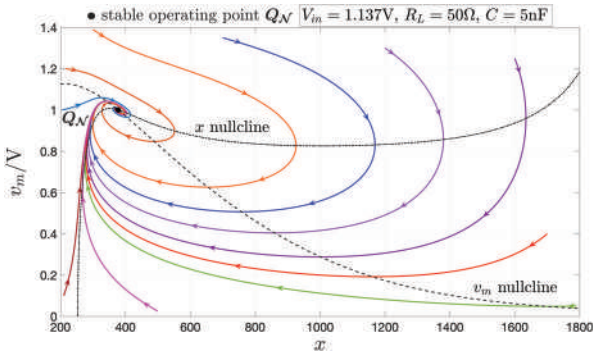

(b)

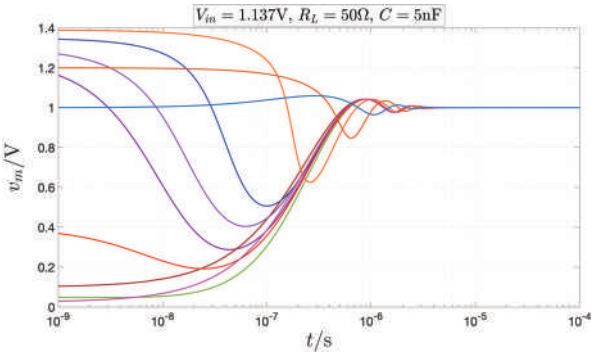

(c)

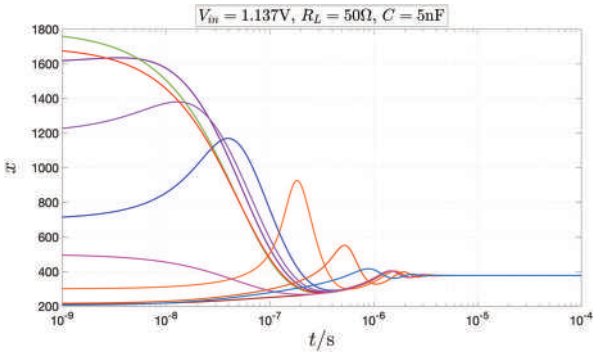

(d)

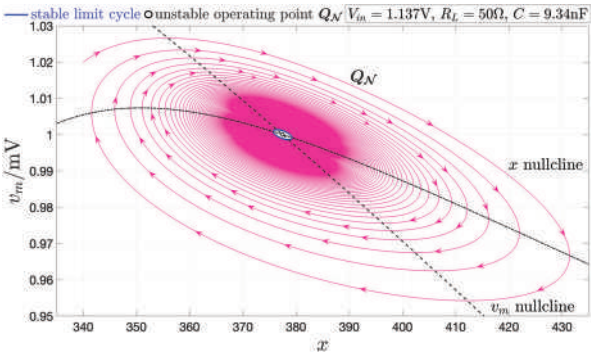

(e)

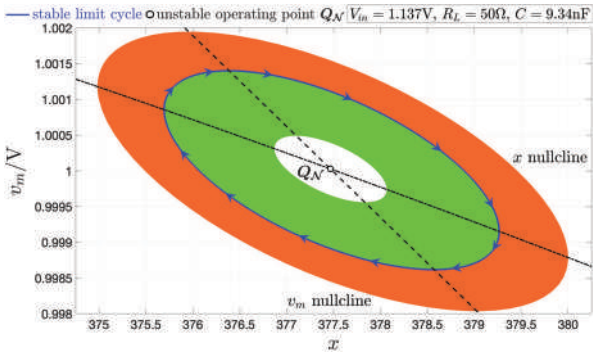

(f)

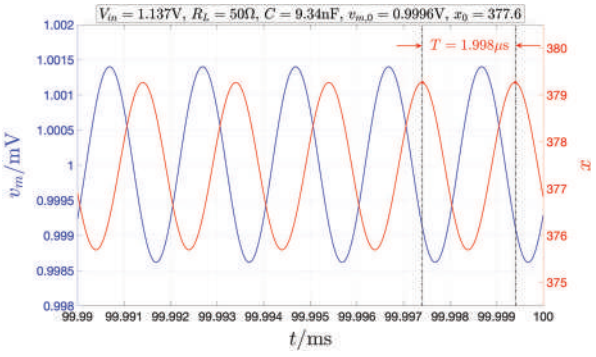

(g)

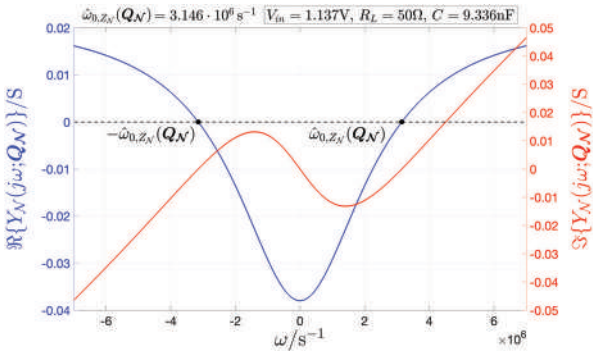

(h)

techniques from Nonlinear Dynamics Theory.[4] One of the most important investigation methods, allowing to shed light into the behavior of the proposed second-order oscillator of Figure 2e far away from its operating points, calls for the analysis of its *phase portrait*, a graph drawn on the 2D v_m versus x space, referred to as *phase plane*, and spanned by the two dynamical states of the ODE set (37)–(38), where $I_{in} = V_{in}/R_L$. Given a certain parameter setting for the oscillator, x and v_m evolve over time from a certain initial condition $(x_0, v_{m,0}) \triangleq (x(0), v_m(0))$ under the effect of the *vector field*, whose first (second) component denotes the rate of change $\dot{x} = f_1(x, v_m)$ ($\dot{v}_m = f_2(x, v_m)$) of the memristor state (voltage) according to the ODE (37) (38). Projecting the solutions $x(t)$ and $v_m(t)$ to the ODE system one against the other from the initial time of their evolution, each point on the resulting trace, referred to as *phase-plane trajectory*, moves with a speed (in the direction) imposed by the modulus $r(\dot{x}, \dot{v}_m)$ (phase $\varphi(\dot{x}, \dot{v}_m)$) of the vector field, computable via $r(\dot{x}, \dot{v}_m) = \sqrt{\dot{x}^2 + \dot{v}_m^2}$ ($\varphi(\dot{x}, \dot{v}_m) = \arctan(\dot{v}_m/\dot{x}) + \pi/2 \cdot (1 - \text{sign}(\dot{x}))$). The phase portrait of the oscillator, preliminarily programmed through a specific parameter setting, consists of a number of trajectories, endowed with arrows, indicating how their points evolve with time from the respective initial conditions, and is further enriched with the system's attractors, which for the neuristor cell under study may either be operating points or limit cycles. The operating points lie at the intersections between the x and v_m nullclines. The first (latter) nullcline, depicted via a dash-dotted (dashed) black trace in the oscillator phase portraits to be discussed shortly, is the locus of phase-plane points, where the rate $\dot{x}$ ($\dot{v}_m$) of change of the memristor state x (memristor voltage v_m) vanishes. For the relaxation oscillator of Figure 2e, the x and v_m nullclines are respectively expressed by

$$v_m = \pm\sqrt{\frac{-a_0 - a_1 \cdot x}{b_2 + c_{2,1} \cdot x + c_{2,2} \cdot x^2 + c_{2,3} \cdot x^3 + c_{2,4} \cdot x^4 + c_{2,5} \cdot x^5}}, \text{ and } (58)$$

$$v_m = \frac{R_L}{1 + R_L \cdot G(x)} \cdot I_{in} \quad (59)$$

where $I_{in} = V_{in}/R_L$. The positive (negative) solution in Equation (58) should be employed to define the x nullcline in case V_{in} were endowed with a positive (negative) polarity. In the oscillator phase portraits, illustrated in this manuscript, a filled (hollow) circle is used to indicate a stable (an unstable) operating point $\mathbf{Q}_{\mathcal{N}}$, whereas an isolated closed orbit, drawn in solid blue (dash-dotted red) line style, is employed to denote a stable (an unstable) limit-cycle attractor. A blue-red dashed line style is further used here to indicate a semistable isolated closed orbit, particularly a saddle-node limit cycle, which attracts (repels) phase-plane trajectories initiated outside (inside) it. Through an extensive numerical investigation, based upon the phase portrait analysis method, we gained a deep understanding of the global behavior of the bio-inspired circuit of Figure 2e in each of the four case studies listed in Section 5.2. The results of the study are enumerated below.

1. With reference to the first (second) scenario from case study 1, as revealed in the exemplary phase portrait from Figure 8b,d, where an arbitrary value was assigned to the capacitance C, stabilizing the memristor along the HRS (LRS) PDR branch, as depicted in plot (a) of the same figure, the only operating point $\mathbf{Q}_{\mathcal{N}}$, which the oscillator consequently admits, is found to be not just locally but also globally asymptotically stable, attracting phase-plane trajectories irrespective of their initial conditions.
2. Focusing now on case study 2, as shown in the illustrative phase portrait from Figure 9b, where, once again, the capacitance C was chosen arbitrarily, when the bias parameters endow the memristor with two possible stable DC states, one per PDR branch, as visualized in plot (a) of the same figure, the oscillator phase plane may be partitioned into two regions, separated by the stable manifold of the saddle operating point $\mathbf{Q}_{\mathcal{N},2}$, the left (right) of which includes all the initial conditions, from which the oscillator itself asymptotically converges toward the locally-stable operating point $\mathbf{Q}_{\mathcal{N},1}$ ($\mathbf{Q}_{\mathcal{N},3}$). Here the cell exhibits an interesting bistable quiescent response to the DC stimulus,[42] as illustrated in terms of the memristor voltage v_m and of the memristor state x in plots (c) and (d) of

Figure 11. a) Illustration, which, similarly as the one depicted in Figure 4c, reveals how a suitable choice for the bias parameters, corresponding here to the assignment of 1.137V to V_{in} and of 50 Ω to R_L, allows the load line to cross the DC I_m versus V_m characteristic in a single point, lying on its NDR branch, only. Here the memristor bias point **P** is stabilized at $(V_m, I_m) = (1.000\text{ V}, 2.739\text{ mA})$. b) Progressive convergence of the state vector $[x, v_m]^T$ of the ODE system (37)–(38), where $I_{in} = V_{in}/R_L = 22.740$ mA, toward a unique locally-active and stable operating point $\mathbf{Q}_{\mathcal{N}}$, marked via a black filled circle, and lying at a phase-plane location, independent of the capacitance, of abscissa $Q = 377$ and ordinate $V_m = 1.000$ V, from each initial condition across a wide set for $C = 5$ nF. c,d) Asymptotic approach of memristor voltage v_m (state x) toward the steady-state value $V_m = 1.000$ V ($Q = 377$) from each initial condition considered to draw the phase portrait in (b). Increasing the capacitance up to the critical value $\hat{C}(Q = 377) = 9.336$ nF, the Thévenin cell of Figure 2e, or, equivalently, the Norton cell of Figure 2(f), where $I_{in} = V_{in}/R_L$, experiences a Hopf supercritical bifurcation, which destabilizes its locally-active operating point $\mathbf{Q}_{\mathcal{N}}$, and concurrently spawns a stable infinitesimally-small limit cycle around it on the v_m versus x plane. e) Progressive evolution of a phase-plane trajectory, initiated relatively far away from the location of the operating point, marked now through a hollow black circle to indicate its unstable nature, toward the just-born infinitesimally-small GAS limit-cycle attractor, appearing as an isolated closed blue orbit, for $C = 9.34$ nF. f) Green (Orange) trace: phase-plane trajectory, initiated locally inside (outside) the infinitesimally-small limit cycle, and approaching it asymptotically, for $C = 9.34$ nF. g) Blue (Red) trace: tiny almost-sinusoidal time waveform of memristor voltage v_m (memristor state x), recorded after transients vanished for $C = 9.34$ nF during the numerical simulation which produced the green solution trajectory in (f) for $(x_0, v_{m,0}) = (377.6, 0.9996\text{ V})$. h) Blue (Red) trace: locus of the real part $\Re\{Y_{\mathcal{N}}(j\omega; \mathbf{Q}_{\mathcal{N}})\}$ (imaginary part $\Im\{Y_{\mathcal{N}}(j\omega; \mathbf{Q}_{\mathcal{N}})\}$) of the local admittance $Y_{\mathcal{N}}(s)$ of either of the two equivalent bio-inspired cells across the respective port A-B about the operating point $\mathbf{Q}_{\mathcal{N}}$ for $s = j\omega$ versus the angular frequency ω for $C = \hat{C}(Q = 377) = 9.336$ nF. Importantly, $Y_{\mathcal{N}}(j\omega; \mathbf{Q}_{\mathcal{N}})$ vanishes at $\omega = |\hat{\omega}_{0,Z_{\mathcal{N}}}(\mathbf{Q}_{\mathcal{N}})| = 3.146 \cdot 10^6 \text{s}^{-1}$, given that here the poles of the local impedance $Z_{\mathcal{N}}(s)$ of either of the two equivalent second-order circuits at the respective port A–B about the operating point $\mathbf{Q}_{\mathcal{N}}$ form a complex conjugate pair reading as $p_{\mp,Z_{\mathcal{N}}}(\mathbf{Q}_{\mathcal{N}}) = \mp j\hat{\omega}_{0,Z_{\mathcal{N}}}(\mathbf{Q}_{\mathcal{N}})$ (refer to Figure 12d). The period of the tiny sine-wave-alike oscillation, along which the memristor state is expected to evolve at steady state at the Hopf supercritical bifurcation point $C = \hat{C}(Q) = 9.336$ nF in the voltage-driven (current-driven) electrical system of Figure 2e,f) for $V_{in} = 1.137$ V (for $I_{in} = V_{in}/R_L = 22.740$ mA) may be estimated via As expected, this is rather close to the temporal duration $T = 1.998$ μs of one cycle in the steady-state oscillatory waveform of the memristor state x from plot (g), obtained for a capacitance value, specifically 9.34 nF, just over the bifurcation threshold.

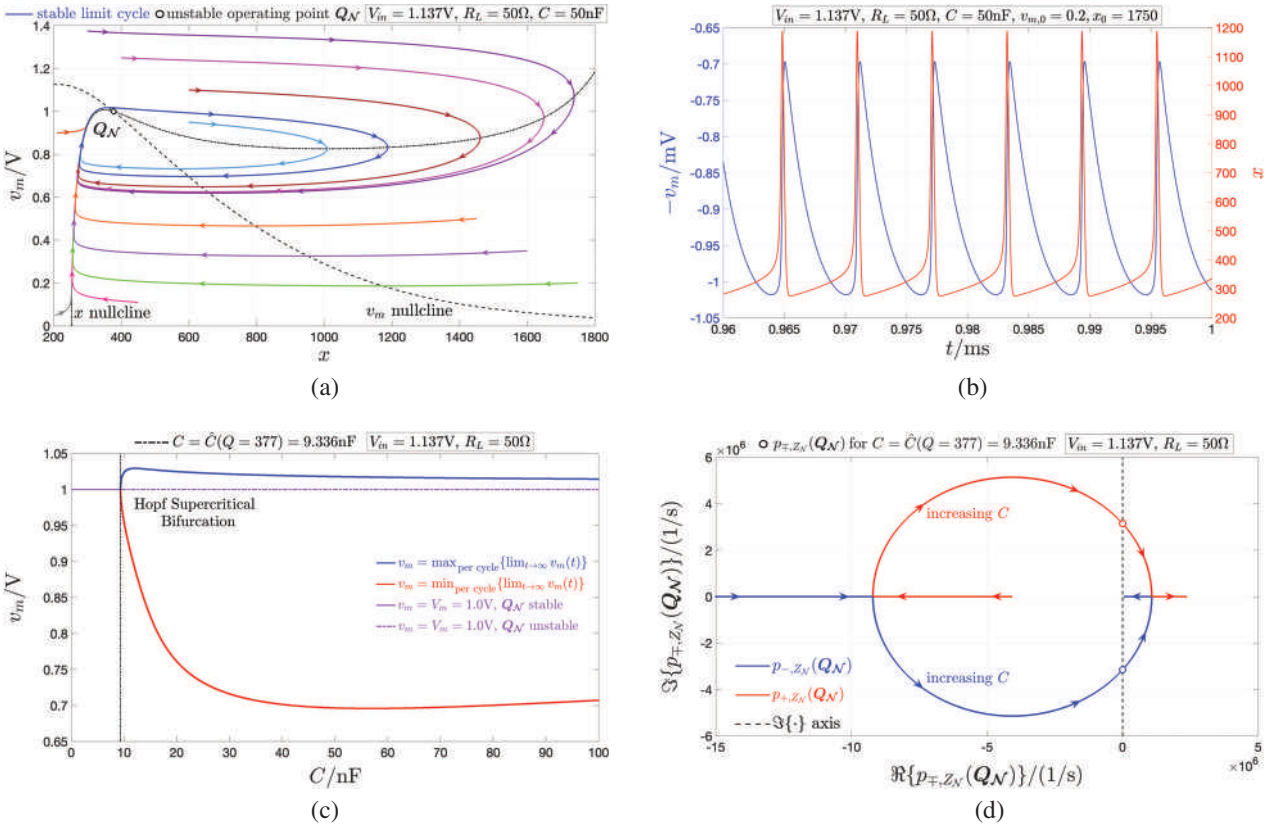

Figure 12. a) Phase portrait of the voltage-driven (current-driven) bio-mimetic oscillator in plot (e,f) from Figure 2 for $V_{in} = 1.137$ V and $R_L = 50\ \Omega$ (for $I_{in} = V_{in}/R_L = 22.740$ mA) with $C = 50$ nF. The size of the isolated closed blue orbit, representing the GAS limit-cycle attractor, has increased considerably since the occurrence of the Hopf supercritical bifurcation. b) Blue (Red) trace: time waveform of the sign-reversed voltage $-v_m$ (of the state x) of the memristor at steady state as extracted from the model simulation which generated the green phase-plane trajectory in (a) for $(x_0, v_{m,0}) = (1750, 0.2$ V). The first (latter) signal undergoes oscillatory dynamics qualitatively similar to the periodic behavior of the activation gating variable n of the potassium ion channel (of the membrane capacitance voltage v_m) in the Hodgkin–Huxley neuron model, as follows by direct comparison with the blue (red) trace from Figure 1d. c) Bifurcation diagram of either of the two equivalent oscillators on the v_m versus C plane for the aforementioned bias parameter pair upon sweeping the capacitance C from 0 to 100 nF. The ordinate of the oscillator operating point $\mathbf{Q}_{\mathcal{N}} = (Q, V_m) = (377, 1.000$ V) is indicated by the violet line. A solid (dash-dotted) line style is used to draw this line over the capacitance range to the left (right) of the Hopf supercritical bifurcation threshold $\hat{C}(Q = 377) = 9.336$ nF, where the oscillator operating point $\mathbf{Q}_{\mathcal{N}}$ is stable (unstable). For any $C > \hat{C}(Q = 377) = 9.336$ nF, a point on the blue (red) trace denotes the maximum (minimum) value $\max_{\text{per cycle}}\{\lim_{t\to\infty} v_m(t)\}$ ($\min_{\text{per cycle}}\{\lim_{t\to\infty} v_m(t)\}$), which the oscillatory waveform of the capacitor voltage v_m attains over each cycle at steady state, irrespective of the initial condition. d) Evolution of the poles $p_{-,Z_{\mathcal{N}}}(\mathbf{Q}_{\mathcal{N}})$ and $p_{+,Z_{\mathcal{N}}}(\mathbf{Q}_{\mathcal{N}})$ of the local impedance $Z_{\mathcal{N}}$ of the voltage-driven (current-driven) oscillator in plot (e,f) of Figure 2 at the respective port A–B about $\mathbf{Q}_{\mathcal{N}}$ for $R_L = 50\ \Omega$ and $V_{in} = 1.137$ V ($I_{in} = 22.740$ mA) across the complex plane upon sweeping the capacitance C from 0.9507 nF to 1 μF. As may be inferred from the locations of the hollow circle markers, the two poles form a purely-imaginary complex conjugate pair at the Hopf supercritical bifurcation point $C = \hat{C}(Q = 377) = 9.336$ nF.

Figure 9, respectively, yet it is still unable to support sustained limit-cycle oscillations.

3. Looking now at case study 3, as may be evinced from the exemplary phase portrait from Figure 10b,d, when the load line crosses twice the DC I_m versus V_m locus on its NDR branch, as shown in plot (a) of the same figure, the cell exhibits a bistable (monostable) quiescent condition, sitting either at $\mathbf{Q}_{\mathrm{N},1}$ or at $\mathbf{Q}_{\mathrm{N},3}$ (at $\mathbf{Q}_{\mathrm{N},1}$) at steady state, while $\mathbf{Q}_{\mathrm{N},2}$ keeps its saddle nature at all times, if the value assigned to the capacitance C is lower (larger) than the critical threshold $\hat{C}(Q_3)$. With reference to the same figure, plot (c,e) shows the time evolution of the memristor voltage v_m from each initial condition in the pre-bifurcation (post-bifurcation) phase portrait from plot (b,d). Despite the capacitance-induced change in the stability properties of one of its three admissible operating points, the bio-inspired circuit of Figure 2e was once again never found to settle on an oscillatory operating mode, as in the two case studies reported so far.
4. As anticipated earlier, a special consideration has to be given to case study 4, since, under a bias parameter setting, satisfying the associated constraints, the bio-inspired circuit from Figure 2e is capable to support the complex bifurcation phenomena, emerging in the Hodgkin–Huxley neuron model, when suitable conditions, to be disclosed shortly, are satisfied. Here it is worth monitoring the dynamical behavior of the bio-inspired cell across the capacitance C versus memristor operating point Q plane in the hypothesis, considered in the remainder of this manuscript, where the linear resistance R_L complies with the constraint $R_L > \max_{Q\in(Q_{NDR,L}, Q_{NDR,U})}|r(Q)| = |r(Q = 411)| = 21.427\ \Omega$. On the basis of the results from

Section 5.2, **Figure 13a** illustrates how such plane may be partitioned into distinct operating domains for the oscillator in the exemplary scenario where R_L is a 50 Ω resistance.

Remark 6. Since the inequality $R_L > |r(Q)|$ holds true, with the memristor bias point **P** belonging to a NDR branch of the DC I_m versus V_m locus, there exists a threshold value for the capacitance C, specifically $\hat{C}(Q)$, depending upon Q according to Equation (53), below (above) which the cell is poised on the Edge of Chaos (in the Unstable Local Activity) domain about $\mathbf{Q}_{\mathcal{N}} = (Q, V_m)$. Extensive numerical simulations, based upon the phase portrait analysis method, have revealed how, choosing the capacitance C as tuning parameter, the oscillator of Figure 2e may follow either of two possible bifurcation routes depending upon its operating point $\mathbf{Q}_{\mathcal{N}}$, i.e., equivalently, on the basis of the specific location of the memristor bias point **P** on the NDR branch of the DC I_m versus V_m locus. Along the first (second) bifurcation route, when the capacitance attains the critical value $\hat{C}(Q)$, the cell is found to undergo a local Hopf bifurcation of supercritical (subcritical) nature.

6. Unveiling the Complex Bifurcation Patterns of the Second-Order Bio-Inspired Memristive Oscillator

This section is devoted to unveil all the possible bifurcation phenomena, which may ever appear across the proposed bio-inspired oscillator under a monotonic sweep in one of its key design parameters, particularly the capacitance and its stimulus, as described in the first and section subsections to follow.

6.1. Bifurcation Routes of the Bio-Inspired Oscillator under Monotonic Capacitance Sweep

Let us first analyse the one-parameter bifurcation scenarios observable across the bio-ispired oscillator under capacitance sweep. Moving vertically across the C versus Q plane of Figure 13a, the local and global dynamical behavior of the cell may manifest two possible patterns, as described below.

4.a In the first one-parameter bifurcation scenario, occurring in case study 4, while increasing the value assigned to the capacitance C from 0, the Thévenin cell of Figure 2e, or, equivalently, the Norton cell of Figure 2f, where $I_{in} = V_{in}/R_L$, is found to sit on a locally active and GAS operating point $\mathbf{Q}_{\mathcal{N}}$ at steady state as long as C keeps below $\hat{C}(Q)$. When the control parameter attains this critical value, the cell undergoes a local Hopf supercritical bifurcation, which destabilizes the operating point, while spawning an infinitesimally-small limit cycle, encircling $\mathbf{Q}_{\mathcal{N}}$ and attracting any trajectory in the phase-plane. For any capacitance value beyond the bifurcation threshold $\hat{C}(Q)$ the cell keeps acting as an oscillator, irrespective of the initial condition.
As an illustrative example, setting V_{in} and R_L to 1.137 V and 50 Ω, respectively, as illustrated in Figure 11a, the memristor from the circuit of Figure 2c is stabilized on the bias point $\mathbf{P} = (V_m, I_m) = (1.000\text{ V}, 2.739\text{ mA})$, and endowed as a result with the operating point $Q = 377$. As may be inferred from the location of the black hollow circle marker in Figure 13a, the particular choice for the bias parameters sets the Hopf supercritical bifurcation capacitance $\hat{C}(Q = 377)$ to the value of 9.336 nF. As a result, increasing the capacitance from 0 along the vertical red solid line in the C versus Q diagram, as indicated by the arrows superimposed upon it, all the solution trajectories in the phase plane asymptotically approach $\mathbf{Q}_{\mathcal{N}} = (Q, V_m) = (377, 1.000\text{ V})$ until the control parameter attains the ordinate of the crossing point between the line itself and the solid black curve, which denotes the locus of the Hopf bifurcation capacitance $\hat{C}(Q)$ versus the memristor operating point Q for $R_L = 50\,\Omega$. For example, Figure 11b shows the oscillator phase portrait for an exemplary pre-bifurcation scenario, corresponding to the assignment of a value of 5 nF to the capacitance. Plot (c,d) in the same figure demonstrates the eventual approach of the time waveform of the memristor voltage v_m (memristor state x) toward the ordinate V_m (abscissa Q) of the GAS operating point $\mathbf{Q}_{\mathcal{N}}$ of the oscillator when $C = 5$ nF for each initial condition considered in the derivation of the phase portrait shown in plot (b) of the same figure. An infinitesimally-small GAS limit cycle suddenly appears in the v_m versus x plane around the oscillator operating point $\mathbf{Q}_{\mathcal{N}}$, which concurrently loses stability, as soon as C increases up to $\hat{C}(Q = 377) = 9.336$ nF. As shown in plot (e) of the same figure, directly after the bifurcation, specifically for $C = 9.34$ nF, a phase-plane trajectory, initiated far away from the region, hosting the operating point, converges asymptotically toward the blue-colored isolated closed orbit. Plot (f) shows a close-up view of the limit cycle from plot (e), together with two new phase-plane trajectories, one in green and the other in orange, initiated within its local neighborhood the first inside and the latter outside its orbit, respectively, and spending a relatively large amount of time while spiralling clockwise toward it. Here the forward-time waveforms of memristor voltage (blue trace) and memristor state (red trace), depicted in plot (g), are infinitesimally-small almost-sinusoidal oscillations, which is a fingerprint of a Hopf supercritical bifurcation. Figure 11h shows through blue and red traces respectively the real and imaginary parts of the local admittance $Y_{\mathcal{N}}(j\omega)$ of either of the two equivalent cells, depicted in plots (e) and (f) of Figure 2, across the respective port A–B about $\mathbf{Q}_{\mathcal{N}}$ as a function of the angular frequency ω at the Hopf supercritical bifurcation point $C = \hat{C}(Q = 377) = 9.336$ nF. $Y_{\mathcal{N}}(j\omega; \mathbf{Q}_{\mathcal{N}})$ is found to vanish at the angular frequencies $\pm\hat{\omega}_{0,Z_{\mathcal{N}}}(\mathbf{Q}_{\mathcal{N}})$, where, correspondingly, its inverse function, i.e. the local impedance $Z_{\mathcal{N}}(j\omega; \mathbf{Q}_{\mathcal{N}})$ of either the Thévenin or the Norton cell at the respective port A–B about $\mathbf{Q}_{\mathcal{N}}$ admits a purely-imaginary complex conjugate pair of poles of the form $p_{\mp,Z_{\mathcal{N}}}(\mathbf{Q}_{\mathcal{N}}) = \mp j\hat{\omega}_{0,Z_{\mathcal{N}}}$, where $\hat{\omega}_{0,Z_{\mathcal{N}}}$, numerically equal to $3.146 \cdot 10^6 \cdot s^{-1}$, denotes the angular frequency of the infinitesimally-small oscillations developing across the circuit topology under focus at the bifurcation point. As shown in plot (g) of Figure 11, the period T of the oscillatory waveform in the memristor state x for $C = 9.34$ nF amounts to 1.998 μs, which, as expected, is rather close to the temporal duration of one cycle of the same signal, computed by theory as $\hat{T}(\mathbf{Q}_{\mathcal{N}}) = 2\pi/\left(\hat{\omega}(\mathbf{Q}_{\mathcal{N}})\right) = 1.997\,\mu\text{s}$, when the capacitance C attains the bifurcation threshold

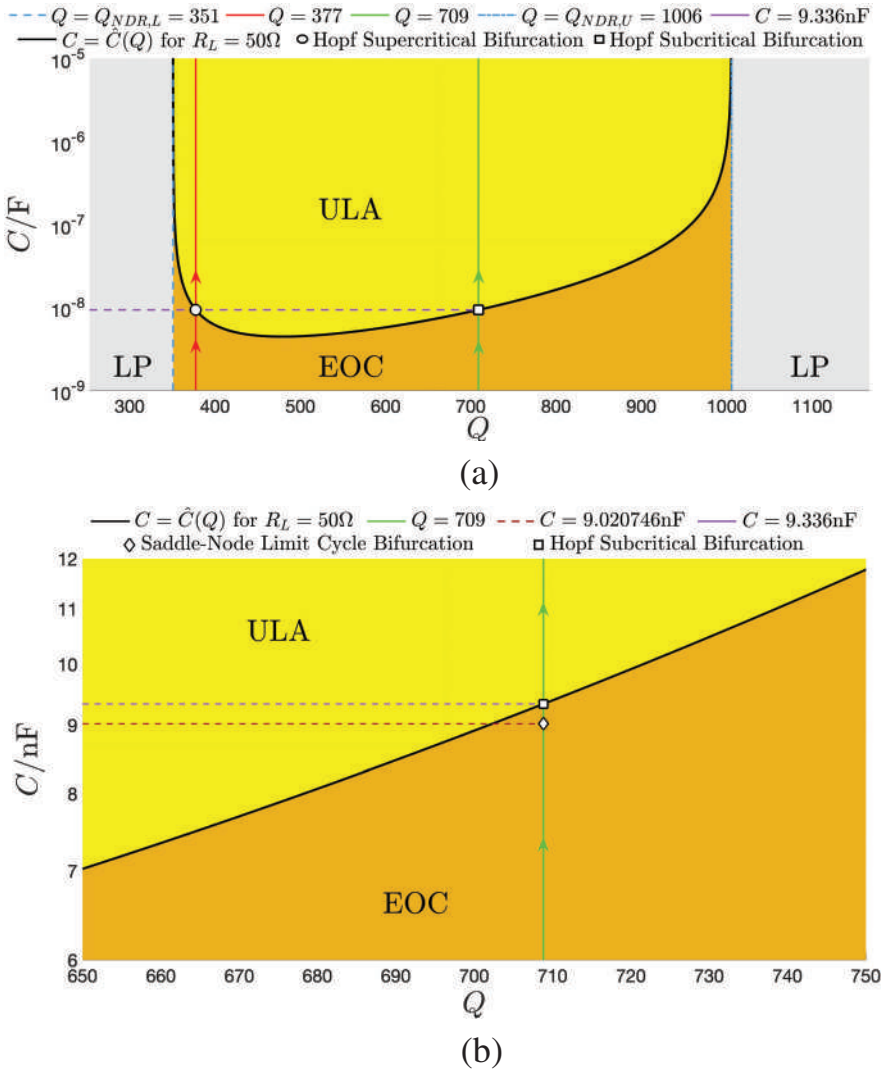

Figure 13. a) Illustration guiding the exploration of the local and global behavior of the relaxation oscillator of Figure 2e,f for a given value of the linear resistance, here set to 50 Ω, satisfying the inequality $R_L > \max_{Q\in(Q_{NDR,L},Q_{NDR,U})}|r(Q)| = |r(Q = 411)| = 21.427\Omega$, under sweep in one of the two possible bifurcation parameters of interest, namely the capacitance C, after fixing the other one, specifically the DC stimulus V_{in} (I_{in}). The plane is partitioned into regions of different colors, indicating the local activity and local stability properties of the second-order cell about a given operating point $\mathbf{Q}_{\mathcal{N}} = (Q, V_m)$ for each admissible capacitance value. When the memristor bias point **P** sits on a NDR branch of the DC I_m versus V_m locus, the cell is locally stable and locally active, i.e., on the Edge of Chaos (EOC), about $\mathbf{Q}_{\mathcal{N}}$ if the capacitance satisfies the inequality $C < \hat{C}(Q)$, whereas it is unstable and locally active (ULA) about the same operating point, otherwise (this is what happens in case study 4, where, additionally, **P** is unique). The solid black curve denotes the locus of the Hopf bifurcation capacitance $\hat{C}(Q)$ versus the memristor operating point Q for the above specified resistance value. Moving from bottom to top along the red (green) vertical line, i.e., fixing the memristor operating point Q to 377 (709) by setting V_{in} to 1.137 V (1.72 V), or, equivalently, I_{in} to 22.740 mA (34.400 mA), and increasing the capacitance from 0, the voltage-driven cell of Figure 2e, or, equivalently, the current-driven cell of Figure 2f is found to experience a local Hopf bifurcation of supercritical (subcritical) nature at $C = \hat{C}(Q) = 9.336$ nF, as indicated through a black hollow circle (square) marker. In the latter case the Thévenin cell, or, equivalently, the Norton cell is earlier on also subject to a global saddle-node limit-cycle bifurcation for $C = \tilde{C} = 9.020746$ nF, as indicated through a black hollow diamond marker in (b), showing a close-up view of the diagram in (a) around the area where the vertical line $Q = 709$ crosses the bifurcation locus $C = \hat{C}(Q)$. In anticipation for the analysis in Section 6.2, had we moved from left to right along a horizontal path passing first through the black hollow circle marker and then through the black square marker (see the dashed violet segment), i.e., had we increased the DC voltage V_{in} from 0 V to 1.72 V, or, equivalently, the DC current I_{in} from 0 A to 34.400 mA, after fixing the capacitance C to 9.336 nF, the voltage-driven cell in Figure 2e, or, equivalently, the current-driven cell in Figure 2f would have undergone first a local Hopf Bifurcation of Supercritical nature when V_{in} had attained the value of 1.137 V, i.e., equivalently, when I_{in} had attained the value of 22.740 mA, where $Q = 377$, and then a local Hopf Bifurcation of Subcritical nature when V_{in} had attained the value of 1.72 V, i.e., equivalently, when I_{in} had attained the value of 34.400 mA, where $Q = 709$, respectively. In fact, as explained in detail later on, following this bias input-controlled bifurcation path also past the second square marker, as shown in Figure 20, the Thévenin (Norton) cell would have effectively operated as a Hodgkin–Huxley neuristor, which explains the origin for the name attributed to the proposed voltage-driven (current-driven) bio-inspired oscillator. b) Close-up view of the C versus Q diagram from plot (a) magnifying the region around the Global Saddle-Node Limit Cycle Bifurcation – see the black hollow market on the point (Q, C) with abscissa $Q = 709$ and ordinate $C = \tilde{C} = 9.020746$ nF) – along the vertical green-colored bifurcation path, which the Thévenin (Norton) cell follows under capacitance control for $V_{in} = 1.72$ V ($I_{in} = 34.400$ mA).

$\hat{C}(Q) = 9.336$ nF. The size of the stable limit cycle keeps growing as the capacitance is further increased beyond the bifurcation point, as may be evinced by comparing the phase portrait in Figure 11f, derived for $C = 9.34$ nF, with the phase portrait in **Figure 12a**, obtained with $C = 50$ nF. As shown via a blue (red) trace in plot (b) of Figure 12, the steady-state oscillatory dynamics of the memristor sign-reversed voltage $-v_m$ (memristor state x) for $C = 50$ nF resemble rather closely the periodic behavior, which the potassium ion channel activation gating variable n (the membrane capacitance voltage v_m) may exhibit after transients vanish in the Hodgkin–Huxley neuron model, e.g., under a net synaptic current I_{in} of 9.70 μA, as may be inferred by inspecting the blue (red) waveform in plot plot (d) of Figure 1. Plot (c) of Figure 12 illustrates for $R_L = 50$ Ω the bifurcation diagram of the second-order relaxation oscillator, in either the voltage-driven circuit topology from plot (e) of Figure 2 for $V_{in} = 1.137$ V, or the equivalent current-driven circuit topology from plot (f) of Figure 2 for $I_{in} = V_{in}/R_L = 22.740$ mA, on the v_m versus C plane across the capacitance range [0, 100 nF], which includes the Hopf supercritical bifurcation point $\hat{C}(Q = 377) = 9.336$ nF. Locally, i.e., directly after the bifurcation, the amplitude of the GAS limit cycle grows as the square root of the modulus of the difference between the control parameter C and the bifurcation point $\hat{C}$, which is a hallmark of a Hopf bifurcation. Finally, for $V_{in} = 1.137$ V and $R_L = 50$ Ω, the arrows on the blue (red) trace in Figure 12d show how the location of the pole $p_{-,Z_{\mathcal{N}}}(\mathbf{Q}_{\mathcal{N}})$ ($p_{+,Z_{\mathcal{N}}}(\mathbf{Q}_{\mathcal{N}})$) of the local impedance $Z_{\mathcal{N}}$ of either the Thévenin cell from Figure 2e or the equivalent Norton cell from Figure 2f with $I_{in} = V_{in}/R_L$ at the respective port A–B about $\mathbf{Q}_{\mathcal{N}}$ changes as the capacitance C is increasingly stepped from the lower to the upper bound over the range [0.9507nF, 1 μF]. When the capacitance C attains the critical value $\hat{C} = 9.336$ nF, the poles, indicated via hollow circle markers, form a purely-imaginary complex conjugate pair of the form $p_{\mp,Z_{\mathcal{N}}}(\mathbf{Q}_{\mathcal{N}}) = \mp j\hat{\omega}_0(\mathbf{Q}_{\mathcal{N}})$, with $\hat{\omega}_0(\mathbf{Q}_{\mathcal{N}}) = 3.146 \cdot 10^6 \text{s}^{-1}$ (recall plot (h) of Figure 11), which is a necessary condition for the occurrence of a Hopf bifurcation in a second-order dynamical system.

4.b In the second one-parameter bifurcation scenario, occurring in case study 4 while increasing the value assigned to the capacitance from 0, the Thévenin cell of Figure 2(e), or, equivalently, the Norton cell of Figure 2f, where $I_{in} = V_{in}/R_L$, is first found to feature a locally active and GAS operating point $\mathbf{Q}_{\mathcal{N}}$, similarly as discussed in item 4.a. However, differently from what is the case in the first bifurcation scenario, here either of the two equivalent cells undergoes a major global bifurcation at some capacitance value $\tilde{C}$ preceding the critical Hopf bifurcation threshold $\hat{C}(Q)$. This global bifurcation generates a large semi-stable isolated closed orbit, called saddle-node limit cycle (SNLC), which attracts trajectories initiated outside it, but repels those starting off inside it. In fact, if the initial condition is chosen within the saddle-node limit cycle, either of the two system eventually approaches the operating point $\mathbf{Q}_{\mathcal{N}}$, which, as a result, maintains a stable nature, yet of local form only. As the control parameter is further increased, the semi-stable isolated closed orbit splits into a couple of different isolated closed orbits, one of which, namely a stable limit cycle (SLC), encloses the other one, namely an unstable limit cycle (ULC), which in its turn surrounds the locally-stable operating point. In this phase either of the two equivalent electrical systems exhibits a new interesting type of bi-stability, which differs from the steady-state behavior, featuring one of two admissible quiescent forms, depending upon the initial condition, which was illustrated in Figure 9. Here, in fact, the current-driven dynamical system, modeled via the equation pair (37)–(38), or its equivalent voltage-driven dynamical system, described by the same second-order ODE set with $I_{in} = V_{in}/R_L$, asymptotically converges toward a quiescent condition, where the respective state vector $[x, v_m]^{\text{T}}$ sits at some operating point $\mathbf{Q}_{\mathcal{N}} = (Q, V_m)$ on the phase plane after transients decay to zero, only when the initial condition is chosen inside the inner unstable limit cycle. On the other hand, either of the two bio-inspired systems is found to behave as an oscillator, with the respective solution trajectory revolving periodically along the outer stable limit cycle on the v_m versus x plane at steady state, when the initial condition is taken outside the inner unstable limit cycle. Assigning larger values to the capacitance, the amplitude of the unstable limit cycle is found to experience a dramatic decrease, until it reduces to zero for $C = \hat{C}(Q)$. Here either of the memristor circuits in Figure 2e,f experiences a local Hopf subcritical bifurcation, which destabilizes the respective operating point, while signalling the end of the life cycle of the unstable oscillations. For $C > \hat{C}(Q)$, irrespective of the initial condition, the state vector $[x, v_m]^{\text{T}}$ of the current-driven memristive system (37)–(38), or of its equivalent voltage-driven memristive system, described by the same equation pair with $I_{in} = V_{in}/R_L$, is found to converge asymptotically toward the large limit cycle, which now denotes the only admissible attractor in the phase plane. As a pedagogical example, as illustrated in **Figure 14a**, the NbO_x threshold switch is now polarized in the NDR bias point $\mathbf{P} = (V_m, I_m) = (0.85\text{ V}, 17.446\text{ mA})$, admitting consequently the operating point $Q = 709$, upon setting V_{in} and R_L to 1.72 V and 50 Ω respectively in the DC circuit of Figure 2c. In fact, exploiting the double-valuedness of the Q versus C locus in Figure 13a, the bias parameter pair (V_{in}, R_L) was selected here on purpose as just specified, so as to ensure that a Hopf bifurcation—see the black hollow square marker in the same figure—would have appeared across either the Thévenin cell of Figure 2e or its equivalent Norton cell of Figure 2f for the very same capacitance value, specifically $\hat{C}(Q = 709) = 9.336$ nF, as in the exemplary case study, where $\hat{C}(Q = 377) = 9.336$ nF, from the other possible bifurcation scenario, which either of the two cells may experience under capacitance sweep, as discussed in item 4.a above. However, unlike what was observed in the case study discussed in item 4.a, increasing the cell capacitance from 0 along the vertical solid green line in the C versus Q diagram of Figure 13a, any solution trajectory on the phase plane of either of the two equivalent cells is found to converge toward the respective operating point $\mathbf{Q}_{\mathcal{N}} = (Q, V_m) = (709, 0.85\text{ V})$ only as long as the capacitance C is kept smaller than $\tilde{C} = 9.020746$ nF, as is the case, for example, for $C = 5$ nF (refer to the phase portrait in plot (b) of Figure 14). Just before the

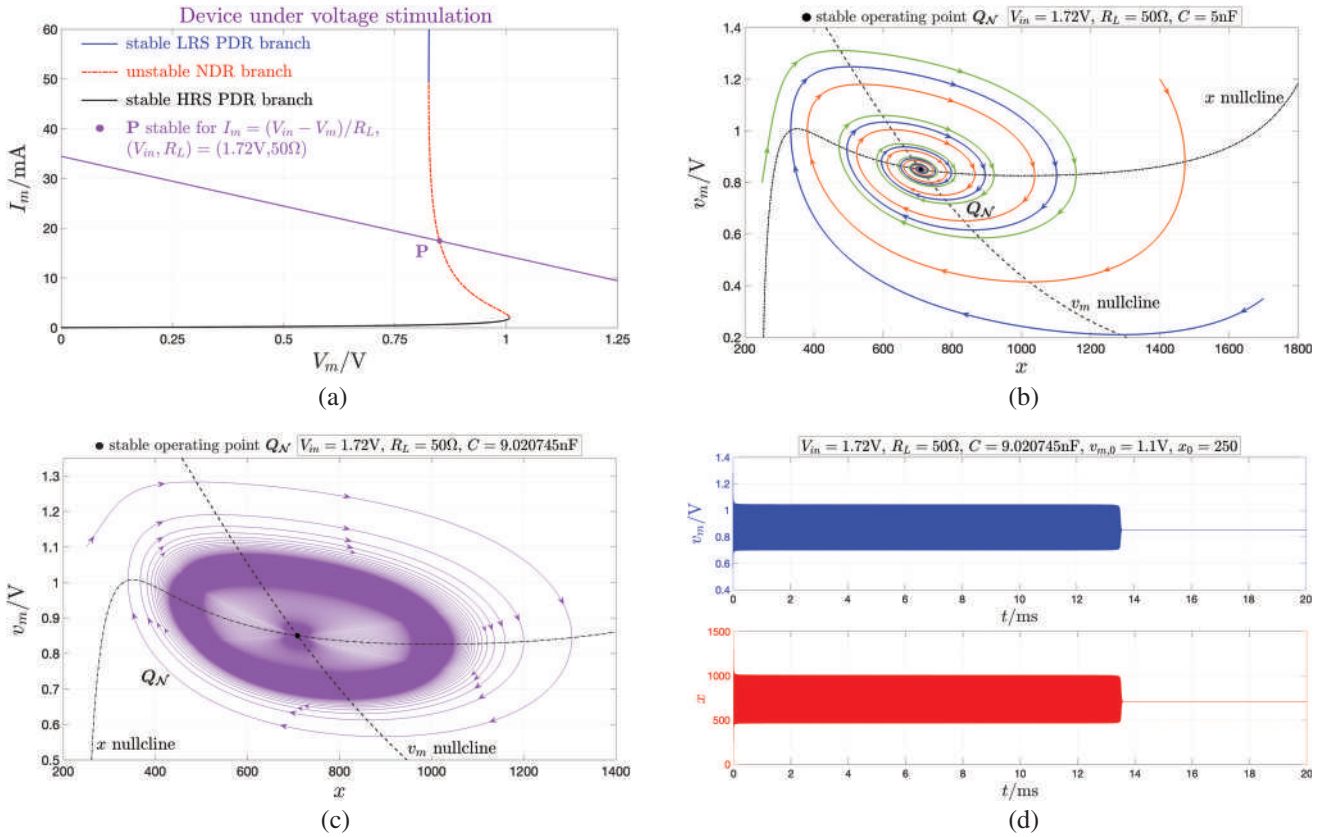

Figure 14. a) Illustration showing how the choice of a bias parameter pair (V_{in}, R_L) of the form (1.72 V, 50 Ω) allows to endow the NbOx threshold switch with a single NDR bias point **P** at (V_m, I_m) = (0.85 V, 17.446 mA). Despite this graph was already part of Figure 4(c), it is reported here once again given its significance in the oscillator design procedure. The memristor operating point $Q = X$ corresponding to the above specified bias point **P** is the real number 709. b) Phase portrait of the second-order system (37)–(38) for $I_{in} = V_{in}/R_L = 34.400$ mA, and $C = 5$ nF. The system operating point $\mathbf{Q}_{\mathcal{N}} = (Q, V_m)$, fixed at (709, 0.85 V) throughout the capacitance sweep, is now unique, and locally active, while featuring a stable nature, as indicated through the use of a black filled circle to mark its location in the phase plane. c) Evolution of the solution trajectory of the aforementioned ODE set under the same DC current stimulus as in (b) across the v_m versus x plane from an initial condition lying far away from $\mathbf{Q}_{\mathcal{N}}$ for $C = 9.020745$ nF. The phase-plane trajectory revolves a large number of times in the region, where a semistable limit cycle is about to appear, as it spirals toward the GAS operating point. d) Blue (red) trace: progressive approach of the memristor voltage (memristor state) toward the ordinate $V_m = 0.85$ V (abscissa $X = 709$) of $\mathbf{Q}_{\mathcal{N}}$, as observed in the numerical simulation which resulted in the v_m versus x locus from plot (c). e) Locus of v_m versus x extracted from the solutions to the above specified ODE set with $I_{in} = 34.400$ mA for an initial condition holding a large distance from $\mathbf{Q}_{\mathcal{N}}$ at the saddle-node limit cycle bifurcation point $C = \tilde{C} = 9.020746$ nF. The phase-plane trajectory approaches asymptotically an isolated closed orbit, drawn with alternating red and blue dashes, and denoting the so-called saddle-node limit cycle (SNLC), a semistable isolated closed orbit attracting only v_m versus x loci initiated outside it. f) Steady-state behavior of memristor voltage (in red) and memristor state (in blue) as recorded in the numerical simulation which produced the solution trajectory in (e). g) Turquoise (Grey) trace: Locus of v_m versus x extracted from the solutions to the ODE set (37)–(38) for $I_{in} = 34.400$ mA from an arbitrary initial condition chosen inside the semistable saddle-node limit cycle (SNLC) under forward-time (reverse-time) flow conditions when $C = \tilde{C} = 9.020746$ nF. The turquoise trajectory converges toward $\mathbf{Q}_{\mathcal{N}}$, which keeps a stable nature, yet of local form only, through the global bifurcation. Since running time backwards changes the stability properties of all the admissible steady states of a dynamical system, the grey phase-plane trajectory approaches asymptotically the SNLC. h) Blue (Red) trace: Time course of the memristor voltage (memristor state) as recorded from the numerical simulation which generated the turquoise v_m versus x locus in (g). i) Violet (Green) trace: Memristor voltage versus memristor state locus extracted from the solutions to the earlier specified ODE set under the same DC current stimulus as in (g) from an initial condition located outside the isolated closed blue solid orbit denoting a stable limit cycle (SLC) (between the isolated closed red dash-dotted orbit denoting an unstable limit cycle (ULC) and the isolated closed blue solid orbit denoting a stable limit cycle (SLC)) for $C = 9.2$ nF. Both these phase-plane trajectories approach asymptotically the stable limit cycle. As soon as the capacitance was increased through the global bifurcation point, the SNLC splitted into two distinct limit cycles, of which one, of unstable nature, lay entirely inside the other, of locally-stable nature, enclosing in its turn the second locally-stable attractor, specifically $\mathbf{Q}_{\mathcal{N}}$. Importantly, here and throughout this manuscript, the direction of arrows, superimposed on top of an unstable limit-cycle, shows how the trajectory point in the two-dimensional plane under focus would evolve along it under forward-time flow. Further relatively-small increases in the control parameter C determine on one hand a mild growth in the size of the SLC, and on the other hand a major dramatic reduction in the dimensions of the ULC. j) Steady-state time course of v_m (in blue) and x (in red) as resulting from the numerical simulation which produced the green phase-plane trajectory in (i). k) Turquoise (Grey) trace: v_m versus x locus resulting from the solutions to the aforementioned ODE set under the DC current input specified in (g) from an arbitrary initial condition lying inside the unstable limit cycle under forward-time (reverse-time) flow conditions for $C = 9.2$ nF. The first (latter) solution trajectory spirals progressively toward the operating point (the ULC). (l) Blue (Red) trace: memristor voltage (memristor state) over time as observed during the numerical simulation which resulted in the turquoise phase-plane trajectory from (k). m) Blue (Red) trace: v_m (x) over time as recorded at steady state from the numerical simulation which generated the grey solution trajectory in (k). Importantly, here and throughout this manuscript, solutions to the second-order cell ODE model, attaining asymptotically an unstable oscillatory steady state, were obtained by reversing the direction of

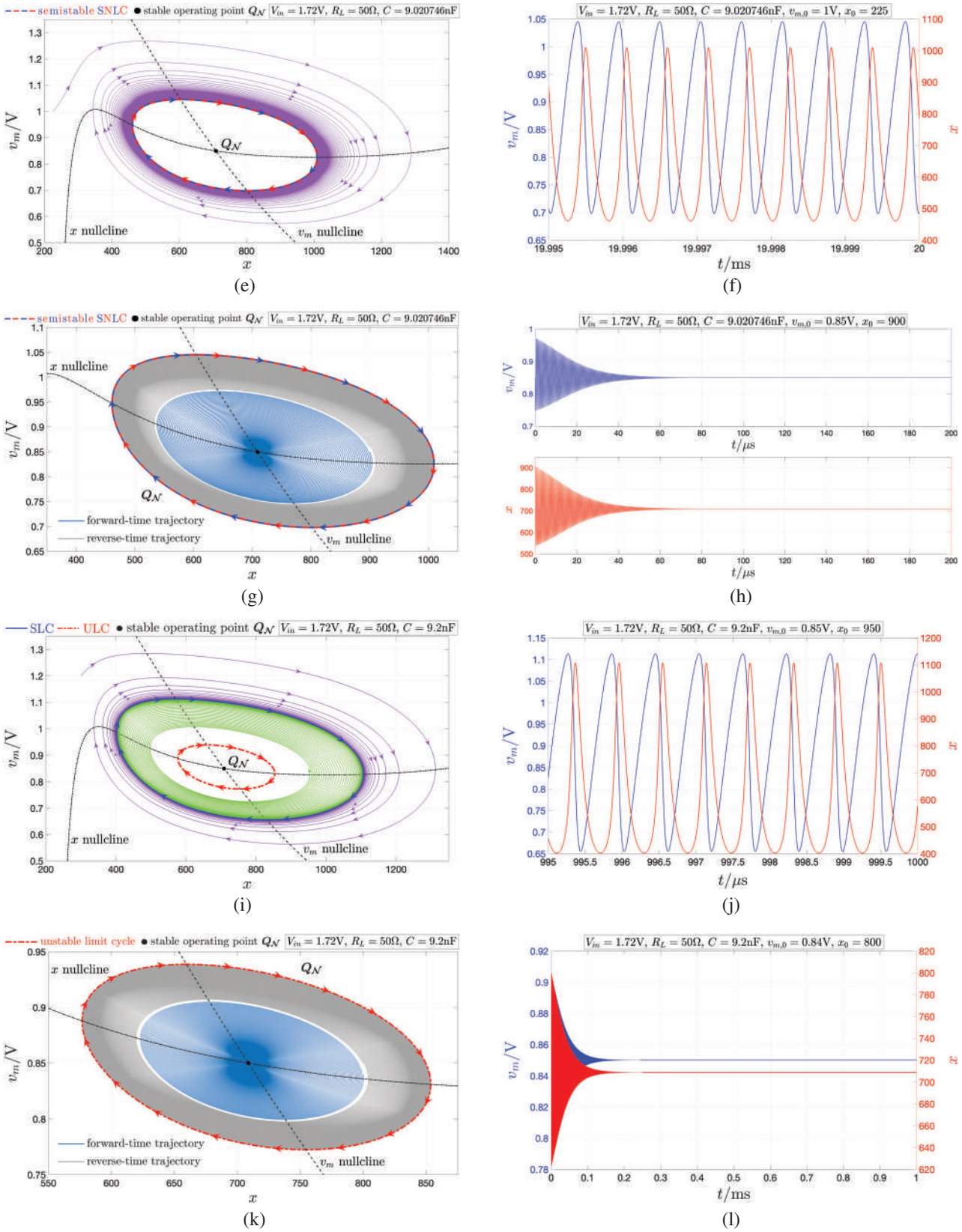

Figure 14. *Continued*

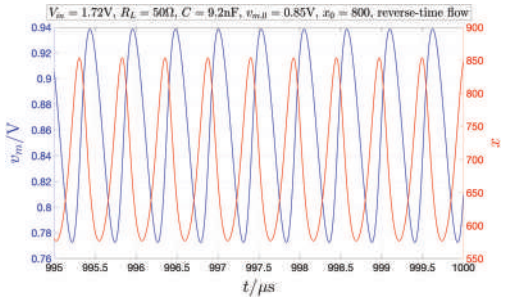

(m)

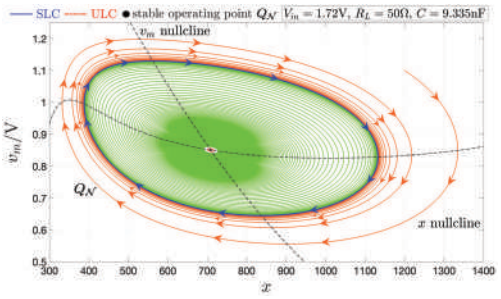

(n)

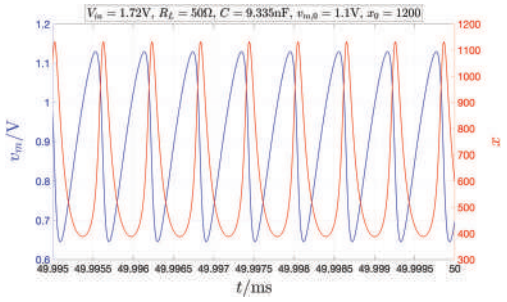

(o)

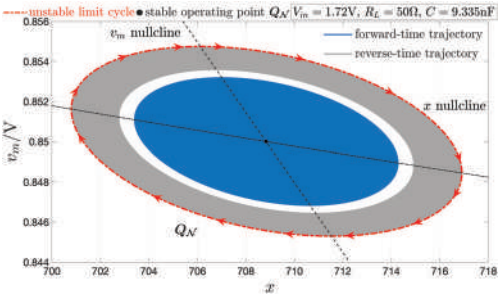

(p)

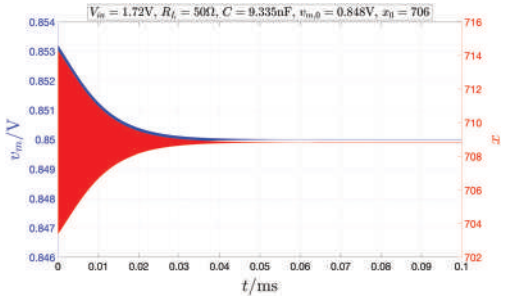

(q)

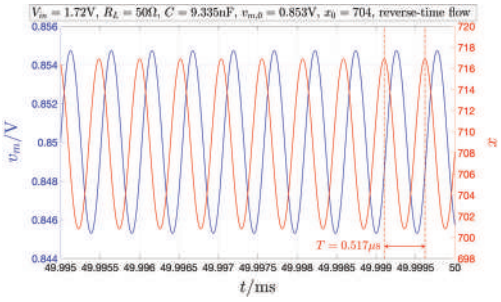

(r)

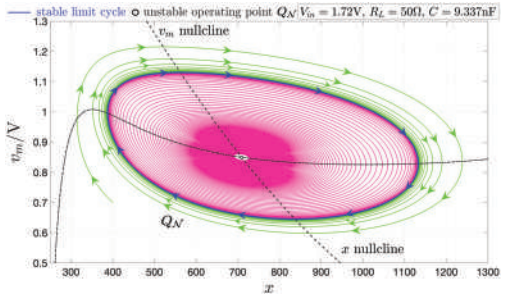

(s)

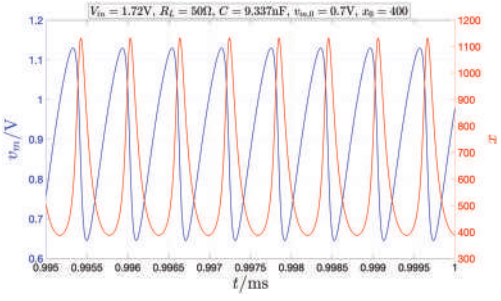

(t)

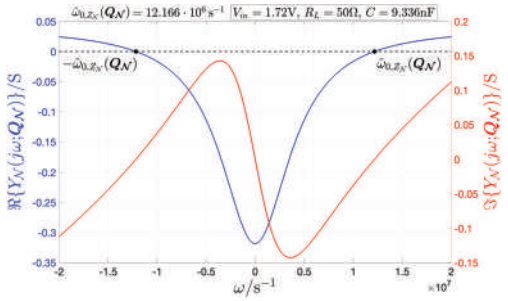

(u)

Figure 14. *Continued*

saddle-node limit-cycle bifurcation, i.e., for $C = 9.020745$ nF, any phase-plane trajectory, initiated far away from $\mathbf{Q}_{\mathcal{N}}$, spends a considerable number of revolutions within the region, where the global bifurcation phenomenon is about to occur in the 2D v_m versus x space, before spiralling asymptotically toward the GAS operating point, as shown in Figure 14c. The top (bottom) blue (red) trace in plot (d) of the same figure shows the time waveform of the memristor voltage v_m (memristor state x) for $C = 9.020745$ nF. A relatively-large semi-stable limit cycle, encircling the operating point $\mathbf{Q}_{\mathcal{N}}$, which concurrently keeps a stable nature, yet of local form only, suddenly appears in the phase-plane for $C = 9.020746$nF. This global dramatic phenomenon is indicated through a black hollow marker along the bifurcation route corresponding to the vertical green solid line $Q = 709$ in Figure 13b, visualizing a a zoom-in view of the C versus Q diagram from plot (a) of the same figure around the local Hopf subcritical bifurcation point $(Q, \hat{C}(Q)) = (709, 9.336\,\text{nF})$. As shown in Figure 14e, a solution trajectory, initiated outside the saddle-node limit cycle, which is marked with a line of alternating blue- and red-colored dashes, asymptotically converges toward it. The blue (red) trace in plot (f) shows the steady-state behavior of the memristor voltage v_m (memristor state x) in this case. The turquoise (grey) trace in plot (g) is a v_m versus x locus extracted from samples of the state variables in a numerical simulation of the second-order ODE set (37)–(38) with $I_{in} = V_{in}/R_L$, $(V_{in}, R_L) = (1.72\,\text{V}, 50\,\Omega)$, for an arbitrary initial condition chosen inside the semi-stable limit-cycle, and under forward-time (reverse-time) flow conditions. As expected, in the first (latter) case the solution trajectory tends toward the operating point (toward the semi-stable limit-cycle). The top (bottom) blue (red) trace in plot (h) depicts the time course of the memristor voltage (memristor state) in the forward-time simulation. Increasing the control parameter beyond $\tilde{C}$, the semi-stable saddle-node limit cycle splits into two limit cycles of different sizes. Specifically, the larger limit cycle is found to have a stable nature and to surround the smaller limit cycle, which in its turn encircles the operating point, but features an unstable nature. For example, Figure 14i illustrates the behavior, which either of the equivalent bio-inspired circuits in plots (e) and (f) of Figure 2 exhibits for any initial condition lying outside the inner unstable limit cycle, marked through a red-colored dash-dotted trace, for $C = 9.2$ nF. Here a phase-plane trajectory is eventually found to revolve along the solid blue-colored orbit denoting the outer stable limit cycle. The blue and red waveforms in plot (j) of Figure 14 show the steady-state oscillations in the memristor voltage and state under these circumstances. However, choosing the initial condition inside the unstable limit cycle, a forward-time solution trajectory converges asymptotically toward the locally-stable operating point, as illustrated by the v_m versus x locus marked through a turquoise solid trace in plot (k) of Figure 14. Correspondingly the time course of the memristor voltage (memristor state) is illustrated through a blue (red) trace in plot (l) of the same figure. Running the time backward from any initial condition inside the stable limit cycle, the respective phase-plane trajectory is found to revolve around the unstable limit cycle after transients decay to zero. For example, the grey-colored solution trajectory in Figure 14k shows the reverse-time behavior of either of the two equivalent cells for an initial condition located inside the unstable limit cycle. Here at steady state the memristor voltage (memristor state) is found to admit the oscillatory waveform depicted as a blue (red) trace in plot (m) of the same figure. The outer stable (inner unstable) limit cycle mildly (dramatically) grows (shrinks) with further increases in the capacitance. Plot (n) of Figure 14 shows the phase portrait of the Thévenin cell of Figure 2e or of its equivalent Norton cell of Figure 2f for $C = 9.335$ nF, i.e., just before the

the time flow. n) Green (Orange) trace: phase-plane trajectory extracted from the solutions to the ODE (37)–(38) with $I_{in} = 34.400$ mA from an initial condition lying outside the SLC (between the ULC and the SLC) for $C = 9.335$ nF, i.e. just before the occurrence of a local bifurcation, at which the area of the ULC reduces to zero, signalling the end of the life cycle of the unstable oscillations, and concurrently $\mathbf{Q}_{\mathcal{N}}$ loses stability. Both these v_m versus x loci eventually converge toward the SLC. o) Time waveform of memristor voltage (in red) and memristor state (in blue) as recorded at steady state in the numerical simulation which resulted in the orange solution trajectory from (n). p) Turquoise (Grey) trace: v_m versus x locus derived from the solutions to the earlier specified ODE set for the same DC current stimulus as in (n) from an arbitrary initial condition located inside the ULC under forward-time (reverse-time) flow conditions for $C = 9.335$ nF. The first (latter) phase-plane trajectory asymptotically approaches $\mathbf{Q}_{\mathcal{N}}$ (the ULC). q) Blue (red) trace: v_m (x) over time as observed in the numerical simulation which produced the turquoise solution trajectory from (p). r) Blue (red) trace: time course of the memristor voltage (memristor state) as derived after transients vanished from the numerical simulation which resulted in the grey v_m versus x locus from (p). As indicated, the period T of the unstable steady-state oscillation in the memristor state is found to be equal to 0.517 µs. s) Green (Magenta): phase-plane trajectory extracted from the solution to the ODE (37)–(38) with $I_{in} = 34.400$ mA from an arbitrary initial condition located outside the stable limit cycle (in the neighborhood of the operating point) for $C = 9.337$nF. Both the v_m versus x loci asymptotically approach the isolated closed blue solid orbit, which now denotes the only admissible attractor in the phase plane. In fact, the local Hopf subcritical bifurcation, which just occurred for $C = \hat{C}(Q = 709) = 9.336$ nF, determined the extinction of the unstable limit cycle, turned $\mathbf{Q}_{\mathcal{N}}$ into an unstable operating point, as indicated through the use of an hollow circle to mark its location in the v_m versus x plane, and ended up the system bistability regime, which started off at the global bifurcation point $\tilde{C} = 9.020746$ nF. t) Blue (Red) trace: steady-state time evolution of the memristor voltage (memristor state) as resulting from the numerical simulation which generated the green-coloured v_m versus x locus in (s) for $(x_0, v_{m,0}) = (400, 0.7\,\text{V})$. u) Real (in blue) and imaginary (in red) parts of the local admittance $Y_{\mathcal{N}}$ of either the Thévenin cell of Figure 2e for $V_{in} = 1.72$ V and $R_L = 50\,\Omega$ or the equivalent Norton cell of Figure 2f for $I_{in} = V_{in}/R_L = 34.400$ mA across the respective A–B port about the operating point $\mathbf{Q}_{\mathcal{N}}$ for $s = j\omega$ at the Hopf subcritical bifurcation point $C = \hat{C}(Q = 709) = 9.336$ nF as a function of the angular frequency ω. $Y_{\mathcal{N}}(j\omega; \mathbf{Q}_{\mathcal{N}})$ vanishes at $\pm\hat{\omega}_{0,Z_{\mathcal{N}}}(\mathbf{Q}_{\mathcal{N}})$, where $\hat{\omega}_{0,Z_{\mathcal{N}}}(\mathbf{Q}_{\mathcal{N}}) = 12.166 \cdot 10^6\,\text{s}^{-1}$ denotes the frequency of the infinitesimally-small sine-wave-alike oscillations developing for the first time across either of the two equivalent bio-inspired circuits under reverse-time flow conditions at the local bifurcation. The period $\hat{T}(\mathbf{Q}_{\mathcal{N}})$ of these oscillations is computable via $2\pi/(\hat{\omega}_{0,Z_{\mathcal{N}}}(\mathbf{Q}_{\mathcal{N}})) = 0.516\,\mu\text{s}$. As expected $\hat{T}(\mathbf{Q}_{\mathcal{N}})$ is close to the period of the unstable steady-state oscillations in the memristor state from plot (r), where a value close to the local bifurcation point, specifically 9.335 nF, was assigned to the capacitance.

capacitance attains the Hopf bifurcation value $C = \hat{C}(Q)$, which, as anticipated earlier, is equal to 9.336 nF for $Q = 709$. Any phase-plane trajectory lying outside the tiny unstable limit cycle approaches the outer stable limit cycle. The time waveform, which the memristor voltage (memristor state) admits at steady state in these circumstances is shown via a blue (red) trace in plot (o) of the same figure. A zoom-in view of the phase plane in the small region, containing the unstable limit cycle, is shown in Figure 14p. Choosing arbitrarily an initial condition inside the unstable limit cycle, the corresponding forward-time (reverse-time) solution trajectory is found to converge asymptotically toward the locally-stable operating point (the unstable limit cycle), as illustrated by the turquoise (grey) v_m versus x locus in this figure. In the first (latter) case, the time evolution of the memristor voltage and state may be respectively evinced by inspecting the blue and red trace in plot (q,r) of Figure 14. When the capacitance is increased up to the critical value $C = \hat{C}(Q = 709) = 9.336$ nF the area enclosed by the unstable limit cycle reduces to zero. Here either of the two equivalent electrical systems experiences a Hopf subcritical bifurcation, beyond which the unstable limit cycle is no longer present in the 2D state space, $\mathbf{Q}_{\mathcal{N}}$ loses stability, and, consequently, all the phase-plane trajectories asymptotically evolve along the large stable limit cycle, as visualized in the phase portrait of plot (s) of Figure 14 for $C = 9.337$nF. Correspondingly, the time waveform of the memristor voltage (memristor state) is shown through a blue (red) trace in plot (t) of the same figure. Figure 14u shows that both the real part (refer to the blue trace) and the imaginary part (refer to the red trace) of the local admittance $Y_{\mathcal{N}}$ of either the voltage-driven cell of Figure 2e or the equivalent current-driven cell of Figure 2f across the respective port A–B about the operating point $\mathbf{Q}_{\mathcal{N}}$ for $s = j\omega$ vanishes for $\omega = \mp\hat{\omega}_{0,Z_{\mathcal{N}}}(\mathbf{Q}_{\mathcal{N}})$, where $\hat{\omega}_{0,Z_{\mathcal{N}}}(\mathbf{Q}_{\mathcal{N}})$ is found to be equal to $12.166 \cdot 10^6 \text{s}^{-1}$, at the local bifurcation point $C = \hat{C}(Q)$. In fact $\hat{\omega}_{0,Z_{\mathcal{N}}}(\mathbf{Q}_{\mathcal{N}})$ defines the period $\hat{T}(\mathbf{Q}_{\mathcal{N}})$, amounting to $2\pi/(\hat{\omega}_{0,Z_{\mathcal{N}}}(\mathbf{Q}_{\mathcal{N}})) = 0.516\,\mu$s, which the unstable oscillations admit when they first develop with an almost-sinusoidal yet infinitesimally-small shape across either of the equivalent bio-inspired circuits at the Hopf subcritical bifurcation. As expected, with reference to Figure 14r, the time duration $T = 0.517\,\mu$s of one cycle in the steady-state periodic waveform, which the memristor state admits under reverse-time flow conditions for any initial condition inside the stable limit cycle when the capacitance C is equal to 9.335 nF, is rather close to $\hat{T}(\mathbf{Q}_{\mathcal{N}})$. Similarly as in the exemplary case study from the first bifurcation route, which either of the two equivalent cells may possibly admit under capacitance sweep (refer to the descriptions in item 4.a), also here, increasing the value assigned to C further, the dynamics of the memristor voltage (state) are found to reproduce biomimetically the relaxation oscillations in the potassium ion channel activation gating voltage (the electrical voltage spike train across the membrane capacitance) in the Hodgkin-Huxley neuron model. For example, **Figure 15a** shows the phase portrait of either of the two equivalent electrical systems for $C = 50$ nF. The blue (red) trace in plot (b) of the same figure shows the time waveform, which the sign-reversed memristor voltage (the memristor state) correspondingly admits for any initial condition at steady state. Figure 15c shows for $R_L = 50\ \Omega$ the bifurcation diagram of either the voltage-driven relaxation oscillator in plot (e) of Figure 2 with $V_{in} = 1.72$ V or the equivalent current-driven relaxation oscillator in plot (f) of Figure 2 with $I_{in} = V_{in}/R_L = 34.400$ mA on the v_m versus C plane across the capacitance range [0, 100 nF]. Plot (d) of the same figure provides a zoom-in view of the bifurcation diagram from plot (c) over the capacitance range [8.8 nF, 9.6 nF], which includes both the saddle-node limit cycle and the Hopf subcritical bifurcation points. Finally, the blue and red traces in Figure 15e respectively show how under the bias parameter pair $(V_{in}, R_L) = (1.72\text{ V}, 50\ \Omega)$ the poles $p_{-,Z_{\mathcal{N}}}(\mathbf{Q}_{\mathcal{N}})$ and $p_{+,Z_{\mathcal{N}}}(\mathbf{Q}_{\mathcal{N}})$ of the local impedance $Z_{\mathcal{N}}$ of either the Thévenin cell from Figure 2e or its equivalent Norton cell with $I_{in} = V_{in}/R_L = 34.400$ mA from Figure 2f at the respective port A–B about the operating point $\mathbf{Q}_{\mathcal{N}}$ evolve around the complex plane during a monotonically-increasing sweep in the capacitance from the lower to the upper bound across the range [0, 1 μF]. A close-up view of the pole diagram for $C \in [4.859\text{ nF}, 1\ \mu\text{F}]$ is illustrated in plot (f) of the same figure. Here the hollow diamond (square) markers indicate the locations of the two poles of $Z_{\mathcal{N}}(s; \mathbf{Q}_{\mathcal{N}})$ at the saddle-node limit cycle (Hopf subcritical) bifurcation point. In particular, at the local bifurcation point $p_{+,Z_{\mathcal{N}}}(\mathbf{Q}_{\mathcal{N}}) = -p_{-,Z_{\mathcal{N}}}(\mathbf{Q}_{\mathcal{N}}) = j\hat{\omega}_{0,Z_{\mathcal{N}}}(\mathbf{Q}_{\mathcal{N}})$, with $\hat{\omega}_{0,Z_{\mathcal{N}}}(\mathbf{Q}_{\mathcal{N}}) = 12.166 \cdot 10^6 \text{s}^{-1}$ (recall Figure 14u).

Having studied the two admissible bifurcation routes, which either the Thévenin cell from Figure 2e or its equivalent Norton cell with $I_{in} = V_{in}/R_L$ from Figure 2f may undergo under capacitance sweep, it is now of interest to study the local and global phenomena, which may possibly emerge across either of the two equivalent bio-inspired memristive circuits under a monotonic sweep in the respective DC stimulus.

6.2. Bifurcation Routes of the Bio-Inspired Oscillator Under Monotonic Stimulus Sweep

Three are the possible bifurcation scenarios, which the proposed second-order oscillator, accommodating a single memristor on Edge of Chaos, may undergo under monotonic sweep in its stimulus. The choice of the capacitance determines which of the three admissible bifurcation cascades will emerge across the bio-inspired cell under one-way input modulation. Let us first investigate the most interesting scenario, where an opportune choice for the capacitance lets the proposed second-order relaxation oscillator of Figure 2e,f supports the same bifurcation route under unidirectional DC voltage (current) sweep as a neuronal axon membrane under monotonic synaptic current modulation.

6.2.1. Programming the Cell to Reproduce the Classical Bifurcation Diagram of the Hodgkin–Huxley Neuron Model

Keeping R_L fixed to 50 Ω and sweeping the DC voltage (current) stimulus V_{in} ($I_{in} = V_{in}/R_L$) from 0 V (0 A) to 5 V (100 mA) allows to modulate the only possible GAS bias point of the memristor in the voltage-driven (current-driven) bio-inspired cell from

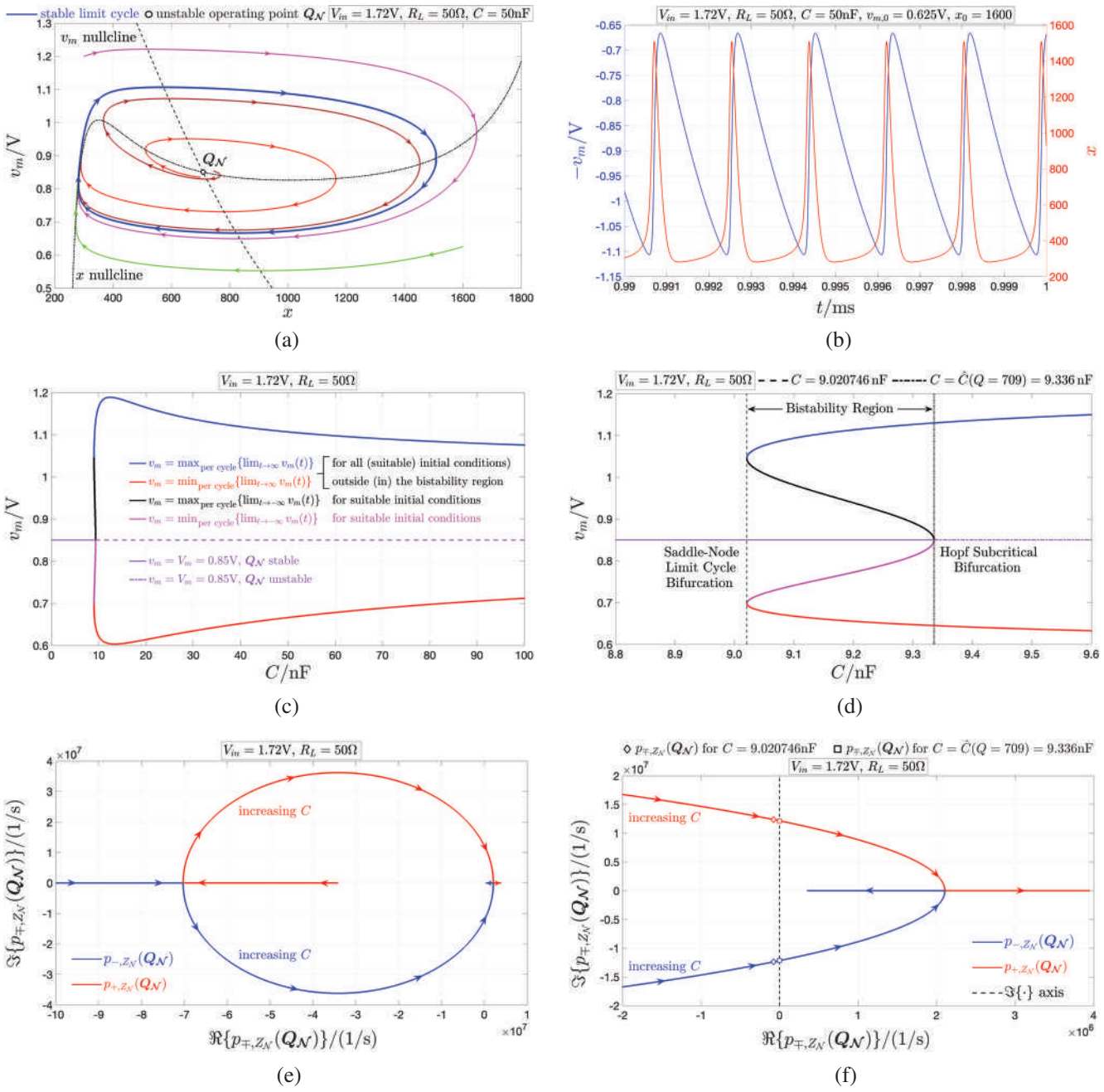

Figure 15. a) Phase portrait of the ODE (37)–(38) with $I_{in} = 34.400$ mA for $C = 50$ nF. All solution trajectories approach the GAS limit cycle. b) Red (blue) trace: steady-state time course of the sign-reversed memristor voltage (the memristor state) as resulting from the data series of the second (first) state variable in the numerical simulation which generated the green-colored v_m versus x loci from (a) for $(x_0, v_{m,0}) = (1600, 0.625\text{ V})$. As was the case in the exemplary case study from the first bifurcation scenario, described in item 4.a, which either the voltage-driven memristive circuit of Figure 2e for $V_{in} = 1.72$ V and $R_L = 50\ \Omega$ or its equivalent current-driven memristive circuit of Figure 2f for $I_{in} = 34.400$ mA may undergo under capacitance sweep, also here, assigning a relatively large value to the control parameter, specifically 50 nF, the steady-state behavior of the memristor voltage (memristor state) is reminiscent of the relaxation oscillations in the potassium ion channel activation gating variable (of the electrical voltage spike train across the membrane capacitance) in the Hodgkin–Huxley neuron model under suitable net synaptic current stimuli. c) Bifurcation diagram of the ODE set (37)–(38) for $I_{in} = 34.400$ mA on the memristor voltage versus capacitance plane across the C range [0, 100 nF]. For a given control parameter value, a point on the solid (dash-dotted) violet horizontal line $v = V_m = 0.85$ V indicates the stability (instability) of the system operating point $\mathbf{Q}_{\mathcal{N}} = (Q, V_m) = (709, 0.85\text{ V})$. Additionally, a point on the blue (red) trace, corresponding to a certain capacitance value beyond the global bifurcation threshold $\hat{C} = 9.020746$ nF, denotes the maximum (minimum) value $\max_{\text{per cycle}}\{\lim_{t\to\infty} v_m(t)\}$ ($\min_{\text{per cycle}}\{\lim_{t\to\infty} v_m(t)\}$) assumed by the capacitor voltage v_m over each cycle of the respective periodic waveform, when either of the two equivalent bio-inspired circuits experiences stable steady-state limit-cycle oscillations. While this occurs at all circumstances, when the capacitance is larger than the subcritical Hopf bifurcation threshold $C = \hat{C}(Q = 709) = 9.336$ nF), the initial condition $(x_0, v_{m,0}) \triangleq (x(0), v_m(0))$ to the earlier specified ODE set must be carefully chosen outside the unstable limit cycle for the phase-plane trajectory

Figure 2e,f. Referring without loss of generality to the voltage-driven circuit of Figure 2e, for each value, assigned to V_{in}, the DC load line of the circuit of Figure 2c crosses the I_m versus V_m characteristic of the NaMLab device in a single point, as illustrated for a number of cases in **Figure 16**.

With reference to Figure 13a, with R_L fixed to 50 Ω, setting the capacitance C to 9.336 nF, and sweeping the DC voltage V_{in} (I_{in}) from 0 V (0 A) to 5 V (100 mA) in the Thévenin (Norton) oscillator of Figure 2e,f induces a progressive leftward motion of the point (Q, C) along the violet horizontal line. As a result, from the analysis described in Section 6.1, the voltage-driven (current-driven) bio-inspired circuit undergoes two local Hopf Bifurcations, the first of Supercritical form and the second of Subcritical form, when the point (Q, C) respectively attains the locations ($Q = 377$, $\hat{C}(Q) = 9.336$ nF) and ($Q = 709$, $\hat{C}(Q) = 9.336$ nF), indicated in turn through the circle marker on the vertical red line and through the square marker on the vertical green line, which is the case when the DC voltage (current) stimulus V_{in} (I_{in}) is increased up to 1.137 V (22.740 mA) and 1.722 V (34.446 mA), correspondingly. In fact, as the monotonic increase in the DC voltage (current) stimulus goes on, a third dramatic phenomenon, particularly a Global Saddle-Node Bifurcation, is found to appear across the relaxation oscillator of Figure 2e,f for the aforementioned choice of the parameter pair (R_L, C) when V_{in} (I_{in}) attains the value of 1.748 V (34.953 mA), which allows to stabilize the memristor at the operating point $Q = 717$. We may thus conclude that for (R_L, C) = (50 Ω, 9.336 nF), a monotonic increase in the DC voltage (current) stimulus V_{in} (I_{in}) induces the emergence of the three-bifurcation cascade, which marks the life cycle of an Action Potential under synaptic current sweep across a biological axon membrane as predicted by the biologically-plausible Hodgkin–Huxley neuron model,[23] within the proposed second-order Thévenin (Norton) cell of Figure 2e,f. Referring once more to Figure 13(a), the application of concepts from Bifurcation Theory has thus allowed us to make a conscious choice for the resistance R_L and the capacitance C so as to allow either of the two equivalent bio-inspired memristive cells in plots (e) and (f) of Figure 2 to reproduce qualitatively, as the respective stimulus is progressively let grow, all the complex local and global bifurcations, which, according to Hodgkin and Huxley model, dictate birth, evolution and extinction of spiking oscillations across a neuronal membrane under a monotonic decrease in the net synaptic current.

Remark 7. Importantly, it is the rich locally-active dynamics, which the NaMLab memristor exhibits while operating around NDR bias points that allow our simple second-order analogue circuit, cast either in the Thévenin form or in the Norton form, to capture the complex bifurcation phenomena occurring in the fourth-order ODE set conceived by the two American luminaries under net synaptic current sweep through the interaction of just two state variables, which makes it the first and simplest ever reported bio-inspired circuit capable to undergo a Hopf Supercritical Bifurcation, a Hopf Subcritical Bifurcation, and a Global Saddle-Node Limit Cycle Bifurcation one after the other for a unique design parameter set under a monotonic modulation of the respective DC stimulus. In this regard, either of the proposed equivalent analogue circuits in plots (e) and (f) of Figure 2 may be dubbed a *Hodgkin–Huxley neuristor*.

Plots (a), (b,c), (d), (e,f), (g), (h,i), and (l) in **Figure 17** shows the phase portraits of the second-order ODE (37)–(38) with $I_{in} = V_{in}/R_L$ for $R_L = 50$ Ω and $C = 9.336$ nF when the constant DC stimulus V_{in} respectively attains the values 1.136 V, 1.137 V, 1.5 V, 1.7225 V, 1.745 V, 1.74766132 V, and 1.74766133 V within the sweep range [0, 5]V. The very same local and global phenomena, illustrated in plots (a), (b,c), (d), (e,f), (g), (h,i), and (l) of Figure 17, appear in the Norton cell of Figure 2f when $C = 9.336$ nF if the DC current stimulus I_{in} is respectively set to 22.720 mA, 22.740 mA, 30 mA, 34.450 mA, 34.900 mA, 34.9532264 mA, and 34.9532266 mA. First of all, for each of the seven case studies considered in the gallery of phase portraits displayed in Figure 17, **Table 2** reports the corresponding DC voltage (current) stimulus V_{in} (I_{in}) for the Thévenin (Norton) circuit of Figure 2e,f when $R_L = 50$ Ω and $C = 9.336$ nF, and further specifies each operating point $\mathbf{Q}_{\mathcal{N}} = (Q, V_m)$, which the voltage-driven (current-driven) cell may possibly admit, together with its stability properties. Increasing progressively the DC voltage (current) stimulus V_{in} (I_{in}) from 0 V (0 A), the voltage-driven (current-driven) cell of Figure 2e,f with $R_L = 50$ Ω and $C = 9.336$ nF is initially found to sit on some input-dependent globally asymptotically stable operating point. However, when V_{in} (I_{in}) attains the threshold value of 1.137 V (22.740 mA) the Thévenin (Norton) circuit undergoes a first local Hopf Bifurcation of Supercritical form, which destabilizes its operating point, while concurrently inducing the birth of an infinitesimally-small globally asymptotically stable limit-cycle around it on the 2D space spanned by memristor state x and capacitor or memristor voltage v_m. Immediately before the bifurcation, for $V_{in} = 1.136$ V ($I_{in} = 22.720$ mA), referred to as case study 1 in Table 2, a phase-plane trajectory initiated far away from the only operating point of the voltage-driven (current-driven) relaxation oscillator revolves a large number of times around the operating point itself before converging toward it eventually, as shown in Figure 17a, where the circle, marking the location of

point to revolve around the stable limit cycle at steady state when the system operates in the bistability regime, i.e., for $C \in (\tilde{C} = 9.020746\,\text{nF}, C = \hat{C}(Q = 709) = 9.336\,\text{nF})$. Last but not least, for a bifurcation parameter value falling within this very same range, a point on the black (magenta) trace denotes the maximum $\max_{\text{per cycle}}\{\lim_{t\to-\infty} v_m(t)\}$ (minimum $\min_{\text{per cycle}}\{\lim_{t\to-\infty} v_m(t)\}$) value assumed by the capacitor voltage v_m over each cycle of the respective periodic waveform, when the cell undergoes unstable steady-state limit-cycle oscillations, which is the case when the initial condition is chosen inside the stable limit cycle and the time is run backwards. d) Close-up view of the bifurcation diagram in (c) across the capacitance range [8.8 nF, 9.6 nF], which includes the global and local bifurcation points. Importantly, the cell keeps on the Edge of Chaos around $\mathbf{Q}_{\mathcal{N}}$ for each capacitance value smaller than the Hopf subcritical bifurcation threshold. e) Evolution of the poles $p_{-,Z_{\mathcal{N}}}(\mathbf{Q}_{\mathcal{N}})$ oriented blue trace) and $p_{+,Z_{\mathcal{N}}}(\mathbf{Q}_{\mathcal{N}})$ (oriented red trace) of the local impedance $Z_{\mathcal{N}}$ of either the Thévenin cell of Figure 2e for $V_{in} = 1.72$ V and $R_L = 50$ Ω or its equivalent Norton cell of Figure 2f for $I_{in} = V_{in}/R_L = 34.400$ mA across the respective port A–B about the operating point $\mathbf{Q}_{\mathcal{N}}$ across the complex plane under a monotonically-increasing sweep in the capacitance from the lower to the upper bound over the range [0, 1 μF]. f) Zoom-in view of the pole diagram in (e) across the capacitance range [4.859 nF, 1 μF]. The hollow diamond (square) markers indicate the locations of the two poles of $Z_{\mathcal{N}}(s; \mathbf{Q}_{\mathcal{N}})$ at the saddle-node limit cycle (Hopf subcritical) bifurcation point $C = \tilde{C} = 9.020746$ nF ($C = \hat{C}(Q = 709) = 9.336$ nF).

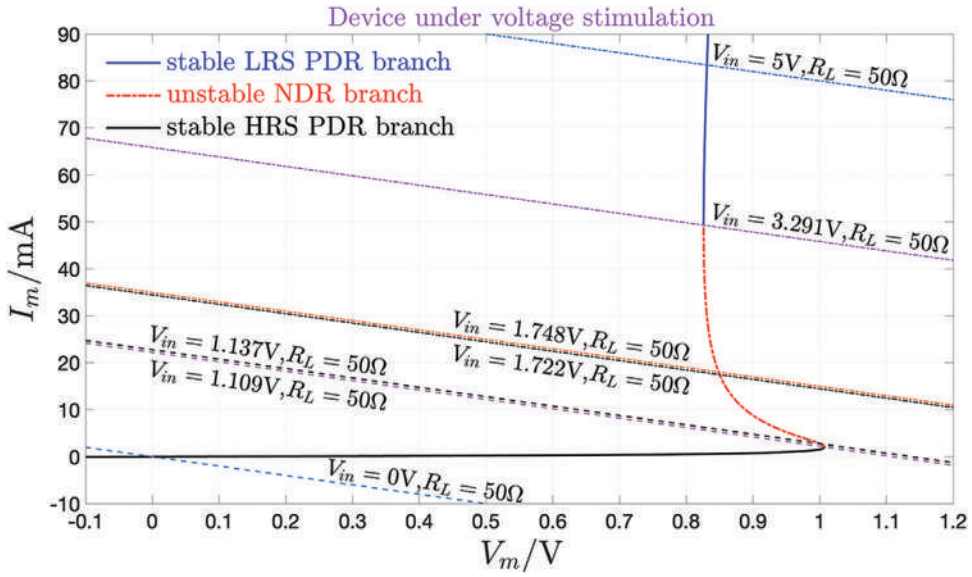

Figure 16. Modulation of the DC bias point $\mathbf{P} = (V_m, I_m)$ of the memristor in the Thévenin circuit of Figure 2e under a monotonic sweep in the DC voltage stimulus V_{in} from 0 V to 5 V for $R_L = 50\ \Omega$ and irrespective of the value assigned to the capacitance C. The monotonic increase in V_{in} determines a progressive upward shift in the graph of the load line of the DC circuit of Figure 2c, which allows to move the only admissible bias point of the memristor first along part of the HRS PDR branch, then along the entire NDR branch, and finally along part of the LRS PDR branch across the first quadrant of the DC I_m versus V_m plane. The stability properties indicated in the legend for the bias points along the memristor DC characteristic refer to the scenario where the device is directly driven by a constant voltage source, as indicated in Figure 2b. On the other hand, the use of a resistor of resistance $R_L = 50\ \Omega > \max_{Q\in(Q_{NDR,L}, Q_{NDR,U})} |r(Q)| = 21.427\Omega$ between the memristor and the DC voltage source, as shown in plot (c) of the same figure, allows to stabilize the entire NDR branch of the I_m versus V_m locus (recall Figure 4b). The load lines indicated in this plot are associated to value for the DC voltage stimulus V_{in} belonging to the set $S_{V_{in}} \triangleq \{0, 1.109, 1.137, 1.722, 1.748, 3.291, 5\}$V. The first (last) value in $S_{V_{in}}$ corresponds to the initial (final) point in the input sweep, and allows to endow the memristor with a HRS (LRS) PDR bias point. More of interest is the second (second last) value in $S_{V_{in}}$, as here the voltage stimulus stabilizes the memristor bias point at the frontier between HRS PDR branch (NDR branch) and NDR branch (LRS PDR branch). Most importantly, the third, fourth, and fifth values in $S_{V_{in}}$ correspond to points in the input voltage sweep, at which, with the memristor poised on NDR bias points featuring abscissas (ordinates) of decreasing (increasing) values, the second-order bio-inspired cell of Figure 2e with $R_L = 50\ \Omega$ undergoes a Hopf Supercritical Bifurcation, a Hopf Subcritical Bifurcation, and a Saddle-Node Limit Cycle Bifurcation, respectively, for $C = 9.336$ nF. Importantly, the three bifurcations occur in the voltage-driven second-order cell of Figure 2e while its threshold switch is polarised along the NDR branch of its DC V_m versus I_m characteristic. This provides clear evidence for the crucial impact of the memristor NDR on the emergence of the fundamental mechanisms, which underlie the life cycle of an Action Potential in a biological neuronal axon membrane, across a relaxation oscillator featuring half the number of degrees of freedom relative to the fourth-order reference model from Hodgkin and Huxley. The memristor bias point may be equivalently modulated by sweeping the DC input current $I_{in} = V_{in}/R_L$ in the Norton circuit of Figure 2f with $R_L = 50\ \Omega$ from 0 A to 100 mA irrespective of the capacitance value. In particular, assigning the i^{th} value in the set $S_{I_{in}} \triangleq \{0, 22.185, 22.740, 34.446, 34.953, 65.813, 100\}$mA to the DC input current I_{in} allows to poise the memristor in the Norton cell at the same operating point, which it admits in the Thévenin cell of Figure 2e when V_{in} assumes the i^{th} value in the set $S_{V_{in}} = \{0, 1.109, 1.137, 1.722, 1.748, 3.291, 5\}$V for $i\{1, 2, 3, 4, 5, 6, 7\}$. Most importantly, for $C = 9.336$ nF, the current-driven electrical circuit exhibits a Hopf Supercritical Bifurcation, a Hopf Subcritical Bifurcation, and a Saddle-Node Limit Cycle Bifurcation when its DC input current respectively assumes the values 22.740 mA, 34.446 mA and 34.953 mA, which in turn correspond to the points 1.137 V, 1.722 V, 1.748 V for the bias voltage stimulus in the voltage-driven circuit of Figure 2e.

the operating point, is drawn in the filled form to denote its stable nature. At the Hopf Supercritical Bifurcation point, i.e., for $V_{in} = 1.137$ V ($I_{in} = 22.740$ mA), referred to as case study 2 in Table 2, irrespective of the initial conditions assigned to memristor state and voltage, the Thévenin (Norton) circuit of Figure 2e,f undergoes infinitesimally-small almost-sinusoidal limit-cycle oscillations after transients fade away, as illustrated in plots (b) and (c) of Figure 17, where the blue solid isolated closed orbit denotes the stable limit cycle, while the circle, lying at the location of the operating point, is drawn in the hollow form to indicate its instability nature. The amplitude of the globally asymptotically stable limit cycle, encircling the unstable operating point on the phase plane of the Thévenin (Norton) circuit in plot (e,f) of Figure 2, grows as the DC voltage (current) stimulus is increased beyond the Hopf Supercritical Bifurcation threshold. For example, this may be evinced by inspecting Figure 17d, which depicts the phase portrait of the voltage-driven (current-driven) cell for $V_{in} = 1.5$ V ($I_{in} = 30$ mA), referred to as case study 3 in Table 2. When V_{in} (I_{in}) attains the critical value of 1.722 V (34.446 mA), the second-order bio-inspired memristor cell shown in plot (e,f) of Figure 2 undergoes a second local Hopf Bifurcation. However this time the Hopf Bifurcation, occurring across either of the two equivalent circuits, is of Subcritical form. As a result, it endows the sudden emergence of infinitesimally-small unstable limit-cycle oscillations across the Thévenin (Norton) circuit, while concurrently restoring the stability of the operating point, yet in a local sense only. In fact, this second local bifurcation signals the onset of a bistability operating regime for either of the two equivalent cells. In this regime, if the initial condition $[x_0, v_{m,0}]^T$ assigned to the state vector $[x, v_m]^T$ of the ODE system (37)–(38), modeling

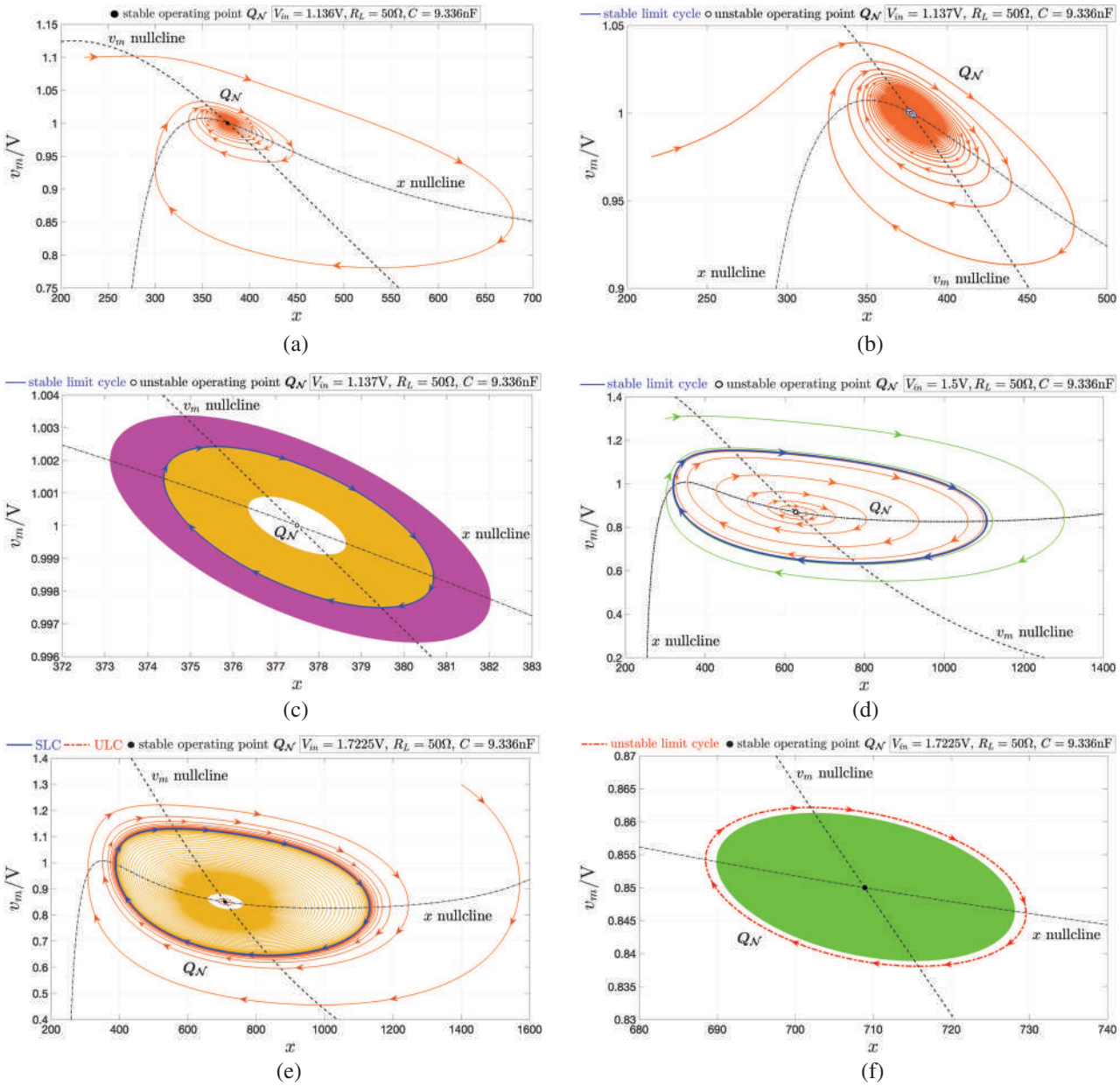

Figure 17. Gallery of phase portraits of the voltage-driven cell of Figure 2e in a scenario, where, the choice of an opportune value for the capacitance C, specifically 9.335 nF, given a suitable value, here 50 Ω, assigned preliminarily to the resistance R_L, induces across the respective circuit, subject to a DC voltage stimulus of progressively larger value, the emergence of the three-bifurcation-cascade, marking the most important life phases of an Action Potential in the Hodgkin–Huxley neuron model under a monotonic decrease in the net synaptic current. a) Asymptotic approach of the state vector of the second-order ODE (37)–(38) with $I_{in} = V_{in}/R_L$ toward a GAS operating point in case study 1 from Table 2, where V_{in}, equal to 1.136 V, is about to attain the Hopf Supercritical Bifurcation threshold. b) Clockwise spiralling approach of the trajectory point (x, v_m) toward a GAS infinitesimally-small limit cycle, along which it evolves cyclically after transients fade away, from an initial condition lying far away from the region of the phase plane hosting the periodic attractor, for V_{in} = 1.137 V, classified as case study 2 in Table 2, when the ODE system undergoes the first bifurcation. Specifically, the blue solid isolated closed orbit, corresponding to tiny almost-sinusoidal oscillatory solutions for memristor state and voltage, is spawned out of a Hopf Supercritical Bifurcation. c) Magenta (Ochre) trace: Phase-plane trajectory initiated outside (inside) the just-born GAS limit cycle, and approaching it as time goes by in case study 2. Another effect of the Hopf Supercritical Bifurcation is in fact to destabilize the operating point of the second-order relaxation oscillator. d) Green (Orange) trace: Phase-plane trajectory approaching the GAS limit cycle from an initial condition set outside (inside it) in case study 3 from Table 2 for V_{in} = 1.5V. The growth of the stable limit cycle, relative to its shape in case study 2, is evident. e) Phase portrait of the ODE set (37)–(38) with $I_{in} = V_{in}/R_L$ in case study 4, when V_{in}, equal to 1.7225 V, has just past over the Hopf Subcritical Bifurcation value of 1.722 V, at which the operating point $\mathbf{Q}_{\mathcal{N}}$ of the bio-inspired memristive system re-acquires a stable nature, yet in a local sense only, while an infinitesimally-small unstable limit cycle, enclosed entirely within the stable limit cycle, now displaying a significantly larger shape than what was the case in plot (c), is concurrently born in the phase plane around it. Orange (Yellow): Motion of a trajectory point (x, v_m) across the phase plane from an arbitrary initial condition chosen outside the stable limit cycle (between the stable and unstable limit cycles). f) Green trace: Temporal evolution of the state vector from an initial condition located inside the unstable limit cycle in case study 4. The Hopf Subcritical Bifurcation marks the onset of a phase, where the memristor state and voltage may

the voltage-driven cell with $I_{in} = V_{in}/R_L$ (modeling the current-driven cell), is chosen inside (outside) the unstable limit cycle, the memristor voltage and state will respectively converge toward the ordinate V_m and abscissa Q of the operating point $\mathbf{Q}_{\mathcal{N}}$ lying inside it (will revolve along periodic waveforms, which drawn one against the other point by point form the stable limit cycle enclosing it) after transients decay to zero. For example, the voltage-driven (current-driven) cell operates as a bistable for $V_{in} = 1.7225$ V ($I_{in} = 34.450$ mA), referred to as case study 4 in Table 2, as illustrated in plots (e) and (f) of Figure 17, where the unstable limit cycle appears as a red dash-dotted isolated closed orbit. As the DC voltage (current) stimulus is further increased, the amplitude of the inner smaller unstable limit cycle on the v_m versus x plane of the Thévenin (Norton) circuit is subject to a progressive significant increase, while the shape of the outer larger stable one, enclosing it, undergoes minor changes. This may be clearly inferred by comparing the shapes of the stable and unstable cycles in Figure 17g, illustrating the phase portrait of the circuit of Figure 2e,f for $V_{in} = 1.745$ V ($I_{in} = 34.900$ mA), referred to as case study 5 in Table 2, with the shapes of the blue solid and red dash-dotted isolated closed orbits, which were recorded on the phase plane of the voltage-driven (current-driven) cell for $V_{in} = 1.7225$ V ($I_{in} = 34.450$ mA), and were visualized in plot (e) of Figure 17, respectively. Eventually, when the DC voltage V_{in} (current I_{in}) stimulus attains the bifurcation value of 1.74766132 V (34.9532264 mA), which is referred to as case study 6 in Table 2, the two limit cycles on the phase plane of the Thévenin (Norton) circuit gently coalesce one into the other, forming a unique

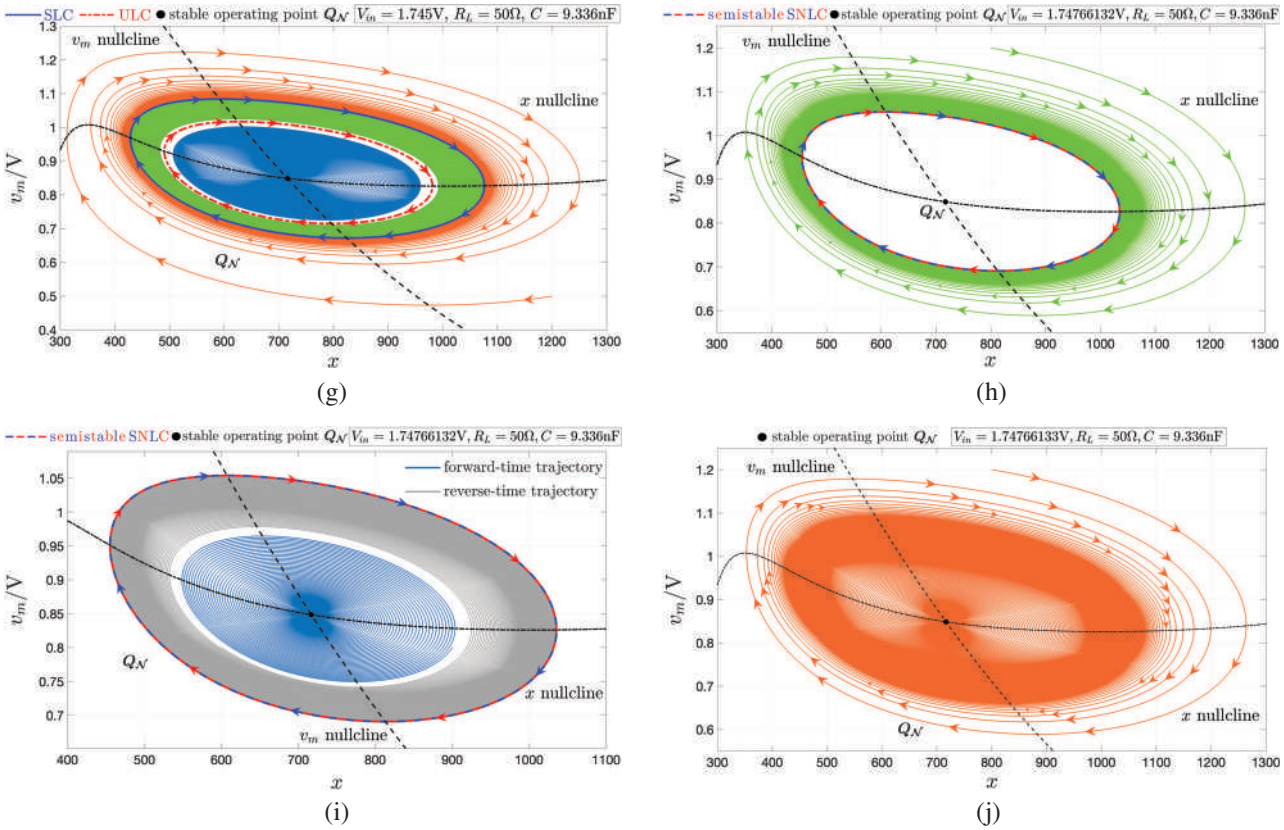

Figure 17. *Continued*

asymptotically display either of two admissible steady states, depending upon the initial condition, namely oscillations or quiescent levels when (x_0, $v_{m,0}$) lies outside or inside the unstable limit cycle, respectively, as shown in turn in plots (d) and (e) for case study 3. (g) Phase portrait of the proposed neuristor of Figure 2e in case study 5 from Table 2, where V_{in}, equal to 1.745 V, falls within the range of DC voltage stimuli endowing memristor state and voltage with two coexisting locally-stable steady states. While the orange and green phase-plane trajectories eventually follow repeatedly the blue closed route of the stable limit cycle, the turquoise phase-plane trajectory converges asymptotically toward the operating point. The growth of the unstable limit cycle, relative to its shape in case study 4, is evident. h) Clockwise spiralling motion of the phase-plane trajectory point (x, v_m) toward a semi-stable periodic attractor, along which the stable and unstable limit cycles coalesce one into the other in case study 6 from Table 2, where V_{in} attains the critical global Saddle-Node Limit Cycle Bifurcation value of 1.74766132 V, from an initial condition set outside the periodic attractor itself. i) Turquoise (Grey) trace: Forward-time (Reverse-time) evolution of the state vector of the ODE system (37)–(38) with $I_{in} = V_{in}/R_L$ from an arbitrary initial condition lying inside the semi-stable limit cycle in case study 6. j) Clockwise spiralling evolution of a phase-plane trajectory, initiated far away from the region, where the two limit cycles just merged gently one into the other, disappearing together from the v_m versus x plane as a result, toward the GAS operating point $\mathbf{Q}_{\mathcal{N}}$ in case study 7 from Table 2, where a value of 1.74766133 V, just above the global bifurcation threshold, was assigned to the DC voltage stimulus V_{in}. The very same gallery of phase portraits may be recorded from the analysis of the equivalent current-driven cell of Figure 2f upon setting the respective DC current stimulus according to the formula $I_{in} = V_{in}/R_L$ for each case study under exam.

Table 2. Operating point $\mathbf{Q}_{\mathcal{N}}$ and admissible attractors for the proposed second-order voltage-driven Hodgkin–Huxley Neuristor in plot (e) of Figure 2 for each of the 7 values assigned to the DC input voltage V_{in} to acquire the phase portraits displayed in plots (a)–(l) of Figure 17. Here R_L and C are respectively fixed to 50 Ω and $C = 9.336$ nF. The values to be assigned to the DC input current I_{in} to induce the same steady states in the equivalent Norton circuit of Figure 2f for each of the 6 case studies considered for the Thévenin cell are also tabulated below. Here GAS stands for *Globally Asymptotically Stable*, LS for *Locally Stable*, and SS for *Semi-Stable*.

Case study 1	V_{in}	$I_{in} = V_{in}/R_L$	Coordinates of the Operating Point $\mathbf{Q}_{\mathcal{N}} = (Q, V_m)$		Admissible Attractors
	1.136 V	22.720 mA	$Q = 376.39006$	$V_m = 1.00053$ V	GAS Operating Point
Case study 2	V_{in}	$I_{in} = V_{in}/R_L$	Coordinates of the Operating Point $\mathbf{Q}_{\mathcal{N}} = (Q, V_m)$		Admissible Attractors
	1.137 V	22.740 mA	$Q = 377.49093$	$V_m = 1.00002$ V	GAS Limit Cycle
Case study 3	V_{in}	$I_{in} = V_{in}/R_L$	Coordinates of the Operating Point $\mathbf{Q}_{\mathcal{N}} = (Q, V_m)$		Admissible Attractors
	1.5 V	30 mA	$Q = 627.66837$	$V_m = 0.87014$ V	GAS Limit Cycle
Case study 4	V_{in}	$I_{in} = V_{in}/R_L$	Coordinates of the Operating Point $\mathbf{Q}_{\mathcal{N}} = (Q, V_m)$		Admissible Attractors
	1.7225 V	34.450 mA	$Q = 708.89972$	$V_m = 0.84999$ V	LS Operating Point and LS Limit Cycle
Case study 5	V_{in}	$I_{in} = V_{in}/R_L$	Coordinates of the Operating Point $\mathbf{Q}_{\mathcal{N}} = (Q, V_m)$		Admissible Attractors
	1.745 V	34.900 mA	$Q = 715.98150$	$V_m = 0.84862$ V	LS Operating Point and LS Limit Cycle
Case study 6	V_{in}	$I_{in} = V_{in}/R_L$	Coordinates of the Operating Point $\mathbf{Q}_{\mathcal{N}} = (Q, V_m)$		Admissible Attractors
	1.74766132 V	34.9532264 mA	$Q = 716.808118$	$V_m = 0.8484621594$ V	LS Operating Point and SS Saddle-Node Limit Cycle
Case study 7	V_{in}	$I_{in} = V_{in}/R_L$	Coordinates of the Operating Point $\mathbf{Q}_{\mathcal{N}} = (Q, V_m)$		Admissible Attractors
	1.74766133 V	34.9532266 mA	$Q = 716.808121$	$V_m = 0.8484621588$ V	GAS Operating Point

isolated closed orbit of semi-stable nature called saddle-node limit cycle. At this point, the voltage-driven (current-driven) cell is said to undergo a global Saddle-Node Limit Cycle Bifurcation. As illustrated in plot (h) of Figure 17, if the initial condition to the second-order ODE (37)–(38) set of the voltage-driven cell with $I_{in} = V_{in}/R_L$ (of the current-driven cell) lies outside the semi-stable saddle-node limit cycle, appearing as an isolated closed orbit of alternating blue and red colours, the trajectory point $(x(t), v_m(t))$ is found to evolve eventually along the semi-stable limit cycle itself. As shown through a light blue (grey) phase-plane trajectory in plot (i) of Figure 17, when $(x_0, v_{m,0})$ lies inside the semi-stable saddle-node limit cycle, the memristor voltage and current of either of the two equivalent cells in plots (e) and (f) of Figure 2 converge asymptotically toward the value of the ordinate and abscissa of the locally-stable operating point $\mathbf{Q}_{\mathcal{N}}$, respectively, (exhibit eventually periodic behaviors corresponding to the semi-stable limit cycle) when the time is let evolve forward (backward). Directly after the global bifurcation phenomenon the voltage-driven (current-driven) neuristor exits the bistability operating regime. For any value of the DC voltage (current) stimulus beyond 1.74766132 V (34.9532264 mA), the Thévenin (Norton) cell admits a unique globally asymptotically stable operating point, as is the case, for example, when $V_{in} = 1.74766132$ V ($I_{in} = 34.9532264$ mA), referred to as case study 7 in Table 2. With reference to Figure 17l, here a trajectory solution, initiated far away from the region, where the two limit cycles just merged one into the other, spends a considerable amount of time in the phase-plane region, which hosted the semi-stable limit cycle, as it spirals progressively toward the globally asymptotically stable operating point.

Importantly, the v_m versus I_{in} bifurcation diagram of the bio-inspired memristive circuit in Norton form from plot (f) of Figure 2 is shown in **Figure 18**. Here the green (brown) trace represents a PDR (NDR) branch of the DC V_m versus I_{in} characteristic of the one-port seen across terminals A and B in the memristive bio-inspired circuit of Figure 2f. A bias point for this one-port, indicated as $\mathbf{P}_{\mathcal{N}} = (I_{in}, V_m)$, is unequivocally associated to one of the oscillator operating points, say $\mathbf{Q}_{\mathcal{N}} = (Q, V_m)$, and, therefore, to a particular memristor bias point $\mathbf{P} = (I_m, V_m)$. Increasing the bias current I_{in} monotonically across the range [0, 100 mA], the one-port and its memristor in the bio-inspired current-driven cell of Figure 2f are found to transition concurrently between the HRS PDR branch (the NDR branch) and the NDR branch (and the LRS PDR branch) of the respective DC V_m–I_{in} and V_m–I_m characteristics when I_{in} attains the level of 22.185 mA (65.813 mA). The NDR branch of the V_m versus I_{in} characteristic, drawn in the bifurcation diagram of Figure 18, is endowed with a solid (dash-dotted) line style, where it includes stable (unstable) bias points for the one-port with terminals A and B from Figure 2f, which is the case either for $I_{in} \in$ (22.185 mA, 22.740 mA) or for $I_{in} \in$ (34.446 mA, 65.813 mA) (for $I_{in} \in$ (22.740 mA, 34.446 mA)). For each DC input current I_{in} falling within the one-port bias point instability regime (22.740 mA, 34.446 mA) the bifurcation diagram accommodates one point, lying along the blue (red) trace at the ordinate corresponding to the maximum (minimum) value $\max_{\text{per cycle}}\{\lim_{t\to+\infty} v_m(t)\}$ ($\min_{\text{per cycle}}\{\lim_{t\to+\infty} v_m(t)\}$), which the memristor voltage $v_m(t)$ assumes over each cycle of the respective GAS periodic waveform as time approaches positive infinity (in practice, transients fade almost completely away over a finite amount of time). Furthermore, for each DC input current I_{in} belonging to the range (34.446 mA, 34.953 mA), the one-port seen across A and B in the relaxation oscillator of Figure 2f operates as a bistable dynamical system. As shown earlier, here a trajectory point (x, v_m) would be found to evolve across the phase plane toward a quiescent state (a stable limit cycle) if its initial condition were set inside (outside) yet another limit cycle, featuring an unstable nature, and enclosing the operating point while lying entirely inside the stable periodic attractor, thus separating the basins of attraction of the two coexisting locally-stable steady states for the state vector of the ODE set (37)–(38), which explains the origin for the name it is typically referred to in Nonlinear Dynamics Theory, namely

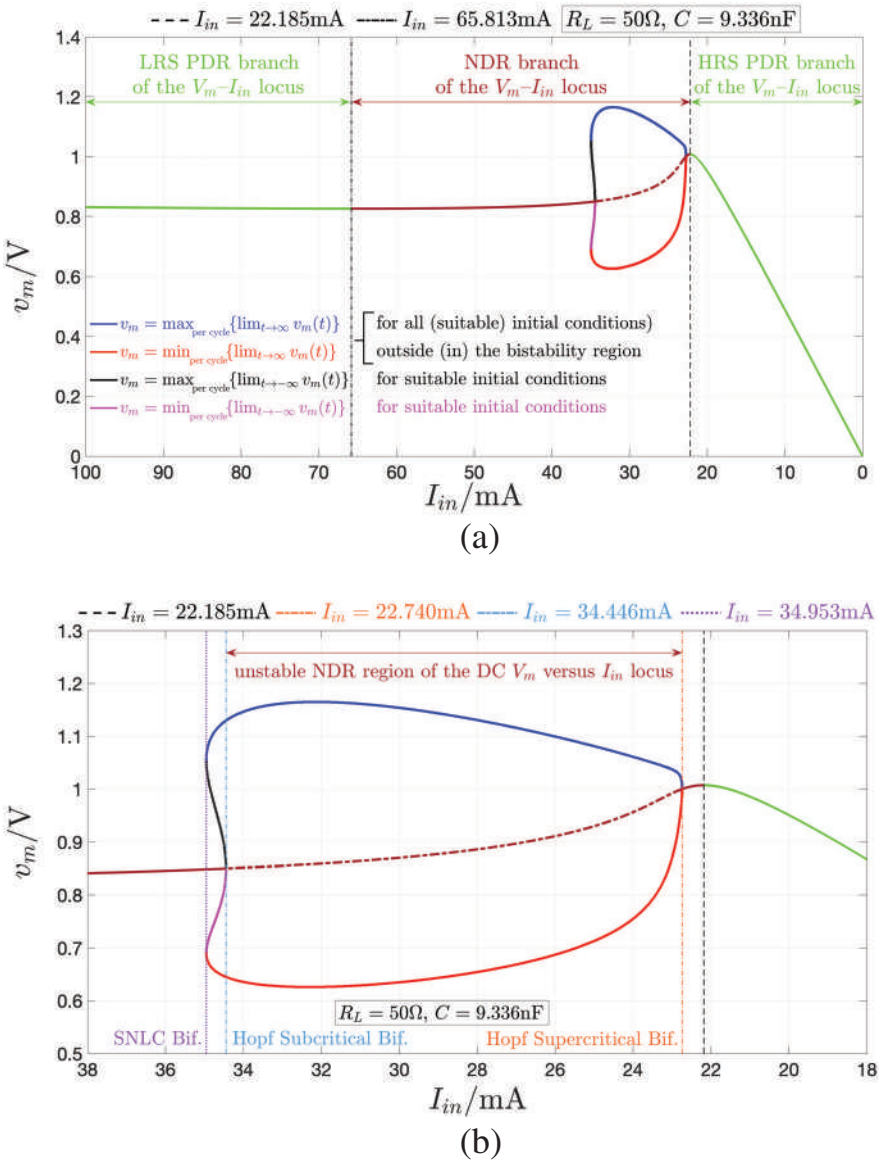

Figure 18. a) Bifurcation diagram of the bio-inspired memristive circuit in Norton form from Figure 2f, illustrating all the admissible stable and unstable quiescent or oscillatory steady-states for the voltage v_m across the memristor under a monotonic change in the DC current stimulus I_{in} across the range [0, 100 mA] for $R_L = 50\ \Omega$ and $C = 9.336$ nF. The curve composed of green and brown branches represents the DC V_m versus I_{in} characteristic of the one-port seen between terminals *A* and *B* in the Norton circuit of Figure 2f. The left and right green branches include LRS and HRS PDR bias points for the one-port, respectively. The one-port NDR bias points lie along the brown branch. A solid (dashed) line-style is used along the V_m versus I_{in} characteristic to indicate stable (unstable) bias points for the one-port. Blue (Red) traces: locus of each maximum (minimum) value $\max_{\text{per cycle}}\{\lim_{t\to\infty} v_m(t)\}$ ($\min_{\text{per cycle}}\{\lim_{t\to\infty} v_m(t)\}$) that the stable steady-state oscillatory solution in the memristor voltage v_m assumes in each cycle asymptotically for any I_{in} value over the range (22.740 mA, 34.446 mA) where the proposed Hodgkin–Huxley neuristor operates in *firing mode*. Black (Magenta) traces: locus of each maximum (minimum) value $\max_{\text{per cycle}}\{\lim_{t\to-\infty} v_m(t)\}$ ($\min_{\text{per cycle}}\{\lim_{t\to-\infty} v_m(t)\}$) that the unstable steady-state oscillatory solution in the memristor voltage v_m assumes asymptotically under reverse-time conditions in each cycle for any I_{in} value over the range (34.446 mA, 34.953 mA) where the proposed Hodgkin–Huxley neuristor may operate either in *firing mode* or in *silent mode* depending upon its initial condition. b) Close-up view of the bifurcation diagram from (a) over the bias current input interval (22 mA, 36 mA), within which the second-order bio-inspired circuit of Figure 2f undergoes the triplet of fundamental bifurcations, which mark the life cycle of an electrical spiking signal across biological axon membranes according to the predictions of the bio-plausible Hodgkin-Huxley neuron model. At the first, second, and third I_{in} value in the set {22.740 mA, 34.446 mA, 34.953 mA} the Norton cell experiences in fact a local Hopf Supercritical Bifurcation, a local Hopf Subcritical Bifurcation, and a Global Saddle-Node Limit Cycle Bifurcation, respectively. Comparing the bifurcation diagram, shown in (a), with the classical Hodgkin-Huxley bifurcation diagram, depicted in Figure 1c, clearly, under a monotonic modulation of the respective input current, the proposed memristive electronic cell from Figure 2f is capable to reproduce qualitatively all the major bifurcation phenomena, occurring in the fourth-order Hodgkin–Huxley neuron model under a progressive unidirectional change in the net synaptic current, while employing half the number of degrees of freedom relative to the mathematical description from the American luminaries. It is in fact the rich analogue dynamics of the NaMLab locally-active memristor that compensates for the relatively low order of the current-driven cell hosting it, allowing a circuit with just two degrees of freedom to mimic the complex behavior of a neuronal system with a 4D state space.

separatrix. For each input current I_{in} across the one-port bistability regime (34.446 mA, 34.953 mA) there exists a point, lying on the black (magenta) trace observable in the bifurcation diagram of Figure 18 at the ordinate associated to the maximum (minimum) value $\max\{\lim_{t\to-\infty} v_m(t)\}$ $(\min\{\lim_{t\to-\infty} v_m(t)\})$, which the memristor voltage $v_m(t)$ assumes over each cycle of the respective GAS periodic waveform as time approaches negative infinity (in practice, transients fade almost completely away over a finite amount of time, here let evolve in the negative direction as a repellor of a dynamic system in forward time becomes an attractor for the same system in reverse time). Plot (b) in Figure 18 shows a close-up view of the bifurcation diagram, shown in plot (a) of the same figure, around the region of the v_m versus I_{in} plane, encompassing the sequence of three bifurcations, which emerge across the Norton circuit one after the other during a forward sweep in the respective current stimulus. Clearly, the proposed Hodgkin-Huxley neuristor of Figure 2f experiences first a Hopf Supercritical Bifurcation when $I_{in} = 22.740$ mA, then a Hopf Subcritical Bifurcation when $I_{in} = 34.446$ mA, and finally a global Saddle-Node Limit Cycle Bifurcation for $I_{in} = 34.953$ mA. It is instructive to point out that, while the bifurcation diagram of the current-driven circuit was acquired upon sweeping the respective bias current input over a positive-valued range, similar conclusions could have been drawn *mutatis mutandis* under a monotonic change of its current stimulus across the negative-valued range (− 100 mA, 0 mA), due to the odd symmetry of the memristor DC I_m versus V_m characteristic. Finally, the bifurcation diagram of the voltage-driven cell of Figure 2e, illustrating all the admissible stable and unstable quiescent or oscillatory steady states for the memristor voltage v_m for each DC input voltage V_{in} across the range (0 V, 5 V) of its forward sweep under the design parameter choice specified via $(R_L, C) = (50\ \Omega, 9.336$ nF) may be easily inferred from the bifurcation diagram, derived above for the equivalent Norton cell and shown in Figure 18a, by scaling the numbers reported along the horizontal axis according to the constraint $V_{in} = R_L \cdot I_{in}$.

6.2.2. Edge of Chaos Behind the Neuronal Bifurcations Emerging in the Cell While It Operates as a Hodgkin–Huxley Neuristor

This section gains a deeper insight into the origin of the neuronal bifurcation phenomena appearing in the Thévenin (Norton) cell for $R_L = 50\ \Omega$ and $C = 9.336$ nF under a monotonic change in the respective DC stimulus. The red (blue) trace in **Figure 19**a shows the evolution of the pole p_- (p_+) of the local impedance $Z_{\mathcal{N}}$ of the cell of Figure 2e,f across the port *A*–*B* under a monotonic build-up in the input voltage (current) V_{in} (I_{in}), which correspondingly brings along concurrently a progressive reduction in the memristor DC voltage V_m and a progressive increase in the memristor DC state $Q = X$, changing as a result the operating point $\mathbf{Q}_{\mathcal{N}} = (Q, V_m)$ about which the linearization analysis is carried out. As better inferable in the close-up view in plot (b) of the same figure, the Thévenin (Norton) cell operates in the instability regime when the DC voltage (current) stimulus V_{in} (I_{in}) lies in the range (1.137 V, 1.722 V) ((22.740 mA, 34.446 mA)), which sets the poles $p_{-Z_{\mathcal{N}}}(\mathbf{Q}_{\mathcal{N}})$ and $p_{+,Z_{\mathcal{N}}}(\mathbf{Q}_{\mathcal{N}})$ somewhere on the RHP. Moreover, as may be evinced from the DC stimulus versus angular frequency diagram of Figure 19c, when under the monotonic DC input voltage (current) modulation, V_{in} (I_{in}) attains a level across the range (1.109 V, 3.291 V) ((22.185 mA, 65.813 mA)) there exists some finite value $\omega_{0,Z_{\mathcal{N}}}(\mathbf{Q}_{\mathcal{N}})$ for ω at which the real part of the local impedance $Z_{\mathcal{N}}$ of the Thévenin (Norton) cell of Figure 2e,f seen across the port *A*–*B* and evaluated about some appropriate operating point $\mathbf{Q}_{\mathcal{N}}$ goes negative. Therefore, combining the results drawn through the analysis of the impact of the DC voltage (current) stimulus on the local stability properties of the operating point $\mathbf{Q}_{\mathcal{N}}$ of the circuit in plot (e,f) of Figure 2 with those collected by testing each DC input voltage (current) V_{in} (I_{in}) for its capability to induce a phase shift larger than $\pi/2$ between any small-signal periodic voltage (current) perturbation δv_{in} (δi_{in}), superimposed on top of its level, and the resulting small-signal periodic current (voltage) response δi_{in} (δv_{in}) in the same Thévenin (Norton) cell, we are in a position to define also the other possible operating regimes, especially the Edge of Chaos Domains but also the Local Passivity Domains, for the voltage-driven (current-driven) circuit in terms of the respective bias stimulus, besides its Unstable Local Activity Domain, defined earlier on, by applying the Local Activity Theorem from Section 2.1 and invoking the Edge of Chaos Corollary from Section 2.2. Figure 19c includes a complete classification of the operating regimes of the Thévenin (Norton) cell in terms of the respective DC voltage (current) stimulus. Interestingly, similarly as is the case for the Hodgkin-Huxley neuron model, either of the two equivalent bio-inspired memristive circuits in plots (e) and (f) of Figure 2 admits two separate Edge of Chaos domains, marked also in the pole diagram of Figure 19. With reference to the horizontal bifurcation path in violet on the *C* versus *Q* diagram of Figure 13a, shown once again in **Figure 20** to facilitate readibility, a progressive increase in the DC voltage (current) stimulus from zero modulates the memristor operating point *Q* in such a way that the cell, poised correspondingly at $\mathbf{Q}_{\mathcal{N}} = (Q, V_m)$, transitions from a first Local Passivity Domain into a first relatively narrow Edge of Chaos Domain, referred to as Edge of Chaos Domain 1, when $V_{in} = 1.109$ V $(I_{in} = 22.185$ mA), moving then into an Unstable Local Activity Domain when $V_{in} = 1.137$ V $(I_{in} = 22.740$ mA), before entering a second relatively wide Edge of Chaos domain, referred to as Edge of Chaos Domain 2, when $V_{in} = 1.722$ V $(I_{in} = 34.446$ mA), to get finally into a second Local Passivity Domain when $V_{in} = 3.291$ V $(I_{in} = 65.813$ mA).

Remark 8. Importantly, increasing V_S (I_{in}) from 0 to 5 V (100 mA), the Thévenin (Norton) circuit topology of the second-order cell from Figure 2e,f undergoes two local Hopf bifurcations, of which the first of Supercritical nature and the second of Subcritical nature, when the voltage (current) stimulus attains in turn the DC levels of 1.137 V (22.740 mA) and 1.722 V (34.446 mA). As indicated through a hollow black circle (hollow black square) in Figure 20, at the Hopf Supercritical (Subcritical) Bifurcation, the memristor operating point *Q* assumes the NDR value of 377 (709), while, correspondingly, either cell is found to be poised at an operating point $\mathbf{Q}_{\mathcal{N}} = (Q, V_m) = (377, 1$ V $(\mathbf{Q}_{\mathcal{N}} = (Q, V_m) = (377, 0.85$ V)) on the frontier between the Edge of Chaos Domain 1 (the Unstable Local Activity Domain) and the Unstable Local Activity Domain (and the Edge of Chaos Domain 2). Moreover, the oscillator from plot (e,f) of Figure 2 is poised on an stable and locally active operating point, specifically $\mathbf{Q}_{\mathcal{N}} = (Q, V_m) = (717, 0.848$ V), which lies on the Edge of Chaos Domain 2, even

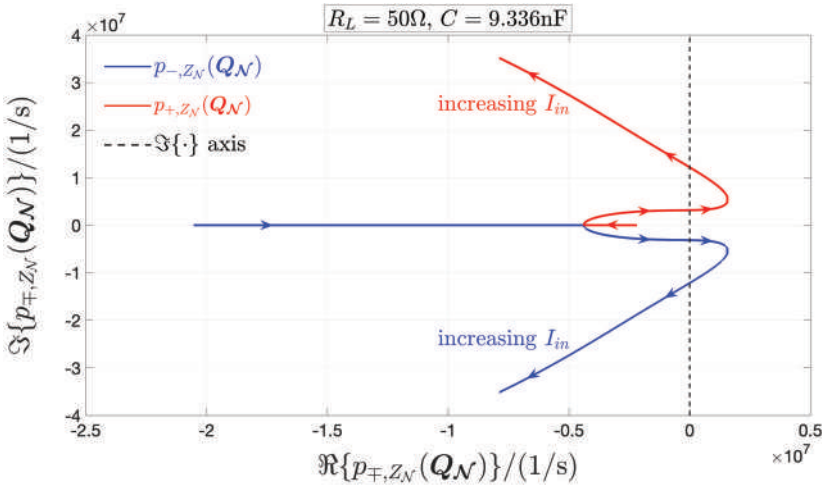

(a)

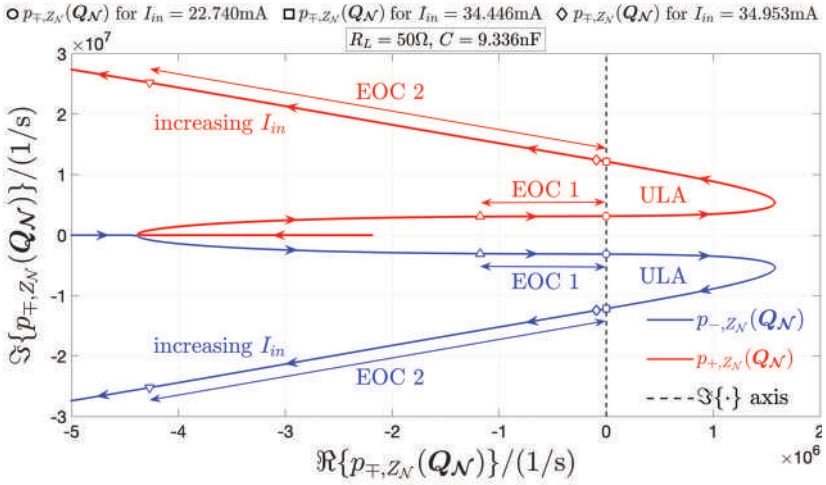

(b)

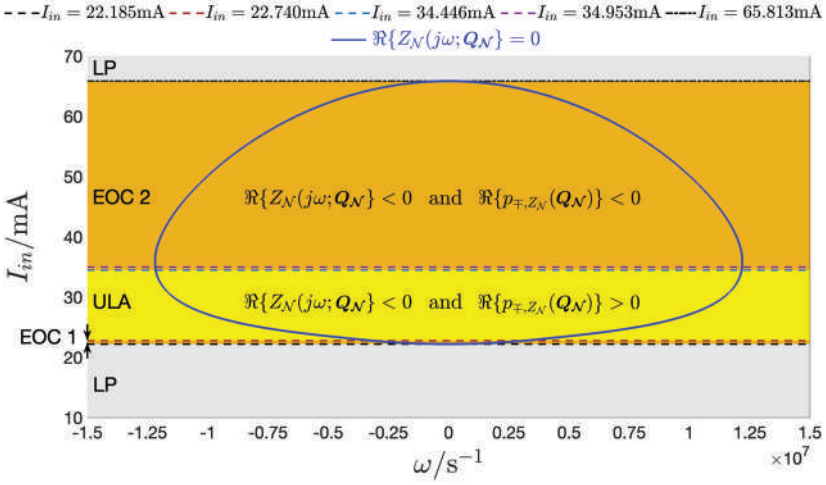

(c)

when it undergoes a global Saddle-Node Limit Cycle Bifurcation for $V_{in} = 1.748$ V ($I_{in} = 34.953$ mA). Last but not least, inspecting Figure 20 once more, and observing that the memristor in either cell is polarized in some operating point Q across the set ($Q_{NDR,\,L}$, $Q_{NDR,\,U}$) = (351, 1006) for each DC voltage (current) stimulus V_{in} (I_{in}) with value in the range (1.109 V, 3.291 V) ((22.185 mA, 65.813 mA)), which includes each of the three control parameter bifurcation thresholds, clearly, the negative differential resistance of the NaMLab memristor has a major impact on the emergence of complex neuronal phenomena across the proposed bio-inspired circuit of Figure 2e,f under monotonic input voltage (current) modulation.

6.2.3. Other Bifurcation Routes of the Bio-Inspired Oscillator Under Monotonic Stimulus Sweep

Before classifying all the bifurcation paths the memristor oscillator may possibly follow under a monotonic modulation in the respective stimulus, the following remark introduces some important definitions.

Remark 9. In the discussion to follow either of the equivalent cells is said to experience *a complementary form of a local Hopf Supercritical bifurcation* if, under monotonic sweep in the respective control parameter, here the DC stimulus, its earlier unstable operating point acquires global stability while concurrently the amplitude of the GAS almost-sinusoidal oscillations, appearing across its capacitance, reduces to zero. Also, either of the two equivalent cells is said to undergo *a complementary form of a local Hopf Subcritical bifurcation* if, under monotonic sweep in the respective control parameter, here the DC stimulus, its earlier stable operating point loses stability while concurrently the amplitude of the almost-sinusoidal unstable oscillations, appearing across its capacitance, reduces to zero. Finally, either of the two equivalent bio-inspired oscillators is said to be subject to *a complementary form of a global Saddle-Node Limit Cycle Bifurcation* if, under monotonic sweep in the respective control parameter, here the DC stimulus, and for suitable initial conditions, a semi-stable large-amplitude nonlinear oscillatory voltage solution, which shall later split into a pair of distinct stable and unstable trains of electrical spikes, is found to suddenly appear across the capacitance at steady state, marking the beginning of a phase,

Figure 19. a) Blue (Red) trace: Locus illustrating how the DC current stimulus of the Norton cell with $R_L = 50\,\Omega$ and $C = 9.336$ nF modulates the location of the pole p_- (p_+) of the local impedance $Z_{\mathcal{N}}$ of the circuit of Figure 2f at the port A–B about the respective I_{in}-dependent operating point $\mathbf{Q}_{\mathcal{N}} = (Q, V_m)$. b) Close-up view of the $\Im\{p_{\mp,Z_{\mathcal{N}}}(\mathbf{Q}_{\mathcal{N}})\}$ versus $\Re\{p_{\mp,Z_{\mathcal{N}}}(\mathbf{Q}_{\mathcal{N}})\}$ loci in (a) around the region of the complex plane where the second-order bio-inspired current-driven memristive oscillator undergoes, under a progressive increase in its DC current stimulus I_{in}, all the three fundamental bifurcations, appearing across neuronal axon membranes under a synaptic current reverse sweep according to the predictions of the bio-plausible Hodgkin–Huxley model. Initially, for each I_{in} value in the set (0 mA, 22.185 mA) the current-controlled relaxation oscillator of Figure 2f is locally passive, since the poles of the local impedance of the cell of Figure 2f across the port A–B about $\mathbf{Q}_{\mathcal{N}}$ lie on the LHP, and concurrently there exists no angular frequency $\omega_{0,Z_{\mathcal{N}}}(\mathbf{Q}_{\mathcal{N}})$ at which the real part of $Z_{\mathcal{N}}(j\omega;\mathbf{Q}_{\mathcal{N}})$ goes negative. However, when I_{in} assumes a value falling in the interval (22.185 mA, 22.740 mA), the inequality $\Re\{Z_{\mathcal{N}}(j\omega;\mathbf{Q}_{\mathcal{N}})\} < 0$ may hold true for some finite angular frequency $\omega_{0,Z_{\mathcal{N}}}(\mathbf{Q}_{\mathcal{N}})$, while at the same time the real parts of $p_{-,Z_{\mathcal{N}}}(\mathbf{Q}_{\mathcal{N}})$ and $p_{+,Z_{\mathcal{N}}}(\mathbf{Q}_{\mathcal{N}})\}$ keep still negative, which sets the cell is the first Edge of Chaos operating regime, referred to here as Edge of Chaos Domain 1. In the ULA domain, i.e. for $I_{in} \in \{22.740\text{ mA}, 34.446\text{ mA}\}$, $p_{-,Z_{\mathcal{N}}}(\mathbf{Q}_{\mathcal{N}})$ and $p_{+,Z_{\mathcal{N}}}(\mathbf{Q}_{\mathcal{N}})$ lie on the RHP. The cell is poised once again on some locally-active and stable operating point $\mathbf{Q}_{\mathcal{N}}$ when its bias current stimulus I_{in} falls in the range {34.446 mA, 65.813 mA}, which defines the second Edge of Chaos operating regime, referred to here as Edge of Chaos Domain 2. Finally, for each bias input current I_{in} beyond 65.813 mA, the Hodgkin–Huxley cell of Figure Figure 2f returns to its initial locally passive state. The hollow circle (square) markers identify the locations of the poles p_- and p_+ of the cell local impedance $Z_{\mathcal{N}}$ about the operating point $\mathbf{Q}_{\mathcal{N}} = (Q, V_m) = (377.466, 1\,\text{V})$ ($\mathbf{Q}_{\mathcal{N}} = (Q, V_m) = (708.836, 0.850\,\text{V})$), i.e., at the local Supercritical (Subcritical) Hopf Bifurcation, when I_{in} attains the value of 22.740 mA (34.446 mA). In the first (latter) case the Hodgkin–Huxley neuristor of Figure 2f transitions from the EOC 1 domain (ULA domain) to the ULA domain (EOC 2 domain). While operating in the EOC Domain 2, the neuristor experiences a global Saddle-Node Limit Cycle Bifurcation, when its bias input current I_{in} grows up to the value 34.953 mA, which endows it with the operating point $\mathbf{Q}_{\mathcal{N}} = (Q, V_m) = (716.808, 0.848\,\text{V})$ (the hollow diamond markers indicate the locations of the poles $p_{-,Z_{\mathcal{N}}}(\mathbf{Q}_{\mathcal{N}})$ and $p_{+,Z_{\mathcal{N}}}(\mathbf{Q}_{\mathcal{N}})$ on the complex plane here). Last, hollow upper-pointing (hollow downward-pointing) triangles are used to mark the locations of these poles when the current-driven bio-inspired cell enters (leaves) the EOC domain 1 (the Edge of Chaos domain 2), which is the case when I_{in} attains the value of 22.185 mA (65.813 mA). c) Partition of the DC input current I_{in} versus angular frequency ω plane into different operating domains for the second-order bio-inspired current-driven cell of Figure 2f with $R_L = 50\,\Omega$ and $C = 9.336$ nF. The grey regions indicate the Local Passivity (LP) domains. In the bottom (top) part, identifiable across the vertical axis range (0 mA, 22.185 mA) ((65.813 mA, 70 mA)), any bias input current I_{in} poises the cell memristor in some HRS (LRS) PDR bias point along its DC V_m versus I_m characteristic, while, concurrently, no condition of the Local Activity Theorem from Section 2.1 holds true for the cell local impedance $Z_{\mathcal{N}}(s)$ across the port A–B about the respective I_{in}-dependent operating point $\mathbf{Q}_{\mathcal{N}} = (Q, V_m)$. The yellow region (Each of the two separate ochre regions) represents the Unstable Local Activity (ULA) (an Edge of Chaos) domain. In either case any bias input current I_{in} stabilizes the cell threshold switch at some NDR bias point, lying along the negative-slope branch of its DC V_m versus I_m characteristic, and endowing it correspondingly with an operating point Q falling in the range ($Q_{NDR,\,L}$, $Q_{NDR,\,U}$). However, for any DC current stimulus I_{in} associated to the yellow region, and thus ranging across the interval (22.740 mA, 34.446 mA), condition (i) of the Local Activity Theorem from Section 2.1 is found to hold true for the cell local impedance $Z_{\mathcal{N}}(s)$ across the port A–B about the respective operating point $\mathbf{Q}_{\mathcal{N}}$. In fact, for any I_{in} in the yellow region the poles of $Z_{\mathcal{N}}(s)$ about the respective operating point $\mathbf{Q}_{\mathcal{N}}$ form a complex conjugate pole pair with positive real part. Thus, the fact that condition (iv) of the Local Activity Theorem may be additionally satisfied in the yellow region, being $\Re\{Z_{\mathcal{N}}(j\omega;\mathbf{Q}_{\mathcal{N}})\}$ negative within the yellow sub-region enclosed within the blue closed curve, denoting the locus, where the real part of the cell local impedance is identically null, is irrelevant here. On the other hand, any DC input current I_{in} across the lower (upper) ochre region, defining the EOC Domain 1 (the EOC Domain 2), EOC 1(EOC 2) for short, and ranging across the interval (22.185 mA, 22.740 mA) ((34.446 mA, 65.813 mA)) sets the current-driven memristive circuit of Figure 2(f) on a stable and locally-active operating point $\mathbf{Q}_{\mathcal{N}}$, at which both conditions (j) and (jj) of the Edge of Chaos Corollary from Section 2.2) apply. In fact, for any I_{in} in the ochre regions the cell local impedance $Z_{\mathcal{N}}(s)$ about the respective operating point $\mathbf{Q}_{\mathcal{N}}$ admits a pair of complex conjugate poles lying on the LHP, featuring furthermore a negative real part for $s = j\omega$ within the angular frequency range $(-\omega_{0,Z_{\mathcal{N}}}(\mathbf{Q}_{\mathcal{N}}), \omega_{0,Z_{\mathcal{N}}}(\mathbf{Q}_{\mathcal{N}}))$ specified via Equation (55), where $-(+)\omega_{0,Z_{\mathcal{N}}}(\mathbf{Q}_{\mathcal{N}})$ is identifiable graphically as the abscissa of the left (right) intersection between the linear segment stretching out horizontally at height I_{in} and the blue closed curve including each point (ω, I_{in}) where $\Re\{Z(j\omega, \mathbf{Q}_{\mathcal{N}})\}$ vanishes.

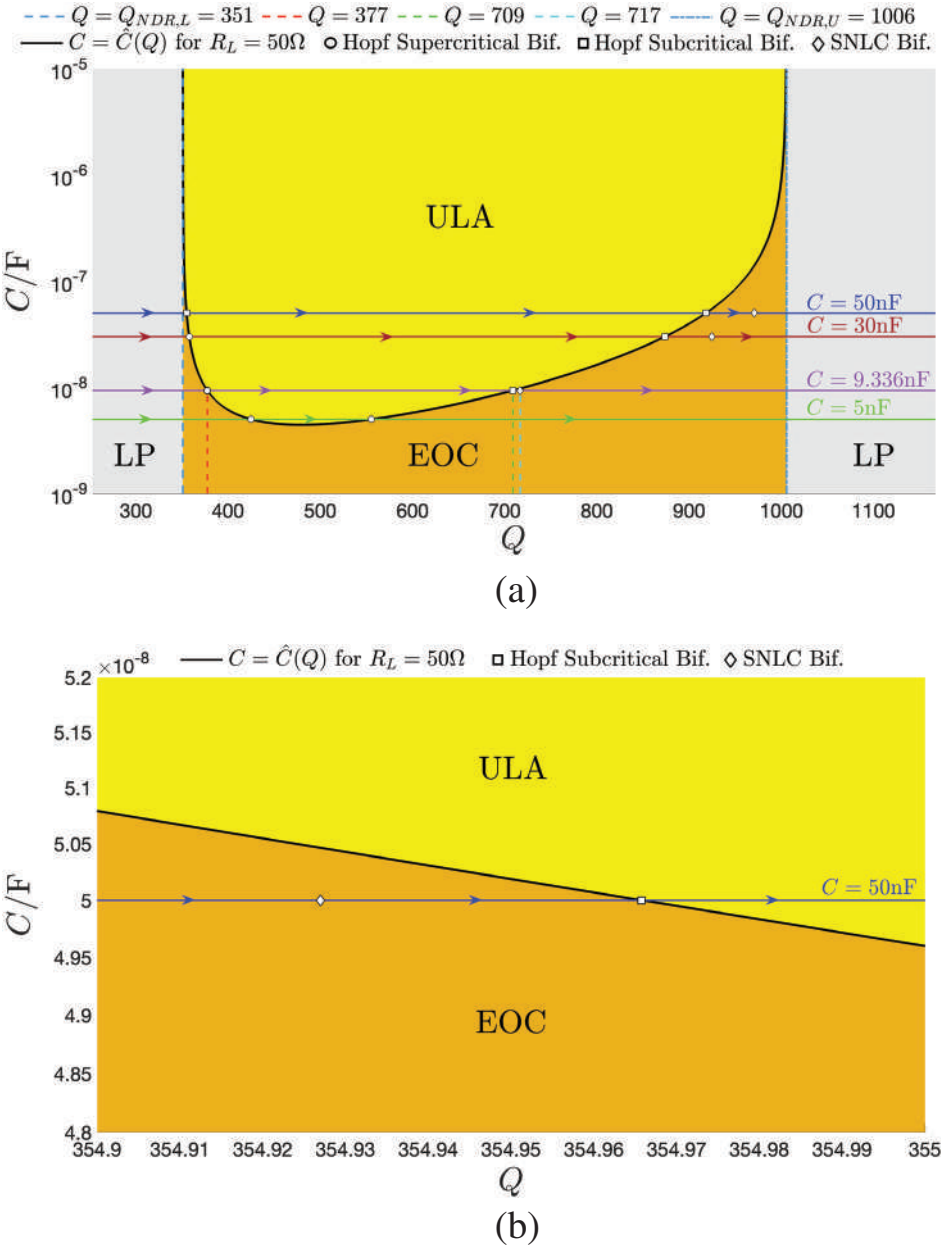

Figure 20. a) C versus Q diagram showing how the operating regime of the bio-inspired circuit in plot (e,f) of Figure 2 may be modulated for $R_L = 50\ \Omega$ through the other possible control parameter of interest, i.e., the DC voltage (current) stimulus V_{in} (I_{in}), after choosing a value for the other one, i.e., the capacitance C. The black trace indicates the locus of points where either cell is subject to a local Hopf Bifurcation. Three are the bifurcation routes which the Thévenin (Norton) cell may undergo under input voltage (current) forward sweep. For relatively low capacitance values, either cell experiences two complementary local Hopf Subcritical bifurcations in complementary form (in the remainder of this paper two bifurcations of the same kind, emerging one after the other across a physical system under a monotonic change in one of its control parameters, are said to be complementary one relative to the other when the nonlinear dynamics of the system to the left (right) of the critical point, where one of the two bifurcations occurs, is analogous to the nonlinear dynamics of the same system to the right (left) of the critical point, where the other bifurcation occurs). This is the case for example for $C = 5$ nF, when as its DC stimulus is progressively increased the (Q, C) point travels rightward along the horizontal green path. For relatively moderate capacitance values, increasing progressively the DC input voltage (current) V_{in} (I_{in}) from zero, the circuit of Figure 2e,f operates as a Hodgkin–Huxley neuristor, undergoing one after the other the three dramatic events, specifically a first local Hopf Supercritical Bifurcation, a second local Hopf Subcritical Bifurcation, and a third global Saddle-Node Limit Cycle Bifurcation, determining generation, evolution and extinction of a train of electrical spikes across biological axon membranes. This is the case for example for $C = 9.336$ nF or for $C = 30$nF, when as its DC stimulus is progressively increased the (Q, C) point travels rightward along the horizontal violet and brown paths, respectively. Here, during the DC voltage (current) sweep across the circuit of Figure 2e,f, the memristor bias point **P** may visit HRS or LRS PDR branches of the I_m (V_m) versus V_m (I_m) characteristic. Under these voltage (current) stimulation conditions, irrespective of the capacitance value, the cell is locally stable yet merely locally passive (LP) about the corresponding operating point $\mathbf{Q}_{\mathcal{N}}$, and may thus only relax toward a quiescent steady state, after transients decay to zero. Only while the DC voltage (current) stimulus endows the NaMLab threshold switch with a negative differential resistance, may the bio-inspired voltage-driven (current-driven) cell in plot (e,f) of Figure 2

where the cell itself exhibits bistable behavior after transients fade away.

As discussed in the description of Figure 13a, depending upon the DC stimulus V_{in} (I_{in}), the Thévenin (Norton) cell may experience one of two admissible bifurcation routes under forward capacitance sweep. Interestingly, the nonlinear dynamics of either cell is richer when the respective DC stimulus is taken as bifurcation parameter. Particularly, as anticipated earlier, depending upon the value assigned to the capacitance C, the memristive relaxation oscillator of Figure 2e,f) may follow one of three possible bifurcation paths under a monotonic change in the respective bias input voltage (current) V_{in} (I_{in}), as listed and described below.

(i) For relatively low values of the capacitance the bio-inspired cell of Figure 2e,f) undergoes a sequence of complementary Local Hopf Supercritical Bifurcations, which explain the bubble shape of the respective v_m versus V_{in} (I_{in}) bifurcation diagram, under a monotonic increase in the input voltage (current). For example, referring to the horizontal green bifurcation path in the diagram from Figure 20a, for $C = 5$ nF as the DC stimulus is progressively increased, the Thévenin (Norton) cell first admits a GAS operating point. It then undergoes a first local Hopf Supercritical Bifurcation, which destabilizes its operating point while spawning an infinitesimally-small GAS limit cycle around it on the v_m versus x phase plane, when V_{in} (I_{in}) is increased up to 1.178 V (=23.569 mA), which endows the threshold switch with the NDR operating point $Q = 424.825$. Subsequently the amplitude of the limit cycle grows up to a maximum value before decreasing thereafter, reducing eventually to zero at a second local Hopf Supercritical Bifurcation, which, complementarily to the first one, turns off the unique asymptotic oscillatory solution for the voltage across the memristor, while restoring a quiescent mono-stable steady-state behavior for the cell, when the DC input voltage (current) V_{in} (I_{in}) attains the value of 1.351 V (27.015 mA), poising the memristor on the NDR operating point $Q = 555.449$. **Figure 21a** illustrates all the possible stable and unstable quiescent and oscillatory steady states of the memristor voltage in the Norton cell under DC input current forward sweep in this scenario. A close-up view of this bubble-shaped bifurcation diagram in the region of the v_m versus I_{in} plane, enclosing the two Hopf Supercritical bifurcations, is shown in plot (b) of the same figure.

(ii) For relatively moderate values of the capacitance a progressive increase in V_{in} (I_{in}) induces the emergence of the three-bifurcation cascade, marking the life cycle of an Action Potential in biological axon membranes under synaptic current reverse sweep, as predicted by Hodgkin and Huxley in 1952, across the Thévenin (Norton) cell, which then operates effectively as a Hodgkin–Huxley neuristor For example, referring to the horizontal violet bifurcation path in the diagram from Figure 20a, for $C = 9.336$ nF the first (latter) cell undergoes a Local Hopf Supercritical Bifurcation, a Local Hopf Subcritical Bifurcation, and a global Saddle-Node Limit Cycle Bifurcation when V_{in} (I_{in}) respectively attains the values of 1.137 V (22.740 mA), 1.722 V (34.446 mA), and 1.748 V (34.953 mA), which in turn endows its memristor with a NDR operating point Q of values increasing progressively from the first to the third in the set {377.466, 708.836, 716.808}, as indicated through a hollow black circle, a hollow black square, and a hollow black diamond along the horizontal line $C = 9.336$ nF (recall the illustration of all the possible stable and unstable quiescent and oscillatory steady states of the memristor voltage in the Norton cell under DC input current forward sweep from Figure 18). As other example, following the horizontal brown bifurcation route in the diagram from Figure 20a, for $C = 30$ nF the voltage-driven (current-driven) circuit experiences a Local Hopf Supercritical Bifurcation, a Local Hopf Subcritical Bifurcation, and a global Saddle-Node Limit Cycle Bifurcation when V_{in} (I_{in}) respectively attains the values of 1.117 V (22.350 mA), 2.409 V (48.182 mA), and 2.706 V (54.128 mA), which in turn endows its memristor with a NDR operating point Q of values increasing progressively from the first to the third in the set {357.859, 873.682, 924.610}, as indicated through a hollow black circle, a hollow black square, and a hollow black diamond along the horizontal line $C = 30$nF. Figure 21c shows all the possible stable and unstable quiescent and oscillatory steady states of the memristor voltage in the Norton cell under DC input current forward sweep in this scenario. Plot (d) in the same figure shows a zoom-in view of this bifurcation diagram in the area hosting the three neuronal bifurcations. Magnifying further the scale of this plot in the region of the first bifurcation results in plot (e), which clearly reveals its local Hopf supercritical nature. Finally, the blue (red) trace in Figure 21f depicts the steady-state time waveform of the memristor voltage v_m (state x) when the DC voltage (current) stimulus V_{in} I_{in} in the Thévenin (Norton) cell is set to a post-Hopf-supercritical bifurcation value, specifically 1.15 V (23 mA).

(iii) For relatively large values of the capacitance, under a monotonic increase in the respective bias voltage (current) stimulus the relaxation oscillator of Figure 2e,f is found to

reproduce the complex neuronal phenomena emerging across a biological axon membrane under monotonic synaptic current modulation according to the Hodgkin–Huxley model predictions. Notably, as explained in detail in Section 6.2.2, the two local Hopf bifurcations occur under DC voltage (current) sweep while the bio-inspired oscillator, shown in the first (latter) plot, is poised on the Edge of Chaos about the respective operating point, similarly as it happens for the Hodgkin–Huxley neuron model (refer to Figure 10b in Section S2 of the Supporting Information file). Interestingly either cell is poised on the Edge of Chaos about the respective operating point also while experiencing the global bifurcation, later on. For relatively large capacitance values, the bio-inspired voltage-driven (current-driven) memristive circuit is subject to a four-bifurcation cascade, in which the first sequence, where a local Hopf Subcritical Bifurcation anticipates a global Saddle-Node Limit Cycle Bifurcation, is followed by a second sequence, composed of the very same bifurcations, included in the first sequence, appearing however in the opposite order and in their complementary forms. This is the case for example for $C = 50$ nF, when as its DC stimulus is progressively increased the (Q, C) point travels rightward along the horizontal blue path. b) Close-up view of the C versus Q diagram in the region where for $R_L = 50\ \Omega$ and $C = 50$ nF the second-order Thévenin (Norton) cell undergoes the first pair of bifurcations, specifically a Saddle-Node Limit Cycle Bifurcation followed by a Hopf Subcritical bifurcation.

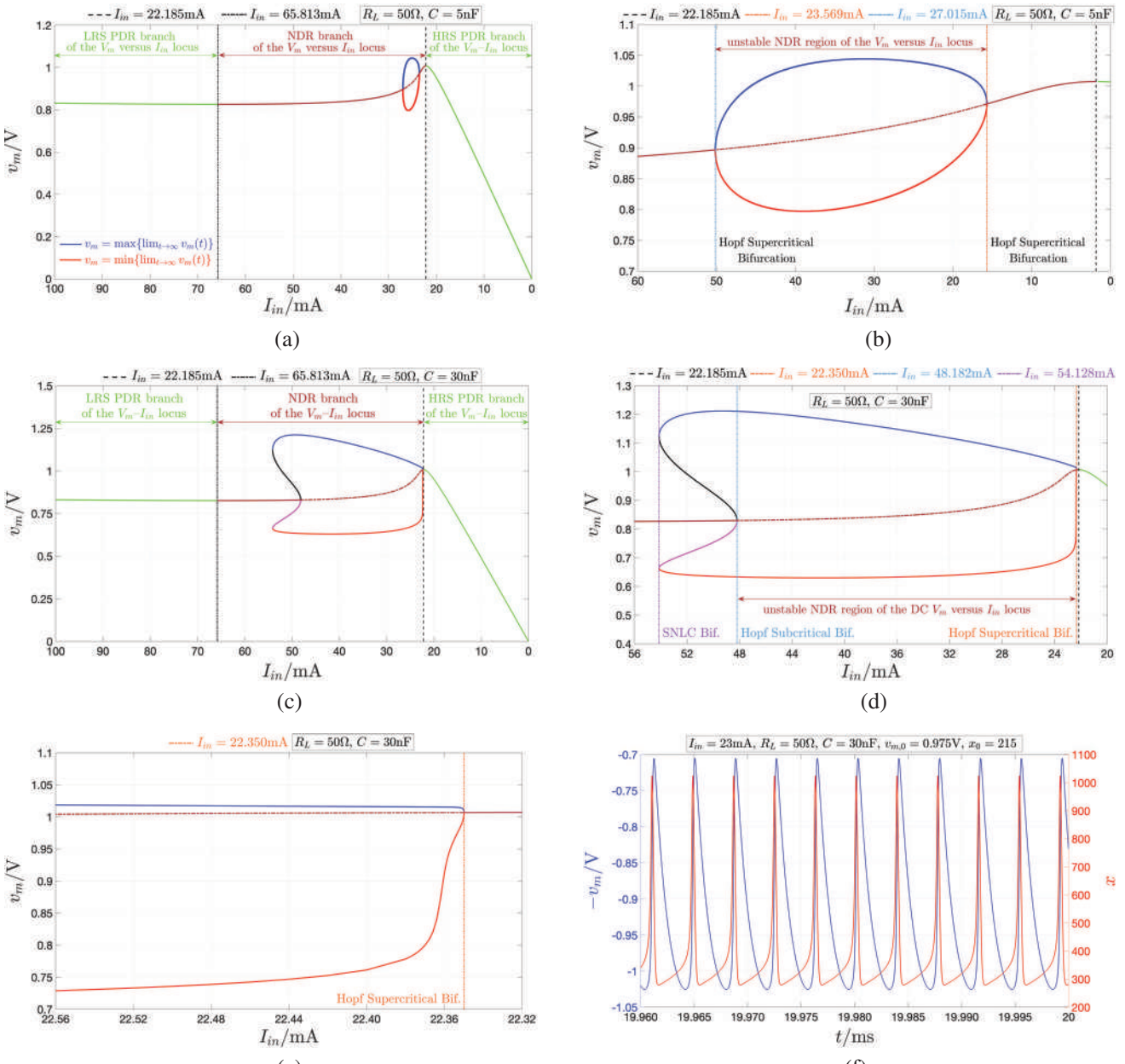

Figure 21. a) Bifurcation diagram of the current-driven relaxation oscillator of Figure 2f for $R_L = 50\ \Omega$ and $C = 5$ nF on the ν_m versus I_{in} plane. b) Zoom-in view of the bubble-shaped bifurcation diagram in (a) around the region of the ν_m versus I_{in} plane hosting the two complementary local Hopf Supercritical Bifurcations. As I_{in} increases from 0 mA to 100 mA, the Norton cell undergoes the first (second) Hopf bifurcation when I_{in} attains the value of 23.569 mA (27.015 mA). c) Bifurcation diagram of the Norton cell of Figure 2f for $R_L = 50\ \Omega$ and $C = 30$ nF on the ν_m versus I_{in} plane. Clearly, in this scenario the cell qualitatively reproduces the classical bifurcation diagram of the Hodgkin–Huxley neuron model. d) Zoom-in view of the diagram, shown in plot (c), around the area enclosing the three-bifurcation cascade, which marks the most important phases in the life cycle of an Action Potential across biological axon membranes, as predicted by the model from Hodgkin and Huxley. e) Close-up view of the ν_m versus I_{in} locus from plot (d) in the region of the first bifurcation the Norton cell goes through as the respective DC stimulus is progressively increased from zero. This plot clearly reveals the local Hopf Supercritical type of this bifurcation. g) Bifurcation diagram of the current-driven relaxation oscillator of Figure 2f for $R_L = 50\ \Omega$ and $C = 50$ nF on the ν_m versus I_{in} plane. At $I_{in} = 22.1849$ mA ($I_{in} = 65.8130$ mA) the memristor bias point lies at the frontiers between the HRS PDR (NDR) and the NDR (LRS PDR) branches of the I_m versus V_m characteristic. h) Close-up view of the bifurcation diagram from plot (g) across the I_{in} range, including the Saddle-Node Limit Cycle-Hopf Subcritical Bifurcation cascade. i) Magnification of the region of the bifurcation diagram from plot (h) around the region, hosting the unstable steady-state oscillatory solution for the memristor voltage, covering the DC input current range (22.28279 mA, 22.28370 mA), starting off (ending up) with the global Saddle-Node Limit Cycle (the local Hopf Subcritical) bifurcation point, and defining the first bi-stability regime for the Norton cell. j) Zoom-in image of the ν_m versus I_{in} locus from plot (g) over the DC input current interval (53.31780 mA, 60.40787 mA), within which the current-driven cell admits a second bi-stability regime. When I_{in} attains the left (right) bound in this range, the Norton cell undergoes a second local Hopf Subcritical (a second global Saddle-Node Limit Cycle) bifurcation complementary to the first one.

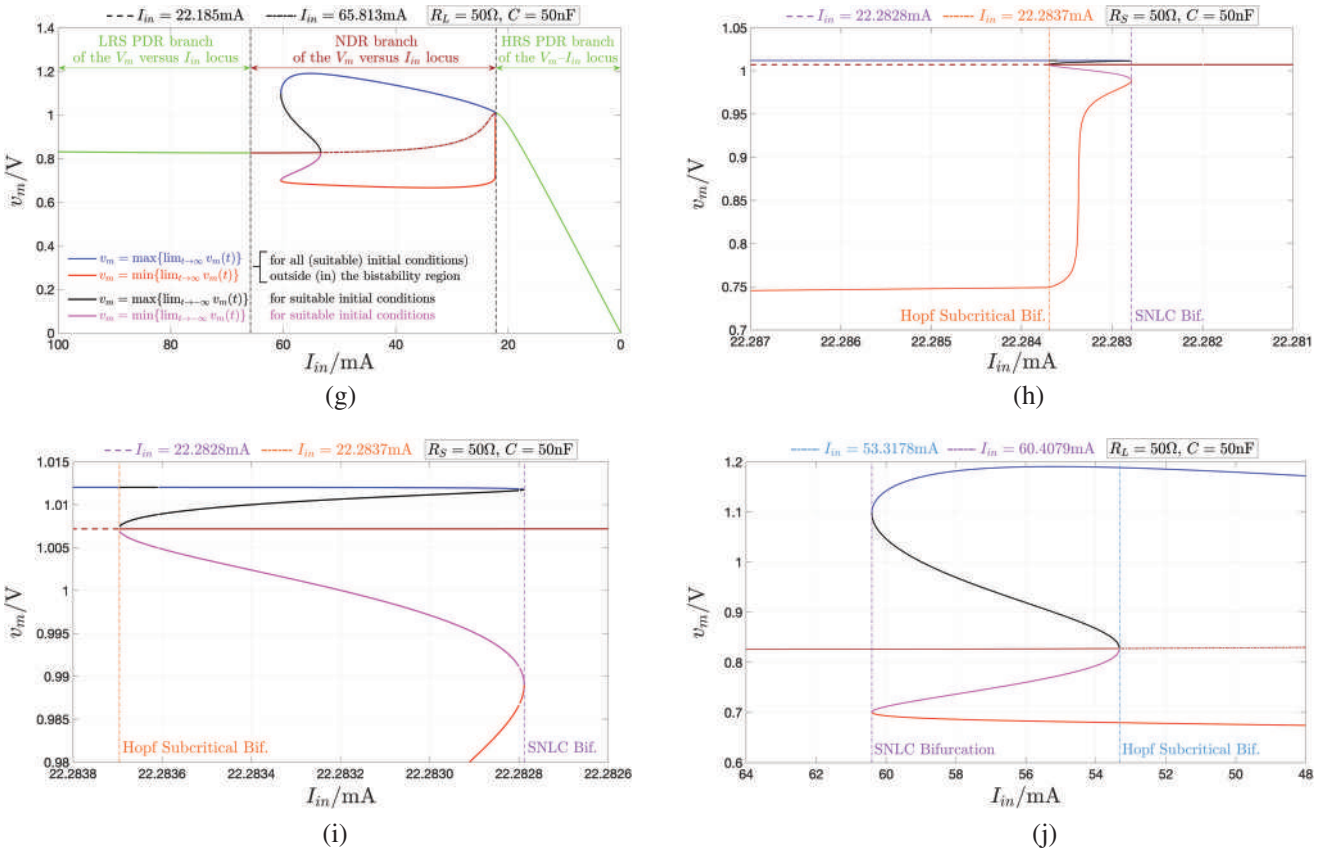

Figure 21. *Continued*

experience a four-bifurcation cascade, in which the bifurcations in the left pair, including first a global Saddle-Node Limit Cycle Bifurcation and then a local Hopf Subcritical Bifurcation, appear in the opposite order and complementary form in the right pair. For example, referring to the horizontal blue bifurcation path in the diagram of Figure 20a and well as to the close-up view of the same diagram in the region of the C versus Q plane, where the horizontal blue path itself crosses the frontier between the Edge of Chaos domain and the Unstable Local Activity domain from left to right, as shown in Figure 20(b), for $C = 50$ nF the first (latter) memristive circuit first exhibits a monostable quiescent steady-state behavior. The Thévenin (Norton) cell experiences then a first global Saddle-Node Limit Cycle Bifurcation, at which a relatively large semi-stable saddle-node limit cycle suddenly appears on the v_m versus x phase plane around the respective operating point $\mathbf{Q}_{\mathcal{N}}$, which concurrently keep stable, yet in a local sense only, when V_{in} (I_{in}) rises up to 1.11414 V (22.28279 mA), which stabilizes the NaMLab thereshold switch on the NDR operating point $Q = 354.927$. Directly afterwards, the saddle-node limit cycle splits into two separate limit cycles, of which the smaller one is found to be unstable, and to separate the basins of attraction of the two possible locally-stable steady-states for the phase-plane trajectories, specifically an operating point, lying inside it, and the larger cycle within which it is entirely enclosed. With the Thévenin (Norton) cell operating a a bi-stable dynamic system, increasing the DC voltage (current) stimulus further, the amplitude of the unstable limit cycle undergoes a progressive reduction until a first local Hopf Subcritical Bifurcation, occurring for $V_{in} = 1.11418$ V ($I_{in} = 22.28370$ mA), when, with the memristor poised on the NDR operating point $Q = 354.966$, it decreases to zero, resulting in the suppression of the unstable oscillatory solution for the memristor voltage, and in the destabilization of its quiescent level, which leaves one one and only one attractor, specifically the remaining limit cycle, now acquiring a global form of stability, in the memristor voltage versus memristor state phase plane. Subsequently, when V_{in} (I_{in}) is increased up to the value of 2.66589 V (53.31780 mA), which sets the memristor at the operating point $Q = 918.136$, the voltage-driven (current-driven) cell of Figure 2(e) (2(f)) experiences yet another local Hopf Subcritical Bifurcation, which, complementarily to the first one, restores the stability of its operating point, spawning the birth of an infinitesimally-small semi-stable limit cycle around it, which endows the Thévenin (Norton) cell with two initial condition-dependent coexisting steady-state behaviors of quiescent and oscillatory form, respectively. Thereafter, the semi-stable limit cycle splits into two separate limit cycles of which the inner one, encircling the operating point, is found to be unstable, to lie entirely within the outer one, which on the other hand

features a stable nature, and to separate the sets of initial conditions, from which the trajectory solutions approach the two possible attractors of the state vector on the phase plane. As the forward input voltage (current) sweep proceeds, the inner unstable cycle grows progressively till the point, where V_{in} (I_{in}) attains the value of 3.02039 V (60.40787 mA), which biases the NaMLab threshold switch at the operating point $Q = 970.726$ when, due to a second global Saddle-Node Limit Cycle Bifurcation, complementary to the first one, it merges gently with the outer stable cycle, forming yet another semi-stable limit cycle, which disappears from the v_m versus x plane as soon as the control parameter passes over the aforegiven threshold, restoring a monostable quiescent steady-state for the memristor voltage in the Thévenin (Norton) circuit of Figure 2e,f thereafter. Figure 21g displays the entire bifurcation diagram of the Norton cell under DC input current forward sweep in this scenario. Plot (h) in the same figure shows a zoom-in view of this diagram in the region of the v_m versus I_{in} plane hosting the first two bifurcations. The first saddle-node limit cycle (second Hopf subcritical) bifurcation in this pair, occurring for $I_{in} = 22.28279$ mA ($I_{in} = 22.28370$ mA), marks the beginning (end) of the first bi-stable operating regime for the Norton cell. Plot (i) is the result of a magnification of the area, belonging to plot (h), which encloses the unstable steady-state oscillatory solution for the memristor voltage. A close-up view of the diagram from Figure 21g in the area enclosing the last two bifurcations is illustrated on the other hand in plot (j) of the same figure. The first Hopf subcritical (second saddle-node limit cycle) bifurcation in this pair, occurring for $I_{in} = 53.31780$ mA ($I_{in} = 60.40787$ mA), marks the beginning (end) of the second bi-stable operating regime for the Norton cell.

Importantly, irrespective of the capacitance value, either of the two equivalent second-order bio-inspired cells is poised on the Edge of Chaos when it experiences any of the bifurcations which crucially determine its local and global nonlinear dynamics under a monotonic change in the respective DC stimulus.

7. High-Order Neuristors

Bio-inspired neuristor structures, employing a larger number of dynamic circuit elements, need to be employed to capture higher-order neuronal phenomena. For example, as already described in ref. [28], the fourth-order circuit topology, shown in **Figure 22a**, and composed of two different copies of the Hodgkin–Huxley neuristor, presented in this manuscript, is necessary to reproduce various complex neuronal spiking patterns. Applying circuit-theoretic principles to this fourth-order circuit, employing two identical NbO_x threshold switches, one per Hodgkin–Huxley neuristor cell, its ODE set is found to be expressed by

$$\dot{x}_1 = g(x_1, v_{m,1}) \tag{60}$$

$$\dot{v}_{C,1} = \frac{1}{C_1} \cdot \left(i_{in} - G_1 \cdot v_{C,1} - G(x_1) \cdot (v_{C,1} - V_1) - \frac{v_{C,1} - v_{C,2}}{R_C} \right) \tag{61}$$

$$\dot{x}_2 = g(x_2, v_{m,2}), \text{and} \tag{62}$$

Table 3. Values assigned to the circuit parameters of the fourth-order neuristor from Figure 22a to induce the emergence of three distinct biomimetic spike trains at its output node after transients decay to zero. Only the capacitances need to be tuned to lock the neuristor into a different oscillatory operating mode.

Regular spiking						
V_1	R_1	C_1	R_C	V_2	C_2	R_2
−1 V	50 Ω	500 nF	18 Ω	1 V	75 nF	50 Ω
Chattering						
V_1	R_1	C_1	R_C	V_2	C_2	R_2
−1 V	50 Ω	500 nF	18 Ω	1 V	30 nF	50 Ω
Fast spiking						
V_1	R_1	C_1	R_C	V_2	C_2	R_2
−1 V	50 Ω	180 nF	18 Ω	1 V	30 nF	50 Ω

$$\dot{v}_{C,2} = \frac{1}{C_2} \cdot \left(-G_2 \cdot v_{C,2} - G(x_2) \cdot (v_{C,2} - V_2) + \frac{v_{C,1} - v_{C,2}}{R_C} \right) \tag{63}$$

where i_{in} is the input current, while, for each i value in {1, 2}, x_i and $v_{C,i}$ denote the state of the i^{th} memristor $\mathcal{M}_i$ and the voltage across the i^{th} capacitor C_i, respectively. Importantly, $g(x_i, v_{m,i})$ and $G(x_i)$ respectively represent the state evolution function and the memductance function of the i^{th} memristor, according to the NaMLab memristor model[19] (recall in turn Equations (11) and (12) with $v_{m,i} = v_{C,i} - V_i$ standing for the voltage drop across the i^{th} threshold switch, appearing in series with a DC voltage source named V_i, whereas $G_i \triangleq R_i^{-1}$ ($i \in \{1, 2\}$). For simplicity the two threshold switches are assumed to be identical, thus the very same parameter set, as provided in Table 1, is assigned to the NaMLab memristor model employed to describe each of them. Setting values for the linear circuit parameters, as reported in the top, middle, and bottom parts of **Table 3**, and perturbing the fourth-order circuit through a current source i_{in}, generating a Heaviside step function of time with amplitude $I_{in} = 13$ μA and center around $t = 0.2$ms, the output signal v_{out}, coinciding with the voltage v_{C_2}, falling across the capacitance C_2, is found to experience regular spiking, chattering, and fast spiking at steady state, a depicted in plots (c), (d), and (e) of Figure 22, respectively.

As first reported in ref. [28], the fourth-order neuristor topology needs to be augmented with another dynamic element, specifically a capacitor, here called C_{in}, as shown in Figure 22b, in order to reproduce the *All-or-None* neuronal effect. This fifth-order circuit is modeled via the ODE set

$$\dot{x}_1 = g(x_1, v_{m,1}) \tag{64}$$

$$\dot{v}_{C,1} = \frac{1}{C_1} \cdot \left(\frac{v_{in} - v_{C_{in}} - v_{C_1}}{R_0} - G_1 \cdot v_{C,1} - G(x_1) \cdot v_{m,1} - \frac{v_{C,1} - v_{C,2}}{R_C} \right) \tag{65}$$

$$\dot{x}_2 = g(x_2, v_{m,2}) \tag{66}$$

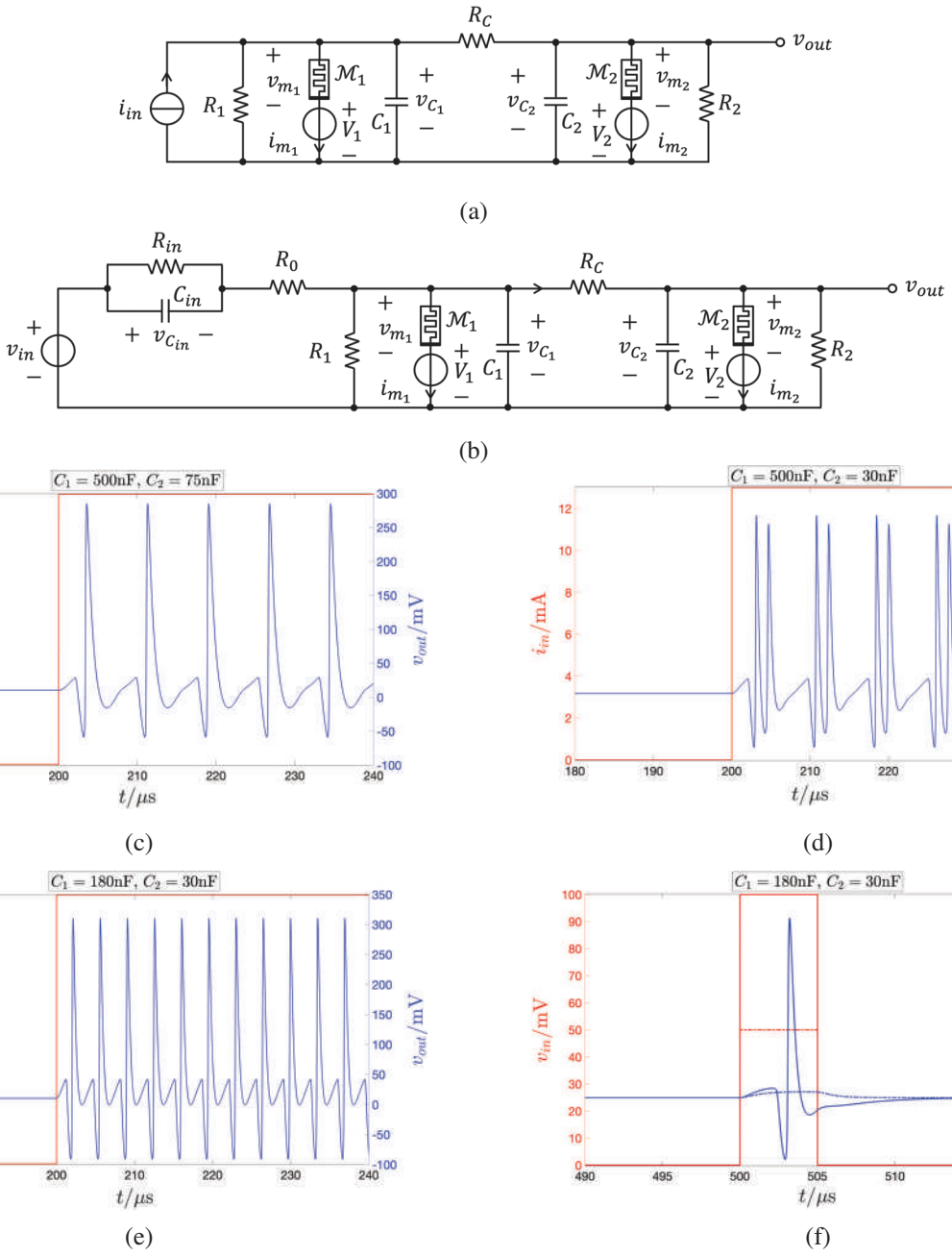

Figure 22. a) A fourth-order neuristor leveraging the local activity of a couple of NaMLab NbO_x threshold switches and a pair of linear capacitors for supporting high-order neuronal phenomena. b) A fifth-order neuristor requiring an additional capacitance, relative to the circuit configuration in (a), for reproducing conditional gain in neuronal axon membranes. c–e) Regular spiking (c), chattering (d), and fast spiking (e) in the fourth-order neuristor structure from plot (a). The circuit, composed of two different copies of the proposed Hodgkin–Huxley neuristor cell, employs two identical locally-active memristors, for each of which we employ the mathematical description (9)–(10) of the NaMLab NbO_x threshold switch with parameter setting from Table 1. Table 3 provides the values for the parameters of the linear circuit elements for each of the three simulation results. In all cases the vector $(x_{1,0}, \nu_{C_1,0}, x_{2,0}, \nu_{C_2,0}) \triangleq (x_1(0), \nu_{C_1}(0), x_2(0), \nu_{C_2}(0))$ of the initial conditions was fixed to (711, 0.1 V, 709, 0.1 V). The input current i_{in} is a unit step function of time, featuring an amplitude I_{in} of 13 μA and centered at $t = 0.2$ms. f) Appearance of the All-or-None phenomenon in the fifth-order Hodgkin–Huxley neuristor from plot (b). Applying a brief $\Delta T = 0.5$ μs-long rectangular voltage pulse to the input node, and setting its amplitude V_{in} to a sub-threshold (supra-threshold) value, specifically 50 mV (100 mV, as shown by the dash-dotted (solid) red trace, the circuit attenuates (amplifies) the stimulus, as may be observed at the output node, where the voltage ν_{out} is found to undergo temporarily a negligible change (to admit the typical waveform of a neuronal Action Potential). **Tables** 1 and 4 report the values of the parameters for the model of each NaMLab memristor (recall Equations (9)–(10)) and of the linear circuit elements, respectively. The vector $(x_{1,0}, \nu_{C_1,0}, x_{2,0}, \nu_{C_2,0}, \nu_{C_{in}}) \triangleq (x_1(0), \nu_{C_1}(0), x_2(0), \nu_{C_2}(0), \nu_{C_{in}}(0))$ of initial conditions is set to (711, 0.1 V, 709, 0.1 V, 0 V).

Table 4. Parameter setting for the linear circuit elements in the fifth-order neuristor circuit topology from Figure 22b. This circuit shares features the capability, typical of a biological neuron, to fire an electrical spike if and only if the strength of its stimulus exceeds a threshold value.

V_1	R_1	C_1	R_C	V_2
−1 V	50 Ω	180 nF	18 Ω	1 V
C_2	R_2	R_0	C_{in}	R_{in}
30 nF	50 Ω	18 Ω	180 nF	10 Ω

$$\dot{v}_{C,2} = \frac{1}{C_2} \cdot \left(-G_2 \cdot v_{C,2} - G(x_2) \cdot v_{m,2} + \frac{v_{C,1} - v_{C,2}}{R_C} \right), \text{and} \quad (67)$$

$$\dot{v}_{C_{in}} = \frac{1}{C_{in}} \cdot \left(\frac{v_{in} - v_{C_{in}} - v_{C_1}}{R_0} - G_{in} \cdot v_{C_{in}} \right) \quad (68)$$

where v_{in} denotes the input voltage, $G_{in} \triangleq R_{in}^{-1}$, while $v_{m,i} = v_{C,i} - V_i$ ($i \in \{1, 2\}$). Once again, assuming the two memristors to be perfectly matched one with the other, employing the NaMLab model DAE set (9)–(10), with parameter setting from Table 1, to describe each of them, and assigning the values reported in Table 4 to the parameters of the linear circuit elements, it is possible to tune the input voltage v_{in} in such a way to reproduce the conditional gain of a neuronal axon membrane. As illustrated in Figure 22f, perturbing the fifth-order circuit through a voltage source v_{in}, generating a $\Delta T = 5$ µs-wide rectangular voltage pulse from $t = 0.5$ms, the output voltage v_{out}, coinciding with v_{C_2}, is found to admit the shape of a neuronal electrical spike if and only if the input pulse amplitude V_{in}, here fixed to 100 mV, is set to a supra-threshold value (refer to the solid blue traces), while the voltage at the output node is negligible when the value, assigned to V_{in}, taken now as 50 mV, lies below the critical level (refer to the dashed-dotted traces).

8. The Most Elementary Hodgkin–Huxley Neuristor

With reference to the simplest ever reported Hodgkin–Huxley Neuristor in Norton form from Figure 2f, it may be reduced to a minimal form by replacing the parallel resistor R_L with an open circuit. A rigorous theoretical analysis was carried out to program the resulting three-element cell, composed of the parallel combination between one linear capacitor C, one locally-active current-controlled volatile NbO_{textx} memristor $\mathcal{M}$, manufactured at NaMLab and featuring a S-shaped DC current I_m versus voltage V_m locus, and one DC current source I, as illustrated in **Figure 23a**, so that it could reproduce qualitatively the classical bifurcation diagram of the neuron model conceived by Hodgkin and Huxley in 1952.[23] The three-element cell can be mathematically described through the second-order ODE set

$$\frac{dx}{dt} = g(x, v_m), \text{and} \quad (69)$$

$$\frac{dv_m}{dt} = \frac{1}{C} \cdot \left(I - i_m(x, v_m) \right) \quad (70)$$

in which the memristor state x and its voltage v_m, identically equal to the capacitance voltage v_C, represent the state variables, $g(x, v_m)$ denotes the state evolution function of the NbO_x threshold switch subject to voltage excitation, as expressed via Equation (11), while $i_m(x, v_m)$ stands for the NaMLab device current, as described through Ohm's law (10), in which $G(x)$ represents the memductance function defined in Equation (12). The memristor model parameters are provided in Table 1. Setting the capacitance C in this cell to 5 nF, the admissible quiescent and oscillatory steady states for the voltage v_m across the memristor under a monotonic increase in the DC current stimulus I are illustrated in Figure 23b. As its DC current stimulus is progressively increased from zero, the cell is first found to undergo a local Hopf Supercritical Bifurcation when I attains the value of 2.136 mA. Later, a local Hopf Subcritical Bifurcation emerges across the cell as I increases up to 17.960 mA. Shortly afterwards, the second-order memristive circuit experiences a global Saddle-Node Limit Cycle Bifurcation for $I = 18.1379189$ mA. *The three-element bio-inspired oscillator clearly acts as a Hodgkin-Huxley neuristor!* Very importantly, especially in view of a future hardware realization of our theory-inspired circuit design, *the minimal three-element circuit of Figure 23a exhibits a superior energy efficiency over the original four-element Norton circuit topology from Figure 2f*. In order to shed light into the reason why the three-element C-$\mathcal{M}$-I parallel circuit consumes less power than the original four-element C-R_L-$\mathcal{M}$-I_{in} parallel circuit while reproducing the classical bifurcation diagram of the Hodgkin–Huxley neuron model,[23] it is instructive to observe that the local Hopf bifurcation locus on the capacitance C versus memristor operating point Q plane for the original relaxation oscillator from Figure 2f moves downward, while its minimum shifts to the left, as the resistance R_L is subject to a progressive increase. This is shown in **Figure 24a**, where the black, blue, red, and magenta traces were respectively obtained by assigning the first, second, third, and fourth value from the set {25, 50, 330, 1000} Ω to the resistance R_L in the formula from Equation (53), that describes how the local Hopf bifurcation capacitance $C = \hat{C}(Q)$ for the four-element circuit of Figure 2f depends upon the memristor operating point Q, and thus on its DC current I_m, taking into account that each value for Q is associated unequivocally to one and only one value for I_m, as illustrated in Figure 4a, which further shows how poising the threshold switch on a higher operating point requires a larger modulus for the bias current which must necessarily flow between its terminals. Clearly, increasing the resistance R_L allows to reduce the lower bound of the moderate capacitance range, across which the four-element Norton cell of Figure 2f is able to reproduce the entire life cycle of an Action Potential across biological axon membranes under monotonic input current modulation according to the bio-plausible Hodgkin–Huxley neuron model, as listed in item (ii) of Section 6.2.3. As may be inferred by inspecting Figure 24a, this consequently allows to decrease the critical DC input currents, which induce the emergence of the local and global phenomena characterizing the Hodgkin–Huxley neuron model bifurcation diagram, across the four-element Norton cell. On the basis of these arguments, from a power consumption viewpoint, it is wise to remove the resistance R_L from the original four-element Norton cell. Taking the limit of $\hat{C}(Q)$ as R_L tends to positive infinity, the formula, expressing the dependence of the capacitance $C = \hat{C}(Q)$, at which the three-element parallel circuit of Figure 23a undergoes a local Hopf bifurcation, upon the memristor operating point Q, and thus, recalling Figure 4a, upon its

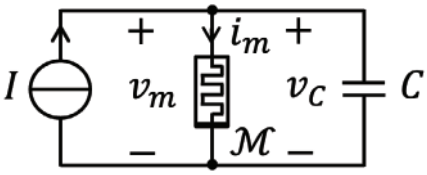

(a)

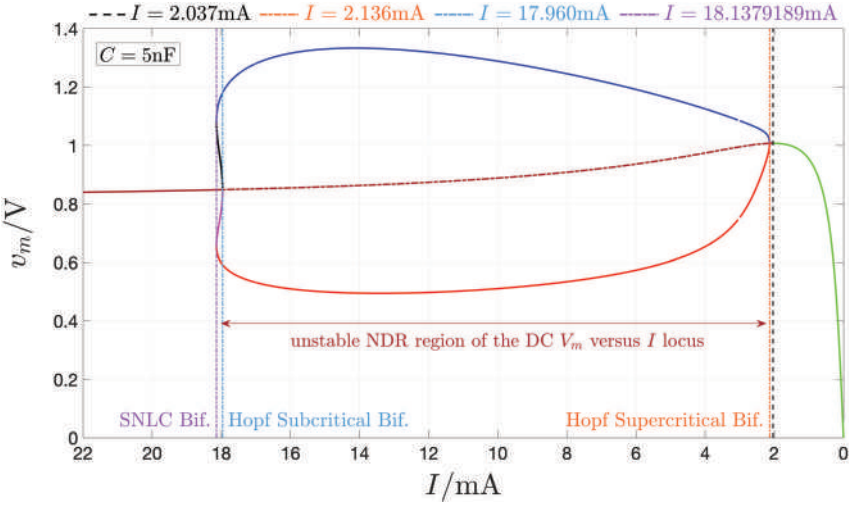

(b)

Figure 23. a) The most elementary form of the first and simplest ever reported bio-inspired Hodgkin–Huxley neuristor $\mathcal{N}$. This cell employs just three elements – one linear capacitor C, one locally-active current-controlled volatile memristor $\mathcal{M}$, manufactured at NaMLab and admitting a S-shaped DC current versus voltage locus, and one DC current source I – and leverages just two degrees of freedom, embodied in the memristor voltage v_m and state x, to undergo all the three fundamental bifurcations, which, according to the fourth-order mathematical model, reported by Hodgkin and Huxley in a seminal research manuscript[23] back in 1952, mark the life cycle of an Action Potential under a monotonic change in the net synaptic current across biological neuronal axon membranes. It is important to point out that, were the DC current stimulus I of the three-element cell chosen according to the constraint $I = I_{in} - V_m/R_L$, with the right hand side corresponding to the DC current I_m flowing through the memristor $\mathcal{M}$ in the four-element Norton cell of Figure 2f, endowed with resistance R_L and subject to bias input current I_{in}, the three-element circuit would be found to feature the very same DC operating point as the Norton circuit. However, the AC behaviors of the two DC-equivalent circuits would not be identical one to the other for a fixed capacitance value, as these depend upon the absence or presence of the resistance R_L within their topologies. b) Bifurcation diagram of the three-element cell showing all its admissible stable and unstable quiescent and oscillatory steady states under a forward sweep in the respective bias current stimulus I for $C = 5$ nF. Here, increasing I from 0 mA and 22 mA, the bio-inspired three-element parallel circuit is found to undergo first a Hopf Supercritical Bifurcation for $I = 2.136$ mA, then a Hopf Subcritical Bifurcation for $I = 17.960$ mA, and finally a global Saddle-Node Limit Cycle Bifurcation for $I = 18.1379189$ mA. Importantly, as may be evinced by inspecting the DC current input levels, at which the three fundamental neuronal bifurcations, underlying generation, evolution, and extinction of an electrical spike across a biological axon membrane according to the Hodgkin–Huxley model predictions, emerge across the three-element circuit from plot (a), removing the resistance R_L from the original four-element Norton cell from Figure 2f allows to improve the energy efficiency of the neuristor design. Since $I \, equiv I_m$, the brown trace is infact the DC voltage V_m versus current I_m locus of the NaMLab memristor. The reader is invited to consult the caption of Figure 18 to learn about the significance of all colors and line styles employed for drawing this bifurcation diagram.

DC current I_m, which here coincides with the cell DC current stimulus I, boils down to

$$\hat{C}(Q) = -\frac{l(Q)}{r_1(Q) \cdot r_2(Q)} \tag{71}$$

Employing Equation (71), the green trace in Figure 24a shows the local Hopf bifurcation locus on the capacitance C versus memristor operating point Q plane for the three-element cell. As expected from our earlier anticipations, for $C = 5$ nF the four-element cell of Figure 2f still exhibits a bubble-shaped bifurcation diagram under a monotonic sweep in the respective DC current stimulus I_{in}, as illustrated in Figure 21a,b, whereas the three-element circuit of Figure 23a is already capable to undergo the Hodgkin–Huxley neuron model bifurcation triplet under a progressive increase in the associated input current I, as showcased in Figure 23b. Figure 24b shows the regime, in which the three-element cell is found to operate for each choice of its two circuit design parameters, specifically the capacitance C and the DC current stimulus I. The violet horizontal line indicates the bifurcation route, which this cell experiences under a monotonic increase in the input current I for $C = 5$ nF. Recalling Figure 23b, in this scenario the three-element cell operates as a Hodgkin–Huxley neuristor. Importantly, with reference to the capacitance versus memristor operating point diagram of Figure 24b, and to its close-up view around the region, where the cell undergoes the

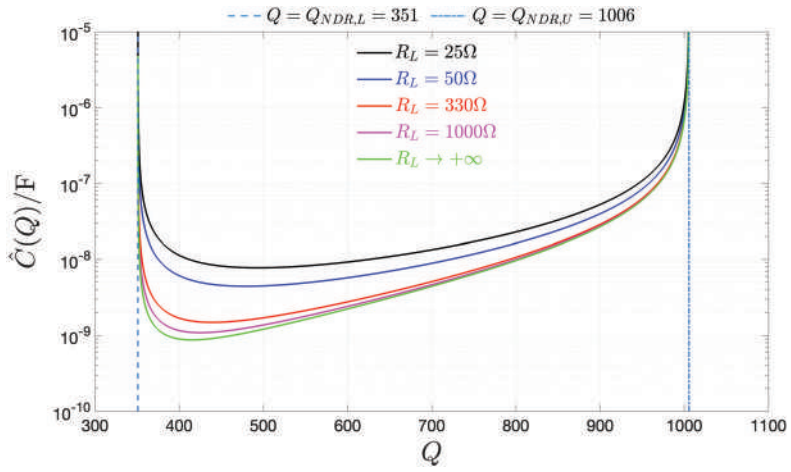

(a)

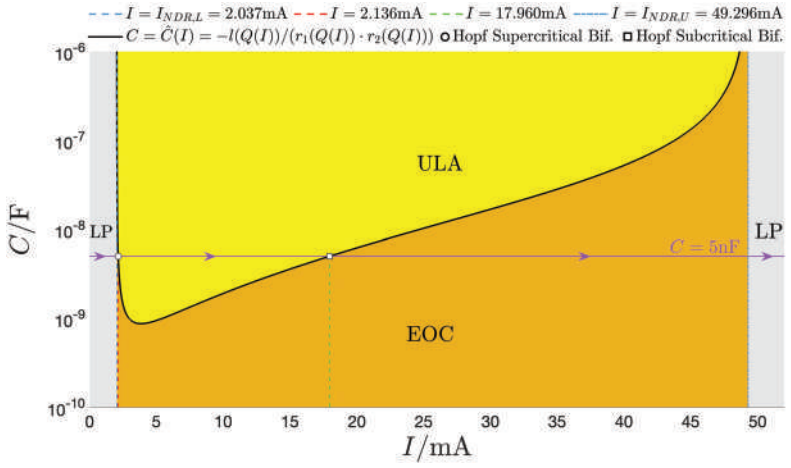

(b)

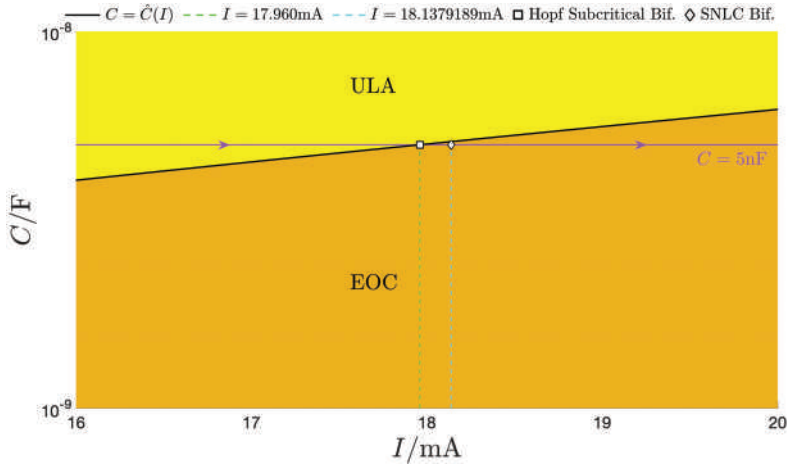

(c)

Figure 24. a) Locus of the local Hopf Bifurcation Capacitance $\hat{C}$ versus the memristor operating point Q for the four-element Norton cell of Figure 2f for four finite resistance values and in the limit as R_L tends to infinity. b) Classification of the admissible operating regimes for the proposed three-element bio-inspired oscillator from Figure 23a on the circuit design parameter plane, spanned by DC input current I and capacitance C on the horizontal and vertical axis, respectively. The black trace shows the graph of $\hat{C}(Q)$ from Equation (71), with Q being a single-valued function of I_m, coinciding here with I, as illustrated in Figure 4a, as a function of the DC current stimulus for the three-element cell. The violet horizontal line shows the bifurcation path,

local Hopf Subcritical and global Saddle-Node Bifurcations under DC input current forward sweep for $C = 5$ nF, as shown in plot (c) of the same figure, the three-element circuit of Figure 23a is found to sit on a stable and locally-active operating point as each of the three neuronal bifurcations of the Hodgkin–Huxley model classical bifurcation diagram appear across its circuitry.

9. Discussion

This is not the first time ever that a memristive analogue electronic circuit, reproducing neuronal phenomena, is reported in the literature. In 2013 Pickett et al. at HP Labs[28] proposed a fourth-order electronic neuron, *neuristor* for short, composed of two NbO_2 threshold switches, two capacitors, and a number of resistors, capable to generate an individual action potential under supra-threshold pulse voltage excitation. Augmented with an additional capacitor, the same neuristor from Hewlett Packard Labs could also be locked into various biomimetic oscillatory operating modes, including those referred to as regular spiking, fast spiking, and chattering under suitable DC current stimulation.

Importantly, Pickett et al. complemented model simulations with a robust experimental verification. Through a numerical study, in a follow-up paper,[43] Pickett et al. also demonstrated the computational universality enabled by the adoption of the fifth-order memristive neuristors in circuit design, showcasing how a suitable combination between a number of different Boolean logic gates, which, composed of cells of this kind, implement spike-based computing paradigms, may obey the fundamental cellular automata rule 137.

Shortly later, Yi from HRL Laboratories[12] employed the neuristor cell introduced by Pickett et al. in,[28] accommodating two VO_2 threshold switches in place for the pair of NbO_2 memristors adopted by the engineers from HP Labs, and paired it with different dendritic input circuits, including a resistor with or without an additional capacitor, to demonstrate via both numerical investigations and lab measurements as many as twenty-three dynamical phenomena appearing across phasic and tonic neurons from the central nervous system. In his paper Yi further revealed that the VO_2 memristor-based neuristor cell topology, mimicking tonic neurons, supports stochastically phase-locked firing, also known as skipping, under noise-prone DC current excitation, similar as biological neurons do.

More recently, in another major theoretico-experimental paper,[44] Kumar et al. introduced a miniaturized third-order NbO_2 nanodevice leveraging various electrophysiological processes, including the Mott phase-transition, to express a number of neuronal functions, including the generation of an individual All-or-None electrical spike, on its own. In this paper, Kumar et al. further employed a number of device samples of this kind to build a transistor-less analogue electrical network solving a computationally-hard problem known as graph coloring.[45]

Despite an experimental verification is yet to be provided, and will be part of an upcoming paper, the three-element memristive analogue electrical cell, presented in this paper, is however the first and most elementary circuit, capable to reproduce the entire life cycle of an Action Potential from birth to extinction via the All-to-None effect, as predicted by Hodgkin and Huxley in 1952,[23] ever reported in the literature.

In this regard, our work was moved by the wish to resolve an open problem raised by Pickett et al. in the maniscript[28] where they presented the two-memristor neuristor cell discussed above. In their seminal paper, Pickett et al. also reported a bifurcation diagram, acquired numerically as well as experimentally from the fourth-order neuristor, and visualizing the changes in the minima and maxima of the stable steady-state oscillatory solutions for the respective output voltage as the DC current stimulus was increased monotonically across a range of values inducing its fast spiking response. As reported in the caption of Fig. 3 in the manuscript,[28] "unlike the Hodgkin-Huxley model, the output voltage amplitude" was found to be "flat for both minimum and maximum spike voltages over the entire sweep range of the bifurcation current". Our research study was thus motivated by the need to address this issue, i.e. to reproduce qualitatively the classical bifurcation diagram, drawn by Hodgkin and Huxley in the membrane capacitance versus DC input synaptic current plane as a result of a numerical investigation of the proposed axon model.[23]

Our three-element cell, composed of the parallel connection between one NbO_x memristor on Edge of Chaos from NaM-Lab, one capacitor, and one DC current source, is the first and most elementary circuit ever found to reproduce one after the other the three fundamental neuronal bifurcations, underlying the most important phases in the life cycle of an All-or-None electrical voltage spike, also known as Action Potential, as compactly illustrated in the classical Hodgkin-Huxley model bifurcation diagram. In order to highlight this exceptional capability, we coined the name *Hodgkin-Huxley neuristor* to dub the proposed three-element biomimetic cell. Importantly, our extraordinary discovery of the emergence of the fundamental biological three-bifurcation cascade, signalling the most important life phases of a neuronal Action Potential, across such a simple three-element analogue electrical cell would not have been possible had we not recurred to the powerful concepts of the Local Activity and Edge of Chaos Theory, and applied insightful methods from Nonlinear Dynamics, including those enabling phase portrait investigations and bifurcation analysis of second-order ODE systems.

Last but not least, compact and scalable neuristor cells of the kind proposed here as well as in the aforementioned papers from Pickett et al.,[28] Yi,[12] and Kumar et al.[44] represent suitable neuromorphic building blocks for designing innovative bio-inspired

which the one capacitor *C*-one locally-active memristor $\mathcal{M}$-one DC current source *I* parallel cell of Figure 23a experiences for $C = 5$ nF under monotonic DC stimulus modulation. The loci, visualizing all the admissible stable and unstable steady-state quiescent or oscillatory solutions for the memristor voltage v_m in the three-element cell for this capacitance value under each DC input current *I*, are shown in Figure 23b, which visualizes a bifurcation diagram closely reminiscent of the one depicted in Figure 1c obtained numerically from the Hodgkin–Huxley neuron model. c) Zoom-in view of the v_m versus *I* diagram from plot (b) across the area, where the bifurcation path, followed by the three-element cell for $C = 5$ nF under forward sweep in the respective DC current stimulus *I* visits the cell bi-stability domain, which is sandwiched between the local Hopf Subcritical and global Saddle-Node Limit Cycle bifurcation points.

analogue electrical networks, which, implementing spike-based computing paradigms,[43,45] promise to approach the energy efficiency of the human brain in solving challenging problems, mitigating the von Neumann bottleneck, limiting the performance of central processing units in digital computing machines, as a result.

10. Conclusion

Memristors on Edge of Chaos[46] enable the design of bio-inspired circuits, capable to reproduce fundamental bifurcations, occurring in high-order biological systems, through a lower number of degrees of freedom. Recently, a simple array of identical and resistively-coupled cells, hosting only one dynamic circuit element, specifically a locally-active niobium oxide memristor from NaMLab, each, was found to reproduce diffusion-driven instabilities, anticipating static pattern formation, as occurring in a fourth-order reaction-diffusion biological cellular neural network from the Turing class.[20] Moreover, adding one capacitor in each cell, the resulting two-cell array, featuring four dynamic circuit elements, was found to replicate the counterintuitive phenomenon,[22] observed by Smale in an eight-order system, where two identical biological reaction cells, sitting quietly on a common quiescent state on their own, were found to pulse together indefinitely as they were let interact via diffusion processes. This manuscript reveals how upon a proper preliminary choice of the circuit parameters, as inferable through the application of the powerful concepts from the physics principle of the Edge of Chaos, the Norton form of the very same second-order relaxation oscillator, employed as basic cell in the design of the bio-inspired network, resolving the aforementioned Smale paradox, undergoes the three fundamental bifurcations, occurring in the fourth-order Hodgkin–Huxley neuronal axon membrane model, and characterizing the life cycle of an Action Potential, under DC current input sweep. To the best of our knowledge, this is the first and simplest ever-reported bio-inspired analogue electronic circuit, which, upon a monotonic change in the DC current stimulus I_{in}, entering the top node of its capacitance, supports one after the other the triplet of fundamental bifurcations, marking the most important life phases of a neuronal electrical spike, according to the bio-plausible Hodgkin–Huxley neuron model,[23] i.e., specifically first a Supercritical Hopf Bifurcation, giving birth to stable oscillations, then a Subcritical Hopf Bifurcation, spawning the emergence of an unstable periodic limit cycle in the respective phase plane, and finally the Global Fold or Saddle-Node Limit Cycle Bifurcation, at which the gentle coalescence between the outer stable and inner unstable limit cycles reveals the true origin of the *All-to-None Phenomenon*, as beautifully illustrated by the respective bifurcation diagram depicted in Figure 18b. The All-to-None phenomenon, whose origin puzzled the mind of the Italian luminary Galvani,[32] is in fact the effect of the global bifurcation, envisaging a sudden mutual annihilation via gentle coalescence between two limit cycles, one stable and the other unstable, born via Local Hopf Bifurcations while the neuristor operates on the *excitable part of its Local Activity Domain referred to as Edge of Chaos*. Remarkably, as is the case for the fourth-order Hodgkin–Huxley neuron model, the proposed neuristor is on Edge of Chaos when its stable and unstable steady-state oscillatory current and voltage solutions, whose coexistence is strictly necessary for the occurrence of the All-to-None effect, are born via local Hopf Bifurcations, which proves once more how it is fundamental for a dynamical system to operate in the Stable Local Activity Domain for complex phenomena to emerge across its physical medium. Furthermore, the sequence of three neuronal bifurcations appear across the proposed current-driven Hodgkin–Huxley neuristor when its memristor is poised along a negative-slope branch of the respective voltage versus current characteristic, which clearly showcases the impact of its Negative Differential Resistance effects on the complex dynamics of the second-order electrical system. In fact, it is precisely thanks to the Negative Differential Resistance effects of its memristor that our simple second-order relaxation oscillator is able to reproduce qualitatively the emergent phenomena appearing across a neuron model with double the number of dynamical states. Very importantly, *in its minimal form the proposed Hodgkin–Huxley Neuristor may be reduced to the three-element cell shown in Figure* Figure 23a. *A bifurcation diagram for this one capacitor C-one NaMLab NbO_x memristor $\mathcal{M}$-one bias current source I parallel circuit is shown in Figure* 23b *for* $C = 5$ nF. *Clearly, for such capacitance value the cell supports the classical bifurcation diagram of the Hodgkin–Huxley neuron model!* Last but not least, it is the application of the powerful concepts from Bifurcation Theory that has allowed us to delve deeply into the nonlinear dynamics of a simple second-order memristive circuit and to determine a suitable design parameter set turning it into the first and most elementary Hodgkin–Huxley neuristor ever reported in the literature. Our in-depth theoretical work awaits now experimental demonstration. In this regard, any kind of volatile memristor physical realization with non-monotonic *S*-shaped current versus voltage DC characteristic may be utilized (see ref. [47] for details). In fact, it may be proved that after adjusting the design parameters through an ad hoc bifurcation analysis along similar lines of reasoning as adopted in this research work, it is possible to use the model of any other locally-active current-controlled volatile memristor with non-monotonic *S*-shaped DC current versus voltage characteristic in the three-element cell of Figure 24a, and still induce the sequential occurrence of the three bifurcations, marking the life cycle of an Action Potential in the Hodgkin–Huxley neuron model, across its circuitry. In fact, employing a locally-active voltage-controlled volatile memristor physical realization with *N*-shaped voltage versus current DC characteristic, it is possible to observe the cascade between the three fundamental bifurcations underlying birth, evolution and extinction of an Action Potential across neuronal axon membranes also in the dual circuit, including the series between three components, specifically the voltage-controlled memristor, a DC voltage source, and a linear inductor. Undoubtedly, our theoretical work sheds light into the necessity to recur to concepts from the Theory of Nonlinear Dynamics to gain a comprehensive understanding of the operating principles of analogue electrical circuits with intrinsically-nonlinear locally-active memristors.[44] This is the only way to proceed for boosting sustainable progress in bio-inspired circuit design based on disruptive memristive nanotechnologies in the years to come.

Supporting Information

Supporting Information is available from the Wiley Online Library or from the author.

Acknowledgements

The research of L. C. was supported in part by the U.S. Air Force Office of Scientific Research (AFOSR) under Grant FA 9550-18-1-0016.

Conflict of Interest

The authors declare no conflict of interest.

Data Availability Statement

The data that support the findings of this study are available from the corresponding author upon reasonable request.

Keywords

action potential, all-to-none phenomenon, edge of chaos, electrical spike, Hodgkin–Huxley neuron model, local activity, NaMLab memristor, neuristor, negative differential resistance

Received: October 13, 2024
Revised: November 7, 2024
Published online:

[1] T. Brown, A. Zhang, F. Nitta, E. Grant, J. Chong, J. Zhu, S. Radhakrishnan, M. Islam, E. Fuller, A. Talin, P. Shamberger, E. Pop, R. Williams, S. Kumar, *Nature* **2024**, *1*.
[2] L. Chua, *Int. J. Bifurcat. Chaos* **2005**, *15*, 3435.
[3] K. Mainzer, L. Chua, *The Local Activity Principle*, 1st ed., Imperial College Press, Shelton Street 57, Covent Garden, London WC2H 9HE, UK, **2013**.
[4] J. Guckenheimer, P. Holmes, *Nonlinear Oscillations, Dynamical Systems, and Bifurcations of Vector Fields*, 1st ed., Springer-Verlag New York, Inc., New York, U.S., **1983**.
[5] L. Chua, V. Sbitnev, H. Kim, *Int. J. Bifurcat. Chaos* **2012**, *22*, 1250098.
[6] A. Andronow, C. Chaikin, *Theory of Oscillations*, Princeton University Press, Princeton, NJ, US, **1949**.
[7] D. Ielmini, R. Waser, Resistive Switching: From Fundamentals of Nanoionic Redox Processes to Memristive Device Applications, 1st ed., Wiley-VCH Verlag GmbH & Co. KGaA, Boschstraße 12, Weinheim 69469, Germany, **2016**.
[8] S. Ovshinsky, *Phys. Rev. Lett.* **1968**, *21*, 1450.
[9] Z. Wang, S. Joshi, S. Savel'ev, H. Jiang, R. Midya, P. Lin, M. Hu, N. Ge, J. Strachan, Z. Li, Q. Wu, M. Barnell, G.-L. Li, H. Xin, R. Williams, Q. Xia, J. Yang, *Nature Materials* **2017**, *16*, 101.
[10] M. Pickett, R. Williams, *Nanotechnology* **2012**, *23*, 215202.
[11] I. Messaris, D. Brown, A. Demirkol, A. Ascoli, M. Al Chawa, R. Williams, R. Tetzlaff, L. Chua, *IEEE Trans. Circuits Syst. I: Reg. Papers* **2021**, *68*, 4979.
[12] W. Yi, K. Tsang, S. Lam, X. Bai, J. Crowell, E. A. Flores, *Nature Communications* **2018**, *9*, 1.
[13] T. Brown, S. Kumar, R. Williams, *Appl. Phys. Rev.* **2022**, *9*, 011308.
[14] A. Ascoli, A. Demirkol, R. Tetzlaff, L. Chua, *IEEE Trans. on Circuits and Systems-I: Regular Papers* **2024**, *71*, 5.
[15] A. Ascoli, A. Demirkol, R. Tetzlaff, L. Chua, *IEEE Trans. on Circuits and Systems-I: Regular Papers* **2025**.
[16] G. Burr, R. Shelby, S. Sidler, C. di Nolfo, J. Jang, I. Boybat, R. Shenoy, P. Narayanan, K. Virwani, E. Giacometti, B. Kurdi, H. Hwang, *IEEE Transactions on Electron Devices* **2015**, *62*, 3498.
[17] Z. Wang, S. Joshi, S. Savel'ev, W. Song, R. Midya, Y. Li, M. Rao, P. Yan, S. Asapu, Y. Zhuo, H. Jiang, P. Lin, C. Li, J. Yoon, N. Upadhyay, J. Zhang, M. Hu, J. Strachan, M. Barnell, Q. Wu, H. Wu, R. Williams, Q. Xia, J. Yang, *Nature Electronics* **2018**, *1*, 137.
[18] A. Ascoli, A. Demirkol, R. Tetzlaff, L. Chua, *IEEE Transactions on Circuits and Systems–I: Regular Papers* **2022**, *69*, 4596.
[19] A. Ascoli, A. Demirkol, R. Tetzlaff, S. Slesazeck, T. Mikolajick, L. Chua, *Frontiers in Neuroscience* **2021**, *15*, 651452.
[20] A. Turing, *Philosophical Transactions of the Royal Society of London, Series B, Biological Sciences* **1952**, *237*, 37.
[21] A. Ascoli, A. Demirkol, R. Tetzlaff, L. Chua, *IEEE Transactions on Circuits and Systems–I: Regular Papers* **2022**, *69*, 1252.
[22] S. Smale, *Lectures on Mathematics in the Life Sciences* **1974**, *6*, 17.
[23] A. Hodgkin, A. Huxley, *J. Physiol.* **1952**, *117*, 500.
[24] A. Ascoli, A. Demirkol, R. Tetzlaff, L. Chua, *IEEE Trans. on Circuits and Systems-II (TCAS-II): Express Briefs* **2024**, *71*, 1721.
[25] E. Izhikevich, *Dynamical Systems in Neuroscience: The Geometry of Excitability and Bursting*, MIT Press, Cambridge, Massachusetts, US **2007**.
[26] L. Chua, *Japan. J. Appl. Phys.* **2022**, *61*, SM0805.
[27] H. Crane, *Proc. IRE* **1962**, *50*, 2048.
[28] M. Pickett, G. Medeiros-Ribeiro, R. Williams, *Nat. Mater.* **2013**, *12*, 114.
[29] L. Chua, C. Desoer, E. Kuh, *Linear and Nonlinear Circuits*, 1st ed., McGraw-Hill, Inc., US, **1987**.
[30] L. Chua, *CNN: A Paradigm for Complexity*, World Scientific Publishing Company, Farrer Road 128, Singapore 912805, Singapore, **1998**.
[31] D. Aidley, *The Physiology of Excitable Cells*, Cambridge University Press, y, 4th ed. **1998**.
[32] L. Galvani, *De Bonoiensi Scientiarum et Artium Instituto atque Academia Commentarii* **1791**, *7*, 363.
[33] L. Chua, *Applied Physics A* **2011**, *102*, 765.
[34] L. Thévenin, *Comptes Rendus Hebdomadaires De L'Academie Des Sciences* **1883**, *97*, 159.
[35] H. Mayer, *Telegraphen und Fernsprech Technik* **1926**, *XV*, 335337.
[36] L. Chua, *Radioengineering* **2015**, *24*, 319.
[37] A. Ascoli, S. Slesazeck, H. Mähne, R. Tetzlaff, T. Mikolajick, *IEEE Trans. Circuits and Systems-I (TCAS-I): Regular Papers* **2015**, *62*, 1165.
[38] A. Demirkol, A. Ascoli, I. Messaris, R. Tetzlaff, in *Memristor - An Emerging Device for Post-Moore's Computing and Applications* (Eds. Y.-F. Chang), IntechOpen Limited, London, UK, **2021**, 378, ch 5.
[39] B. Van der Pol, *The London, Edinburgh, Dublin Philos. Mag. J. Sci.* **1926**, *2*, 978.
[40] S. Pearson, H. Anson, *Proc. Physical Soc. London* **1921**, *34*, 175.
[41] S. Pearson, H. Anson, *Proc. Physical Soc. London* **1921**, *34*, 204.
[42] L. Trotta, E. Bullinger, R. Sepulchre, *PLoS ONE* **2012**, *7*, 11.
[43] M. D. Pickett, R. S. Williams, *Nanotechnology* **2013**, *24*, 384002.
[44] S. Kumar, J. P. Strachan, R. S. Williams, *Nature* **2020**, *585*, 318.
[45] M. Weiher, M. Herzig, R. Tetzlaff, A. Ascoli, T. Mikolajick, S. Slesazeck, *IEEE Trans. on Circuits and Systems-Part I: Regular Papers* **2020**, *68*, 2082.
[46] L. Chua, *Nature Reviews Electrical Engineering* **2024**, *14*.
[47] A. Ascoli, A. Demirkol, I. Messaris, V. Ntinas, D. Prousalis, S. Slesazeck, T. Mikolajick, F. Corinto, M. Bonnin, M. Gilli, P. Civalleri, R. Tetzlaff, L. Chua, *ACS Nano* **2025**.